Summer 7-25-2022

Atomic Gradiometry Based on the Interference of Microwave Optical Sidebands

Kaleb L. Campbell
University of New Mexico - Main Campus

Kaleb Campbell

Candidate

Optical Science and Engineering

Department, The University of New Mexico

This dissertation is approved, and it is acceptable in quality and form for publication:

Approved by the Dissertation Committee:

Dr. Peter Schwindt, Chair

Dr. Elohim Becerra

Dr. Victor Acosta

Dr. Jean-Claude Diels

Defended June 3, 2022.

Atomic Gradiometry Based on the Interference of Microwave Optical Sidebands

by

Kaleb Campbell

B.S., Miami University, Oxford Ohio, 2016
M.S., University of New Mexico, 2019

DISSERTATION

Submitted in Partial Fulfillment of the
Requirements for the Degree of

Doctor of Philosophy
Optical Science and Engineering

The University of New Mexico

Albuquerque, New Mexico

July, 2022

Dedication

To Karishma

For making chai to keep me awake

Acknowledgments

First, I would like to thank my advisor Dr. Peter Schwindt for his help designing and performing experiments, providing funding for me to attend conferences, and for editing my manuscripts. I would like to thank Dr. Vishal Shah for his help with paper writing and his creative ideas for new experiments. I would like to thank Dr. Yuan-Yu Jau for his help with the theoretical aspects of the project. I would also like to thank my committee members for agreeing to read my thesis and attend my defense.

I would like to thank my friends and colleagues at UNM and Sandia, too numerous to name, for their support over the years. Also, I would like to thank Matt, who flew all the way to India for my wedding, and who has been my friend, and roommate, for over 25 years! I would most like to thank my wonderful wife Karishma, who I love dearly. She is my best friend and has stood by me during good times and in bad, and I will never forget that. Finally, I would like to thank my parents who always pushed me to further my education.

This work was funded by the Defense Advanced Research Projects Agency (DARPA) under the AMBIIENT program, contract No. 140D6318C0021. The views, opinions and/or findings expressed are those of the authors and should not be interpreted as representing the official views or policies of the Department of Defense or the U.S. Government.

Sandia National Laboratories is a multimission laboratory managed and operated by National Technology and Engineering Solutions of Sandia, LLC, a wholly owned subsidiary of Honeywell International Inc., for the U.S. Department of Energy National Nuclear Security Administration under Contract No. DE-NA0003525. Approved for Public Release, Distribution Unlimited

Atomic Gradiometry Based on the Interference of Microwave Optical Sidebands

by

Kaleb Campbell

B.S., Miami University, Oxford Ohio, 2016
M.S., University of New Mexico, 2019

Ph.D., Optical Science and Engineering, University of New Mexico, 2022

Abstract

We describe a novel pulsed magnetic gradiometer based on the optical interference of sidebands generated using two spatially separated alkali vapor cells. The sidebands are produced with high efficiency using parametric frequency conversion of a probe beam interacting with ^{87}Rb atoms in a coherent superposition of magnetically sensitive hyperfine ground states. First, experimental evidence of the sideband process is described for both steady-state and pulsed operation. Then, a theoretical framework is developed that accurately models sideband generation based on density matrix formalism. The gradiometer is then constructed using two spatially separated vapor cells, and a beat-note is generated. The frequency of the beat-note is determined by the magnetic field gradient between the two vapor cells. In contrast to traditional magnetic gradiometers, our approach provides a direct readout of the gradient field without the intermediate step of subtracting the outputs of two spatially separated magnetometers. Using this technique, we developed a compact magnetic gradiometer

sensor head with integrated optics with a sensitivity of 25 fT/cm/$\sqrt{Hz}$ with a 4.4 cm baseline, while operating in a noisy laboratory environment unshielded from Earth's field. Also, operation of the sensor in magnetic fields both along the laser axis and perpendicular to the axis are discussed, leading to the potential of making the sensor dead-zone-free.

Contents

List of Figures

List of Acronyms

ADC	Analog-to-digital Converter
AOM	Acousto-Optic Modulator
BS	Beam Splitter
BNC	Bayonet Neill–Concelman Cable
CW	Continuous Wave
DC	Direct Current
DFB	Distributed Feedback Laser
FOM	Figure of Merit
HWP	Half-Wave Plate
MEG	Magnetoencephalography
MODR	Microwave Optical Double Resonance
PBS	Polarizing Beam Splitter
PD	Photo Diode
OD	Optical Depth
OPM	Optically Pumped Magnetometer
QWP	Quarter Wave Polarization
SERF	Spin Exchange Relaxation-free
SQUID	Superconducting Quantum Interference Device

Chapter 1

Introduction

Physicists have long used atoms, and in particular alkali atoms due to their favorable properties, as a platform for studies in fundamental physics, such as testing the foundations of quantum mechanics (Pipkin, 1979), studies of new states of matter (Wynar et al., 2000), and dark matter axion detection (Sikivie, 2014), among many other topics. On the applications side, atoms have found use in a variety of areas such as atomic clocks (André et al., 2004, Bize et al., 2005), which are currently the most precise measure of time, atom interferometers (Abend et al., 2019), which are typically used to measure the strength of gravity but also find use in other areas (Smith et al., 2011), Rydberg atomic electric field sensors (Simons et al., 2021), and optically pumped atomic magnetometers and gradiometers, which measure magnetic or gradient magnetic fields and are the topic of this thesis. More recently, atoms have found use in the burgeoning field of quantum information science where they are being used as a platform for qubits (Saffman, 2016), which provide an architecture for quantum computing (Henriet et al., 2020, Saffman et al., 2010).

Most atomic physics experiments can be categorized as one of two types; warm vapor experiments or cold atom experiments. Warm vapor experiments are inherently easier to build and maintain than cold atom experiments due to the simplicity of the apparatus. For warm atom experiments, atoms are placed in an enclosed volume

(usually a pyrex vapor cell), that is in the path of a laser beam. Maybe some shielding or heating is required, but nothing of substantial complexity. On the other hand, cold atom experiments require more extensive apparati for their operation, with a variety of lasers used to cool the atoms down to ultra low temperatures approaching absolute zero (μK). One of the advantages of cold atoms is that decoherence lifetimes are typically much longer than with warm atoms, which can be useful for generating long lived states and coherences. However, warm atoms have the advantage of atom number density since the sensitivity scales as $\frac{1}{\sqrt{N}}$, where N is the number of atoms used in the measurement. For this dissertation, we use a warm alkali atom atomic vapor cell ($\sim 100^o$ C) to build a novel atomic gradiometer.

1.1 Optically Pumped Magnetometers

In this section we describe the operation of Optically Pumped Magnetometers (OPMs) Budker and Romalis (2007), which typically use alkali atoms, but also others such as helium (Fourcault et al., 2021), to measure magnetic fields. The fundamental principle behind OPMs is the measurement of spin polarized atoms precessing in a magnetic field (Seltzer, 2008). By optically pumping the atoms, the atomic spins are initially aligned. Then, the spins undergo Larmor precession when they are exposed to a magnetic field. The Larmor precession frequency is given by

$$\omega = \gamma|\mathbf{B}| \tag{1.1}$$

where γ is the gyromagnetic ratio for the atomic species, and $|\mathbf{B}|$ is the absolute value of the magnetic field. It can be seen that from a measurement of the precession frequency we can calculate the magnetic field to which the atoms are exposed. The last two decades have witnessed steady progress in the field of OPMs (Bell and Bloom, 1957, Dehmelt, 1957, Tierney et al., 2019) based on alkali vapor cell technology. The sensitivity of OPMs (Dang et al., 2010, Kominis et al., 2003) now rivals superconducting quantum interference device (SQUID) (Cohen, 1972)

magnetic sensors that have been the gold standard for bio-magnetic measurements (Hämäläinen et al., 1993, Vrba et al., 1999) for many decades. The sensitivity of these magnetometers is far below the magnetic noise floor set by ambient geophysical magnetic activity ($\sim 50\mu$ T) and the urban environment. The OPMs with the lowest sensitivity, spin exchange relaxation free (SERF) magnetometers, operate at near zero ambient field and require magnetic shielding or field cancellation coils (Allred et al., 2002, Kominis et al., 2003). In larger fields, these magnetometers experience decoherence from spin-exchange collisions, limiting their sensitivity. Since SERF magnetometers operate near zero-field, most MEG measurements with OPMs are performed in magnetically shielded enclosures (Boto et al., 2018). An OPM based sensor that can maintain good magnetic sensitivity in a noisy environment, without magnetic shielding, is of great interest since it allows for the study of subjects in more diverse environments and further reduces the cost and complexity of the sensor (Boto et al., 2018).

1.2 Atomic Gradiometers

Magnetic gradiometers are typically better than magnetometers at detecting near-field magnetic sources because they eliminate the common field noise from far away sources. This gives them advantage when operating unshielded in noisy environments, such as an unshielded room in Earth's field (Sulai et al., 2019). Magnetic gradients are typically measured by subtracting the magnetic field from two spatially separated total field magnetometers, with the magnetic gradient calculated in post processing (Limes et al., 2020, Sheng et al., 2017). With SQUIDs, two spatially separated flux pickup coils with opposing polarities can be wired together to form an intrinsic gradiometer (Koch et al., 1993, Zimmerman and Frederick, 1971). In contrast, few OPM-based techniques exist to build similar intrinsic gradiometers using vapor cells (Kamada et al., 2015, Lucivero et al., 2021, Perry et al., 2020, Sulai et al., 2019, Zhang et al., 2020). Most OPM-based gradiometers rely on subtracting the output of

two spatially separated magnetometers (synthetic gradiometer) (Johnson et al., 2010, Limes et al., 2020, Shah and Wakai, 2013), and differences and drifts between the two magnetometers can reduce the rejection of common-mode signals. Unshielded gradient sensitivities have been recorded as low as 15.7 $\frac{fT}{cm\sqrt{Hz}}$ (Limes et al., 2020) using the subtraction technique, but this method is technologically difficult and the subtraction of fields may not be perfect over the entire bandwidth.

1.3 Novelty and Advantages of Our Approach

In this thesis, we demonstrate an optical gradiometer where the atom-optical system itself performs the gradient subtraction between two spatially separated vapor cells. We do "NOT" extract the magnetic field from the two physically separated cells, just the gradient field. This makes the gradiometer measurement intrinsic.

The majority of magnetometers are based on measurements of absorption or Faraday rotation (Dehmelt, 1957) and operate on the Zeeman sublevels (RF frequencies). Our gradiometer operates on the hyperfine manifold, with coherences generated between hyperfine ground state sublevels in rubidium (microwave frequency splitting). Many OPMs are limited by excess photon shot noise because the signal is accompanied by background light. Our gradiometer allows for the measurement of signal photons while suppressing the background light. Because of strong background field suppression, it is possible to operate at very low optical depths with vapor cells heated to $< 100^o$ C. This allows for the design of a sensor head to meet power consumption requirements in commercial devices. In addition, because the temperature is relatively low, the device will not be too warm (with appropriate insulation) to place on the human scalp for biomedical applications such as magnetoencephalography (MEG) (Cohen, 1972, Hämäläinen et al., 1993, Tierney et al., 2019). Also, our gradiometer can operate with near-unity spin polarization, thus maximizing signal generation. These two features remove fundamental barriers for reaching atom shot-noise-limited sensitivity (Braginsky et al., 1992, Kominis, 2008).

Moreover, our technique probes the hyperfine magnetic end states which amplifies the sensitivity of the energy levels to magnetic fields by a factor of three compared to the $\Delta m_F \pm 1$ Zeeman states utilized in traditional alkali optically pumped magnetometers (Kimball et al., 2013). However, a limitation of this gradiometer is that there is an additional decay mechanism on the hyperfine manifold vs. the Zeeman manifold known as the Carver rate (Arditi and Carver, 1964, Camparo, 2007). This decay mechanism makes the decoherence times less than would be expected for magnetometers based on the Zeeman splitting.

1.4 Thesis Outline

This dissertation is divided into seven chapters, including the introduction.

In Chapter 2 we describe the crucial background information needed to understand the experiments we perform in this thesis. For example, we describe the level spitting of rubidium vapor, the optical pumping process, and the effect of buffer gas in the vapor cell.

In Chapter 3 we show experimental evidence of sideband generation, which is the essence for the optically pumped atomic gradiometer we build in Chapter 5. We experimentally show sideband generation for the "steady-state" case, where the pump and microwave fields are always on and for the case of a "pulsed experiment", where the pump and microwave fields are turned off when measurements are made. We then conduct a study of vapor cells filled with various buffer gas pressures and define a parameter (FOM) to tell us which buffer gas pressures work best for our experiments.

In Chapter 4 we describe the sideband generation process in much more detail. Starting with Maxwell's equations, we derive a propagation equation for the sidebands as they travel through a vapor cell. We then solve the propagation equation and develop a numerical model which predicts the behavior of the sidebands. We then perform an experiment to ascertain the validity of the numerical model.

In Chapter 5 we detail the experimental setup used to build an optically pumped atomic gradiometer based on the interference of the sidebands. We also make some preliminary measurements of the noise floor using the tabletop experimental setup and a miniaturized "physics package" gradiometer.

In Chapter 6 we perform experiments to show the feasibility of operating the gradiometer in magnetic gradients from all spatial directions, making the gradiometer Dead-Zone-Free. This is useful for applications since multiple components of the gradient field can be measured without physically rotating the apparatus.

In Chapter 7 we conclude the dissertation and provide a summary of the results as well as some possible future experiments.

Chapter 2

Background

In this chapter we describe the background information most relevant to our experiments in an ensemble of warm ^{87}Rb atoms. The sections in this chapter are crucial to the understanding of material in the later chapters, particularly Chapter 3 when we focus on the sideband generation process and Chapter 4 where we provide a detailed theoretical analysis of sideband generation using Maxwell's equations.

2.1 Alkali Atoms

Alkali atoms are of special importance to the fields of physics, optics, and chemistry due to their favorable properties. They have an odd number of electrons, with a single unpaired valence electron farthest from the core of the atom. This valence electron can be easily manipulated with electromagnetic radiation while the rest of the internal structure of the atom is less affected by electromagnetic fields. This fact makes alkali atoms particularly useful in experiments which involve the manipulation of the atomic state of atoms. In modern experiments, lasers are typically used to probe the atoms at optical frequencies, and antennas, or cavities, are used to probe at RF and microwave frequencies (Deutsch and Jessen, 1998). When the energy level structure of an alkali atom is calculated, the energy of the valence electron is

most relevant. In fact, alkali atoms behave similarly to hydrogen atoms with a single electron and proton. The lower energy level electrons and the protons effectively neutralize each other leaving a single proton and the electron in the outer shell.

2.2 Fine and Hyperfine Structure

The interaction of the electron orbiting the nucleus causes the atomic energy levels to split. The interaction between the spin of the electron (**S**) and the orbital angular momentum (**L**) of the electron results in the fine structure. We write the total angular momentum of the electron as

$$\mathbf{J} = \mathbf{L} + \mathbf{S}, \tag{2.1}$$

where the quantum number **J** can take on the values $|L - S| \leq J \leq L + S$ and its magnitude is $\sqrt{J(J+1)}\hbar$. For the ground state of an alkali atom, $L = 0$ and $S = 1/2$, so $J = 1/2$. For the first excited state, $L = 1$, resulting in $J = 1 + 1/2 = 3/2$ and $J = |1 - 1/2| = 1/2$. In spectroscopic notation the ground state, $L = 0$, is an S orbital and can be written as $5^2S_{1/2}$ and the first excited states are a P orbital and can be written as $5^2P_{1/2}$ and $5^2P_{3/2}$. For historical reasons, the $5^2S_{1/2} \rightarrow 5^2P_{1/2}$ transition is known in alkali atoms as the D_1 line and the $5^2S_{1/2} \rightarrow 5^2P_{3/2}$ transition is known as the D_2 line.

The fine structure is further split due to the interaction of **J** with the nuclear spin (**I**) of the atom. This splitting is known as the hyperfine splitting and the total angular momentum of the atom is given by

$$\mathbf{F} = \mathbf{J} + \mathbf{I}, \tag{2.2}$$

where similar to **J**, **F** can take on the values $|J - I| \leq F \leq J + I$. For the case of ^{87}Rb, which is used extensively in this thesis, $I = 3/2$, and hence the ground state, $5^2S_{1/2}$, is split into $F = 1/2 + 3/2 = 2$ and $F = |1/2 - 3/2| = 1$. For excited state $5^2P_{1/2}$, a similar calculation gives $F = 1$ or 2 and for the $5^2P_{3/2}$ excited state $F =$

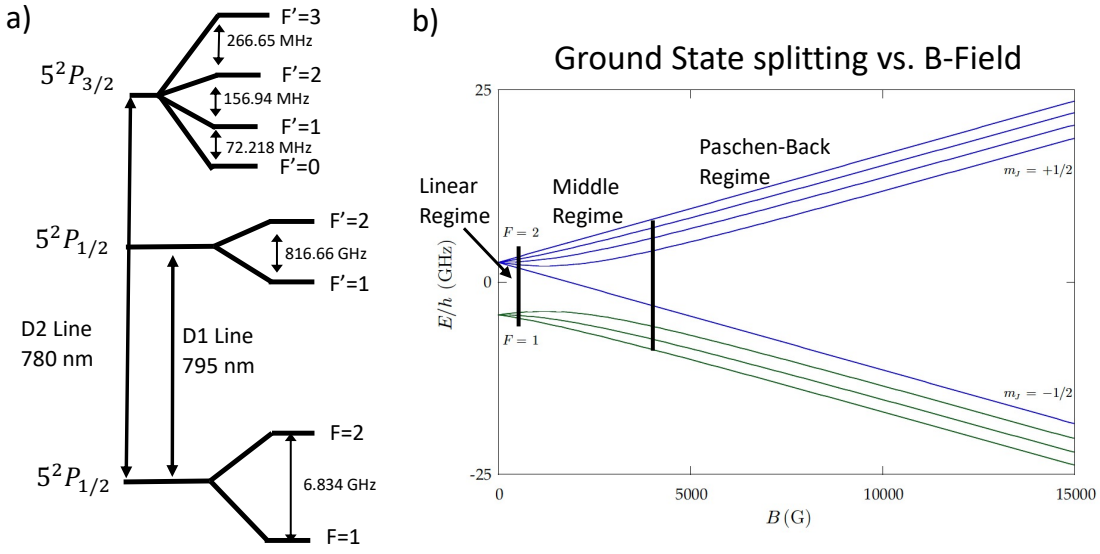

Figure 2.1: The fine and hyperfine splitting for ^{87}Rb. (a) The D_1 line is 795 nm and the D_2 line is 780 nm. The splittings are not to scale. (b) Plot borrowed from Steck (2003) which shows the ground state splitting vs. B-field and the splitting regimes. We perform signal measurements when the field strength is in the linear regime.

0,1,2 or 3. Figure 2.1(a) shows D_1 and D_2 lines for ^{87}Rb with the approximate energy splittings between the hyperfine manifolds.

2.3 Zeeman Effect

When in the presence of an external magnetic field, the levels are further split into $(2F+1)$ Zeeman sublevels. For example, the $5^2S_{1/2}$ ground state in ^{87}Rb splits into an 8-level manifold, with $F=1$ splitting into 3-levels and $F=2$ splitting into 5-levels. This is due to the interaction of the total atomic magnetic moment of the atom, which is the sum of the electronic and nuclear moments, with an external magnetic field. For a magnetic field along the z-direction, and in the weak field limit, the Zeeman splitting is given by Steck (2003)

$$\Delta E_{mF}|F, m_F\rangle = \mu_B g_F m_F B_z \tag{2.3}$$

where ΔE_{mF} is the change in energy for a particular energy level, μ_B is the Bohr magneton, g_F is the Lande-g-factor, and B_z is the magnetic field amplitude in the z-direction.

In a small magnetic field, the energy splitting between each sublevel in the manifold is given by the gyromagnetic ratio (γ), which for rubidium is $\gamma/2\pi \approx 7$ Hz/nT. This means that a 1 nT magnetic field splits the Zeeman levels by approximately 7 Hz. For states at the "end" of the ground state manifold, the splitting between them and the $|F = 2, m_F = 0\rangle$ state gets multiplied by their magnetic quantum number m_F. As an example, when the $|F = 2, m_F = 2\rangle$ state splits, the total first-order frequency shift is $7 \times m_F = 14$ Hz/nT. Also, $|F = 2, m_F = 0\rangle$ state is known as a "clock state" because it is only 2nd order sensitive to the magnetic field. Thus, "clock transitions" between $m_F = 0$ states are more stable and less sensitive to environmental noise. This makes them excellent for atomic clocks (Camparo, 2007, Knappe et al., 2005) where stability is very important. However, for applications such as magnetometers and gradiometers, where measuring the field strength is the objective, probing the end states is more effective (Campbell et al., 2022).

The splitting of the hyperfine sublevels for higher magnetic field strengths is, in general, more difficult to calculate. In the high-field limit, which is known as the Paschen-Back Regime, the states are no longer grouped with respect to F but with respect to m_J as shown in Fig. 2.1(b). For the ground state manifold of ^{87}Rb, the Breit-Rabi formula is used to model the manifold splitting as it passes between the low-field, mid-field, and high-field regimes. It is given as (Corney, 1977)

$$\Delta E_{BR} = \frac{-\Delta E_{hfs}}{2(2I+1)} - \frac{\mu_I B_z}{I} m_F \pm \frac{\Delta E_{hfs}}{2}\sqrt{1 + \frac{4m_F}{2I+1}x + x^2} \tag{2.4}$$

where $\pm$ refers to the upper and lower hyperfine states, ΔE_{hfs} is the hyperfine splitting, and $x \approx \frac{g_J \mu_B B_z}{\Delta E_{hfs}}$ is the ratio between the Zeeman splitting and the hyperfine splitting. For many applications, such as atomic magnetometers inside magnetic shielding, the magnetic field strengths are small enough that the splitting is approximately linear. However, for devices which operate in stronger fields, such as the Earth's magnetic

field, the fields are strong enough that the nonlinear splitting needs to be taken into account.

2.4 Atomic Selection Rules

Not all transitions between energy levels are possible. Selection rules describe which transitions are allowed or prohibited from occurring. When an electromagnetic field is incident on an atom, either the electric field component or magnetic field component can drive transitions if it is on resonance and obeys selection rules. Selection rules are important for our experiments because the angle of the measured magnetic field with respect to the laser direction effects the signal amplitude. By changing the atomic state of the atoms, magnetic fields in orthogonal directions can be measured without significant signal amplitude reduction. Here we provide the basic ideas behind the topic and we investigate it more extensively in Chapter 6.

The D_1 and D_2 transitions in ^{87}Rb vapor are optical transitions. The electric field of an oscillating electromagnetic wave couples with the electric dipole of the atoms. The electric dipole coupling is given by

$$V_e = -\mathbf{D} \cdot \mathbf{E} \tag{2.5}$$

where $\mathbf{D}$ is the dipole operator and $\mathbf{E}$ is the electric field.

The transitions between the ground states of the hyperfine manifold are magnetic dipole transitions. Magnetic dipole transitions couple states with the same parity (Cohen-Tannoudji et al., 1986). The electric dipole moment is zero for these transitions due to the geometrical symmetry. The interaction of the magnetic field with the atoms is given by

$$V_m = -\boldsymbol{\mu_{tot}} \cdot \mathbf{B} \tag{2.6}$$

where $\boldsymbol{\mu_{tot}} = \boldsymbol{\mu_L} + \boldsymbol{\mu}_s + \boldsymbol{\mu_I}$ is the total magnetic moment of the atom given by the sum of the orbital, spin, and nuclear magnetic moments.

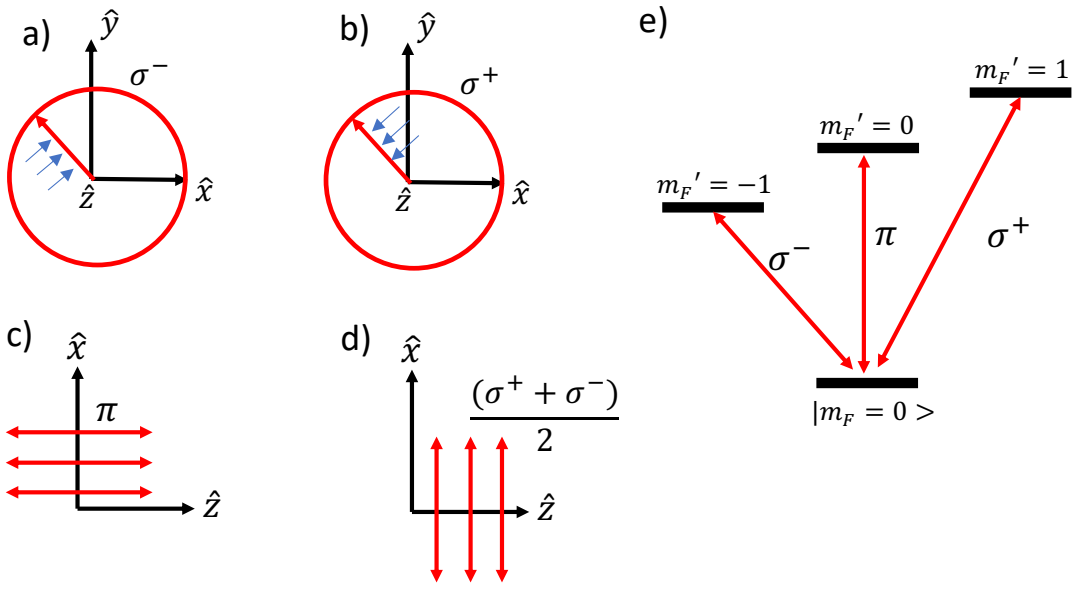

Figure 2.2: Visual representation of the selection rules for optical polarization. (a) The polarization vector rotates counter-clockwise in a plane perpendicular to $\hat{z}$. This is σ^- light with respect to the $\hat{z}$ axis. (b) Similar to the first plot but the polarization vector rotates clockwise with respect to $\hat{z}$. This is σ^+ polarized light. (c) Light traveling in the $+\hat{x}$ direction with the electric field polarized along $\hat{z}$ is π polarized with respect to $\hat{z}$ (d) Linearly polarized light traveling along $\hat{z}$ is a superposition of σ^+ and σ^- polarizations. (e) Visual representation of allowed transitions for different light polarizations.

For the optical transitions, the allowed transitions are $\Delta F = 0, +1, -1$ and $\Delta m_F = 0, +1, -1$ (Auzinsh et al., 2010). As an example, a transition from $|F = 1, m_F = 1\rangle \rightarrow |F' = 1, m_F = 1\rangle$, where the prime indicates the excited state, is allowed, but the transition $|F = 1, m_F = 1\rangle \rightarrow |F' = 1, m_F = -1\rangle$ is not because $\Delta m_F = 2$.

Light polarization plays a large role in the absorption and emission of light by an atom. By definition, σ polarized light drives $\Delta m_F = \pm 1$ transitions by exchanging angular momentum and π polarized light drives $\Delta m_F = 0$ transitions. The polarization that the atoms "see" is dependent on the physical geometry of the experiment with reference to a coordinate system. The coordinate system is arbitrary but is usually defined as the one which is easiest to work in mathematically. In this case, we define the $\hat{z}$ axis to be along the direction of the magnetic field. Fig.

2.2 shows a visual representation of the selection rules for optical polarization with respect to the quantization axis ($\hat{z}$). Fig. 2.2(a) shows a plane wave traveling in the $\hat{z}$ direction with the electric field vector pointing in a direction orthogonal to the direction of propagation. The electric field vector is rotating in the x-y plane in a counterclockwise fashion (as defined by a standard analog clock), and we denote this as σ^- polarized light. In Fig. 2.2(b) the polarization vector is rotating clockwise in a plane perpendicular to $\hat{z}$ and we denote it as σ^+. In Fig. 2.2(c) the propagation direction of the light is in the $\hat{x}$ direction, which is perpendicular to the $\hat{z}$ direction, and the light is linearly polarized with the electric field vector pointing in the $\hat{z}$ direction. In this case, since the polarization vector points in the direction of the quantization axis, the light is described as π polarized. If the light is linearly polarized and traveling in the $\hat{z}$ direction, the polarization can be described as a superposition of σ^+ and σ^- light which is shown in Fig. 2.2(d). For other cases not shown, such as elliptically polarized light, the polarization can aways be described as a combination of $\sigma^\pm$ and π light. In Fig. 2.2(e) we show a plot which shows Δm_F transitions, for different light polarizations, between the ground and excited states for a hypothetical atom. These optical selection rules are extremely important for the experiments described in this thesis, and more details will be discussed in Chapter 6 when we talk about operating a gradiometer in all three spatial directions relative to the magnetic field.

2.5 Optical Pumping

One way to increase signal size is to "optically pump" the atoms, which increases the atomic population in the desired ground state sublevel. This effect is particularly useful in the generation of sidebands, which we describe in Chapter 3. In Fig. 2.3 we show the optical pumping process on the D_1 line in ^{87}Rb vapor. Circularly polarized light (σ^+) drives $\Delta m_F = +1$ transitions, due to an exchange in angular momentum, to the excited state. When the atoms decay back down from the excited state, the

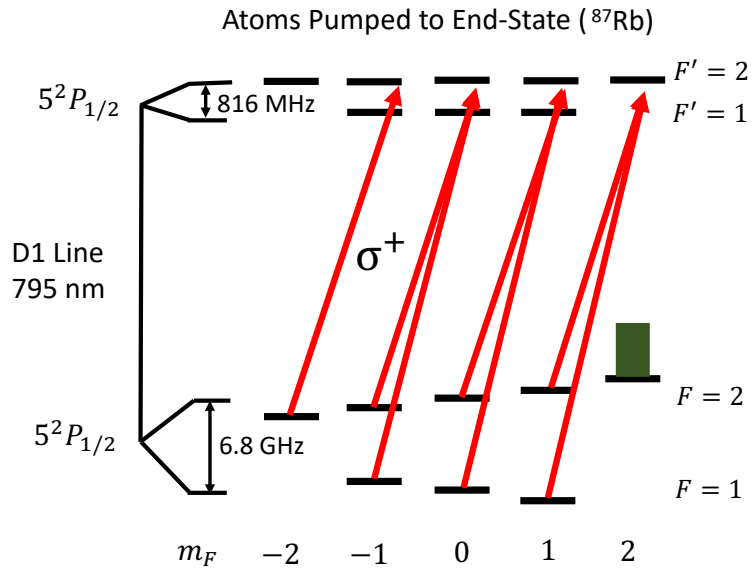

Figure 2.3: The Optical Pumping process on the D_1 line in ^{87}Rb vapor. Circularly polarized light (σ^+) incident on the ground states causes $\Delta m_F = +1$ transitions to the excited state. A net movement of atoms occurs towards one side of the manifold trapping population in the $|F = 2, m_F = 2\rangle$ "end-state". Selection rules prohibit excitation from the end state to the excited state.

scattered light makes $\Delta m_F = -1, 0$, or $+1$ transitions with equal probability, so the atoms make a net $\Delta m_F = 0$ transition. This results in a net movement of the atomic state towards one side of the hyperfine ground state manifold. Once the atoms are driven into the $|F = 2, m_F = 2\rangle$ "end-state", they are effectively "trapped". Selection rules prohibit excitation from the end state to the excited state by applying σ^+ light since there are no excited state sublevels in which to make a $\Delta m_F = +1$ transition. Thus, the $|F = 2, m_F = 2\rangle$ state is known as a "dark state" since the pump light is not absorbed by the atoms (Lambropoulos and Petrosyan, 2007). In fact, one way to measure the efficiency of optical pumping in a vapor cell is by measuring the intensity of the pump light before and after the vapor cell. In a fully pumped cell, the light should be approximately the same power (taking into account losses due to the cell wall) because atoms pumped to the end state will not absorb the pump light.

2.6 Beer-Lambert Law and Optical Depth

The Beer-Lambert law describes the attenuation of light as it travels through a medium. In our case the medium is an atomic vapor cell filled with warm rubidium atoms. The Beer-Lambert law is written as

$$I(L) = I_0 e^{(-N\sigma L)} \tag{2.7}$$

where N is the density of the atomic vapor in the cell, L is the propagation distance through the medium, σ is the absorption cross section, and I_0 is the initial intensity of the light entering the cell. The optical depth (OD) is the exponent of the Beer-Lambert law (OD $= N\sigma L$). If the OD ≤ 1 the vapor is said to be "optically thin" which means most of the light passes through the cell, and "optically thick" if the OD$\gg 1$ which means the light is fully absorbed as it propagates through the cell. For most of the experiments described in the later sections of this thesis, the OD ~ 1.

2.7 Optical Lineshape and Broadening

Transitions between atomic states have a nonzero linewidth. There are three main types of excited state broadening which are relevant for warm atom atomic systems.

The first is the natural line width, $\Gamma_{nat} = \frac{1}{\Delta t}$, which arises from the uncertainty in energy and time given by the Heisenberg uncertainty principle $\Delta E \Delta t \geq \hbar$. This results in a linewidth of $\sim 2\pi \times 5.75$ MHz for ^{87}Rb.

The second type of broadening, Γ_{pr}, is known as pressure broadening and typically arises from collisions between the atomic species and buffer gas, with the broadening depending on the number density of the atomic medium. Atoms in a dense gas collide more frequently than atoms in a gas with low density, which decreases the average time between collisions, and increases the linewidth. For buffer gas pressures used in magnetometry experiments pressure broadened linewidths are typically on the order of a few GHz to several hundred GHz (Oreto et al., 2004).

The third type of broadening is called Doppler broadening, Γ_{dop}, and it is similar to the Doppler effect with sound (Rayleigh, 1896). When an atom is traveling along the propagation direction of a laser beam the laser frequency is shifted in the reference frame of the atom. This means that light detuned from the atomic resonance can still be absorbed by atoms whose velocity allows them to be resonant with the light. In mathematical terms we write the Doppler broadening as

$$\Gamma_{dop} = 2\frac{v_o}{c}\sqrt{\frac{2k_BT}{M}\ln(2)} \tag{2.8}$$

where v_0 is the resonance frequency, c is the speed of light, k_B is the Stephan-Boltzman constant, T is the temperature, and M is the mass of the atom.

In atomic systems where Γ_{dop} is not a strong broadening mechanism ($\Gamma_{dop} \ll \Gamma_{pr}$) the resonance absorption dip can be modeled by a Lorentzian function given by

$$\xi(v) = \left(\frac{\Gamma_{tot}/2\pi}{((v-v_0)^2 + (\frac{\Gamma_{tot}}{2})^2)}\right) \tag{2.9}$$

where v is the frequency of the laser. However, if Γ_{dop} is the larger contributor to the linewidth ($\Gamma_{dop} \gg \Gamma_{pr}$) a gaussian function is used. In general, if all three broadening mechanism are present in the system, and Γ_{dop} and Γ_{pr} are both significant contributers to the linewidth, a Voight profile is needed (Weller, 2013)

2.8 Ground State Buffer Gas Shift

While buffer gas broadens the excited state resonance linewidth, it narrows the ground state linewidth, making it useful for applications which benefit from longer ground state decoherence times. It also shifts both the hyperfine resonance frequency and the frequency of the optical resonances, although here we focus on the ground state frequency shift. The shift arises from phase shifts in the dipole moment of the rubidium atoms as collisions with the buffer gas occurs. In general, it is difficult to theoretically determine the buffer gas shift. For a limited temperature range, the

buffer gas shift can be empirically modeled as

$$\Delta v = P_0[\beta + \delta(T - T_0) + \eta(T - T_0)^2] \tag{2.10}$$

where β, δ, and η are coefficients which can be found in Bean and Lambert (1976), T is the temperature, T_0 is the reference temperature, and P_0 is the pressure of the buffer gas. Common buffer gases used in experiments are the inert gases N_2, He, and Ne. We perform most of our experimental measurements with N_2 buffer gas which has an approximate hyperfine frequency shift of 548 Hz/Torr (Vanier et al., 1982b) for temperatures used in our experiments. It is also possible to effectively cancel the total buffer gas shift by mixing a buffer gas which positively shifts the frequency with a gas that negatively shifts the frequency (for small temperature ranges). The buffer gas frequency shift plays a large role in our atomic gradiometer, described in Chapter 4, where we use two vapor cells filled with different buffer gas pressures to measure a signal at zero-field gradient.

2.9 Bloch Sphere

A common way to describe a two level system in atomic physics is by using a geometric interpretation known as the Bloch sphere. A diagram of the block sphere is shown in Fig. 2.5(a). On the north and south poles of the sphere we have the states $|2\rangle$ and $|1\rangle$ respectively. In our experiments, we optically pump our atoms to the end-state so the two relevant ground states are $|2\rangle = |F = 2, m_F = 2\rangle$ and $|1\rangle = |F = 1, m_F = 1\rangle$. Any state on the Bloch sphere can be represented by spherical coordinates as

$$|\psi\rangle = \cos(\tfrac{\theta}{2})|2\rangle + e^{i\phi}\sin(\tfrac{\theta}{2})|1\rangle \tag{2.11}$$

where θ and ϕ are angles on the sphere as shown in Fig. 2.5(a). All points, except the exact north and south poles, are superpositions of the two states, and points along the equator are equal superpositions. Points on the surface of the Bloch sphere are pure states, and states inside the sphere are mixed (more info in Section 2.14).

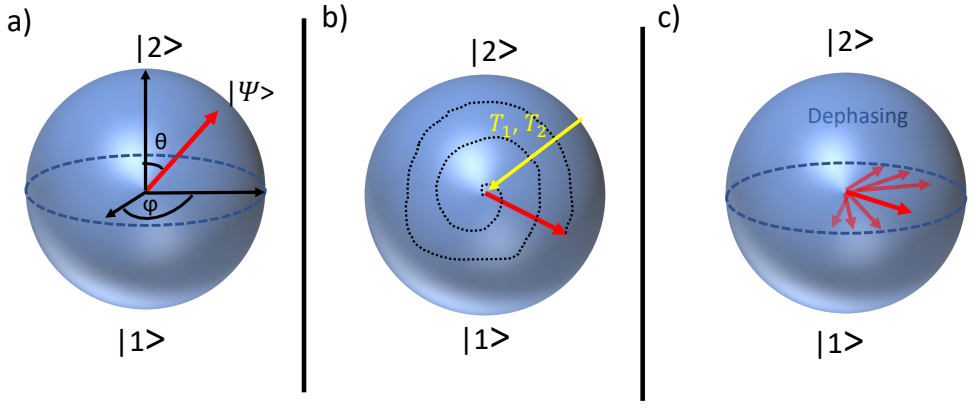

Figure 2.4: (a) A visual representation of Eqn. 2.12. (b) As the Bloch vector oscillates, the atoms undergo Rabi oscillations between states $|2\rangle$ and $|1\rangle$. Both the T_1 and T_2 decay processes result in the Bloch vector relaxing to the origin. (c) A visual representation of the T_2 decay. Phase differences in the spins of the ensemble cause a shortening of the Bloch vector.

2.10 Rabi Oscillations

Electromagnetic waves tuned near the resonance of a two-level system (such as that described by the Bloch sphere) can produce Rabi oscillations, which are oscillations in the atomic population with time. If the atoms are initially prepared in the $|2\rangle$ state on the Bloch sphere, the oscillating field drives stimulated emission which brings the atoms to the ground state. Once in the ground state, stimulated absorption brings them back to the excited state. This oscillation between the two states with time is the essence behind Rabi oscillations. The strength of the Rabi oscillation is proportional to the amplitude of the driving field and the strength of the light-atom coupling (Clebsh-Gordon Coefficients). For the hyperfine ground states, we can write the Rabi frequency as

$$\Omega_R = \frac{\mu_B M_m B_m}{\hbar} \tag{2.12}$$

where subscript m = σ^+, σ^-, π is the polarization of the transition, B_m is the strength of the magnetic coupling field, μ_B is the Bohr magneton, and $M_m = 2\langle S_f|J_m|S_i\rangle$

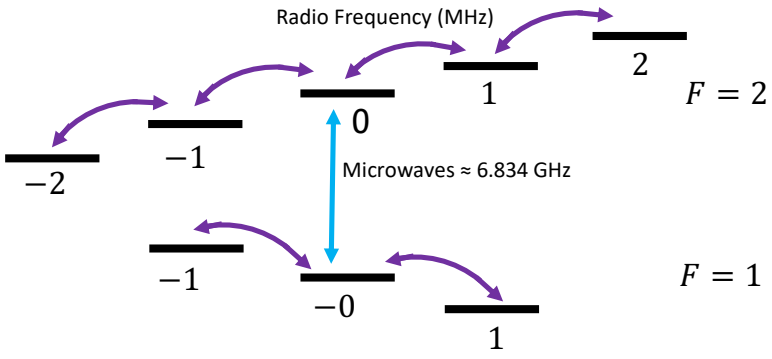

Figure 2.5: (a) A plot showing the hyperfine ground state manifold in ^{87}Rb atoms. RF fields couple the B-field dependent Zeeman transitions, and microwave fields are used to couple between hyperfine ground state transitions. By applying the fields at the correct frequency and for the correct duration, the atomic population can be effectively shifted between the sublevels.

(Horsley and Treutlein, 2016) frequency tunable] is a matrix element which depends on the particular transition and microwave polarization for initial state, i, and final state, f.

2.11 Ground State Control

Rabi oscillations can be used to transfer population between the hyperfine ground states. Shown in Fig. 2.5 is a plot of the hyperfine ground state transitions and the frequencies of the fields that couple the states. The hyperfine transitions are coupled with microwave radiation and Zeeman states are coupled with fields at RF frequencies. By applying microwaves at the frequency of the resonance, we can couple two hyperfine ground states and shift population between the states through Rabi oscillations. However, it is more difficult to couple only two Zeeman states with an RF field for small Zeeman splitting (low B-field) because all of the states are driven by the same frequency, and the population would leak out to all of the other states.

2.11.1 π and $\pi/2$ pulse

In this subsection, we talk about what happens when the Rabi oscillation turns off part way through an oscillation. Let us assume all of the population is pumped to the $|F = 2, m_F = 2\rangle$ hyperfine ground state. If a microwave field tuned to the $|F = 1, m_F = 1\rangle \leftrightarrow |F = 2, m_F = 2\rangle$ is applied, Rabi oscillations will begin between the two states. By turning off the microwave field at $\Omega_R t = \pi/2$ the atoms are in a coherent superposition of the two states. This is known as a $\pi/2$ pulse. If the microwaves are turned on for a time $\Omega_R t = \pi$, or twice the length of time as the $\pi/2$ pulse for the same field strength, then a π pulse has occurred. A π pulse shifts all of the the atomic population from the from the initial state to the final state (ignoring decoherence effects).

2.12 MODR

Microwave-optical double resonance (MODR) is a near resonance effect where both a microwave and optical field are needed to observe an absorption signal in a sample medium. The MODR dip is at its minima when the two fields are on resonance. We describe the MODR effect for a pulsed experiment using a three level system with two ground states $|1\rangle$ and $|2\rangle$ and an excited state $|e\rangle$. The ground states are coupled with a microwave field, and the excited state is coupled to the ground state using an optical transition (pump). In Fig. 2.6(a) the pump field resonant with the $|1\rangle$ to $|e\rangle$ transition optically pumps the atoms to the $|2\rangle$ dark state. The medium is transparent to the probe field since the atoms have collected in the dark state. In Fig. 2.6(b), a resonant microwave field couples the two ground states which means the atomic population is no longer trapped in the $|2\rangle$ state due to Rabi oscillations which shift the atomic population. Now, if we observe the probe signal while sweeping the frequency of the microwave field an absorption dip will be apparent near the microwave resonance since some of the atomic population is now in the $|1\rangle$ state.

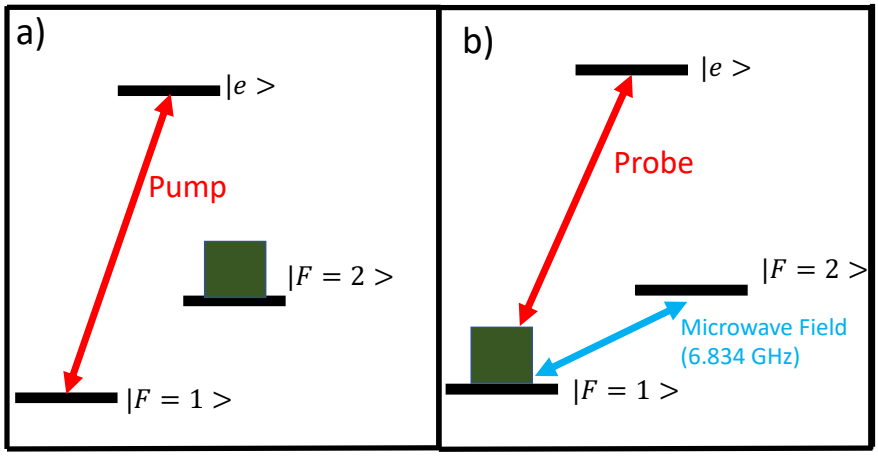

Figure 2.6: Figure showing the MODR process in a pulsed experiment(a) A Pump field is applied from the $|F = 1\rangle$ state to the excited state pumping the atomic population to the $|F = 2\rangle$ state. (b) A microwave field frequency detuned to the splitting between the ground states redistributes the atomic population. A probe beam can then be used to measure the MODR resonance dip.

This absorption dip is the MODR signal. We use the MODR signal in Section 3.8 and compare it to a sideband signal (the topic of this thesis) that we have generated in our vapor cell.

2.13 Atomic Coherence and Decoherence

Coherence is a concept which is truly at the heart of quantum mechanics. Quantum coherence can be thought of as the amount of interference between states in a quantum system. In a two-state system, the Bloch sphere can be used to visualize decoherence and dephasing mechanisms. The longitudinal relaxation time, denoted as T_1, arises when the atomic population relaxes from a position of imbalance towards its thermal equilibrium state. For example, let us say we have a two state system and at thermal equilibrium, barring any interaction with external electromagnetic fields, there is an equal population of atoms in state $|1\rangle$ and state $|2\rangle$. If all of the atomic population is "pumped" to the $|2\rangle$ state by an external field, when the pump field is turned off the

atoms will relax to their original state distribution, with half of the population in each state. The transverse relaxation time, denoted as T_2, is often referred to as the coherence time and includes effects of dephasing as well as population relaxation. In Fig. 2.4(b), we show a two-level system undergoing Rabi oscillations, and relaxation to the origin is caused by both longitudinal and transverse relaxation processes. As shown in Fig. 2.4(c), the transverse relaxation rate is shown to be due to a dephasing of the individual Bloch vectors of each atom, which also results in a shortening of the Bloch vector on the Bloch sphere towards the origin. If the atoms are "pumped" into a state of full atomic coherence, e.g. an equal superposition of the two states, the relaxation of that coherence is given by T_2. The T_2 rate is particularly important for our experiments with sideband generation described in Chapter 3 since sidebands are generated using atomic coherence.

2.14 Density Matrix Formalism

When just a few atoms are present in a system (assuming the ideal case where they are completely isolated from electromagnetic fields and other atoms), it is possible to describe their collective state by writing out their individual wave functions. However, when dealing with a large ensemble of atoms, such as in a cell filled with warm atomic vapor, it becomes effectively impossible to write out the wave functions of each individual atom due to the complexity of their interactions with each other and their environment (decoherence). In order to describe their collective state we use density matrix formalism and take a statistical average of their wave functions.

If all the atoms in an ensemble are in the same state, the atoms are said to be in a pure state. If we define the state of the system as $|\psi\rangle$, its density matrix is given by

$$\rho_{pure} = |\psi\rangle\langle\psi|. \tag{2.13}$$

On the contrary, if all the atoms in an ensemble are not in the same state, and generally this is true, the state of the system is said to be mixed. If N_i atoms are

in the state $|\psi_i\rangle$, where $\sum N_i = N$, the mixed state density matrix is given by the weighted sum of the pure state density matrices

$$\rho_{mix} = \sum p_i |\psi_i\rangle\langle\psi_i| \tag{2.14}$$

where p_i is the probability of each pure state such that $\sum p_i = 1$.

For a two level system $|1\rangle$ and $|2\rangle$, one can write out the density matrix as

$$\rho_{\mu v} = \begin{bmatrix} \rho_{11} & \rho_{12} \\ \rho_{21} & \rho_{22} \end{bmatrix} \tag{2.15}$$

where μ and v are the ground state sublevels. The diagonal elements ρ_{11} and ρ_{22} describe the atomic populations in the $|1\rangle$ state and $|2\rangle$ respectively, while the off-diagonal elements, ρ_{12} and ρ_{21}, describe the coherences between states $|1\rangle$ and $|2\rangle$. It is also of note that the density operator is Hermitian such that $\rho = \rho^\dagger$, and it has only non-negative eigenvalues.

One can use the density matrix formalism to determine the expectation value of an operator. In general, the expectation value of an operator (O) can be given by the following

$$\langle O\rangle = \langle\psi|O|\psi\rangle. \tag{2.16}$$

However, typically the state of a system is unknown, and an ensemble average is used instead. Thus, the expectation value of an operator in a state represented by ρ can be obtained by

$$\langle O\rangle = Tr[\rho O] \tag{2.17}$$

where Tr is the trace operator, which takes a sum of the diagonal elements of a matrix. The density matrix and its formalism is an important tool for describing the state of our atomic ensemble for the sideband generation process described in detail in Chapters 3 and 4.

Chapter 3

Experimental Evidence of Sideband Generation

In this chapter we describe the concept behind the sideband generation process and show data of the first evidence of sideband generation in our experiment. We conduct a steady state pump/probe experiment where we compare the sideband signals to the initial measurements made by Henry Tang in 1973 (Tang, 1973). We then run the experiment in pulsed mode and show how we can extract important information about the atomic system, such as the T_1 and T_2 decay rates from the sideband and MODR signal. Finally, we develop a figure of merit (FOM) that can be used to determine which components of the sideband signal are the most important to the final gradiometer operation, which is described in Chapter 5, and also which buffer gas pressures are optimal for obtaining the strongest sideband signals.

3.1 Steady-State Sideband Experiment

The sideband generation experiments described in this thesis are inspired by experiments performed in the 1970s at Columbia University (Tang, 1973). In their experiments, they prepared alkali atoms in a coherent superposition of hyperfine

ground states by coupling the levels to a microwave magnetic field. They showed that when a weak probe beam is incident on the coherently prepared atoms, sidebands are produced in a process known as parametric frequency conversion (Tang and Happer, 1970, Tang, 1973). The basic idea behind the effect is that the time dependent phase of the atomic coherence oscillates at the hyperfine resonance frequency (taking into account the Zeeman splitting), which modulates the optical susceptibility, χ, of the atomic medium for near resonance light. When the atoms are probed by a weak beam, the oscillating susceptibility generates optical sideband(s). The effect is similar to sidebands which are generated from classical phase or amplitude modulation experiments.

A simplified energy level diagram showing the concept behind sideband generation is shown in Fig. 3.1. We use ^{87}Rb as the atomic species in our experiments so the two hyperfine ground states are $|F = 1\rangle$ and $|F = 2\rangle$ (full energy level structure shown in Section 2.2. To complete the Λ system we label a generic excited state $|e\rangle$. In Fig. 3.1(a) "pump" optical field is resonant with the $|F = 1\rangle \leftrightarrow |e\rangle$ transition which optically pumps (described in Section 2.5) the atoms to the $|F = 2\rangle$ state. In Fig. 3.1(b), a microwave field is concurrently applied which couples the two hyperfine ground states. This coupling puts the atoms in a coherent superposition of the two states. If the superposition between the states is perfect, then a $\pi/2$ pulse has been applied, which is given by $\Omega t = \pi/2$ where Ω is the Rabi frequency. For a steady-state experiment, the pump field cannot be too strong or the microwave coherence will be destroyed, but not too weak such that the pump does not move a significant population of atoms to the desired state. Simultaneously, a probe field is applied which couples one of the ground states (say $|F = 1\rangle$) to the excited state in an optical transition. If the light is coherently scattered from the excited state to the ground state, making the transition $|e\rangle \leftrightarrow |F = 2\rangle$, a sideband is produced. However, due to the very small lifetime of the excited state ($\frac{1}{\pi\Gamma} \sim .3$ ns), spontaneous emission limits the efficiency of the sideband generation process. The frequency of the generated sideband will be offset from the incoming probe frequency by the hyperfine frequency

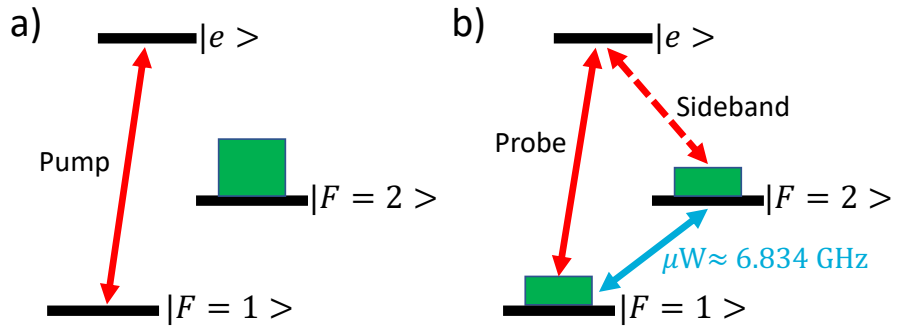

Figure 3.1: Simplified Λ system in a warm ensemble of ^{87}Rb with two ground states $|F = 1\rangle$ and $|F = 2\rangle$ and an excited state $|e>$. (a) The atoms are optically pumped to the $|F = 2\rangle$ state. (b) A microwave field is applied generating a coherence between the two ground state levels. A sideband is produced when a probe is frequency tuned to the $|F = 1\rangle$ state.

($\sim$ 6.834 GHz) due to the fact that the splitting between the coherently coupled states ($|F = 1\rangle$ and $|F = 2\rangle$) is the hyperfine splitting.

In Fig. 3.2 we show an experimental setup for sideband generation. We use an EagleYard distributed feedback (DFB) laser diode, tuned to the D_2 transition in ^{87}Rb (780 nm), which we denote as the "probe" ($\sim$ 10 μW). It is incident on a cubic pyrex atomic vapor cell with internal dimensions of $8 \times 8 \times 8$ mm^3 filled with enriched ^{87}Rb and 30 Torr of nitrogen (N_2) buffer gas. We used a relatively small vapor cell because we eventually use the sideband generation process to build a working gradiometer, and smaller size (Knappe et al., 2006) is better for commercial designs. The buffer gas pressure is determined from experimental measurements and more information is shown in Section 2.8. We apply current to a twisted pair phospher-bronze wire wrapped around the vapor cell to raise the cell temperature. We oscillate the current at high frequency ($\sim$ 200 kHz) so that the time-averaged magnetic field created by the heater current is near zero. A "pump" beam (1 μW $-$10 mW depending on the experiment) tuned to the D_1 transition (795 nm) is directionally orthogonal to the probe and also incident on the vapor cell. A magnetic field is applied along the direction of the pump to define the quantization axis and split the ground state manifold into 8-state hyperfine Zeeman sublevels. A quartz quarter wave plate (QWP)

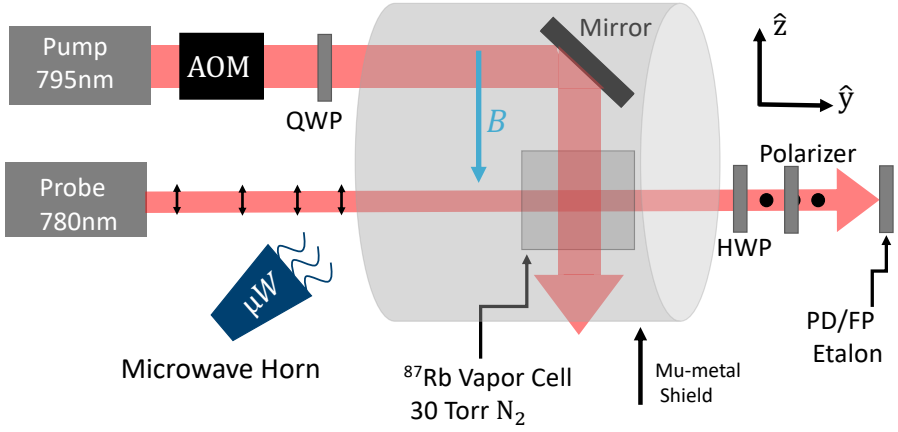

Figure 3.2: Experimental setup to observe sideband generation. A quarter wave plate (QWP) on the pump laser generates σ^+ light. A microwave horn illuminates the atoms with microwaves at the ground state hyperfine frequency of the atoms, producing sidebands on the probe. A polarizer is situated after the cell to allow sideband or probe light to pass. An Acousto-Optic Modulator (AOM) is situated on the probe beam and acts as an optical switch (Continuously on during CW experiments). The atoms are inside a magnetic shield that has a set of internal coils which produce magnetic fields along the y-axis.

circularly polarizes the pump light by applying a $\lambda/4$ retardance to the beam. We use an Acousto-Optic Modulator (AOM) from IntraAction Corp as an optical switch on the pump beam, allowing us to pulse the experiment when needed as shown in Section 3.4 of this chapter. We use a standard gain horn antenna rated at 10 dB, viable at $5.85 - 8.20$ GHz, to probe the atoms with microwave radiation tuned to the hyperfine ground state splitting of ^{87}Rb. The microwave signal is generated by a microwave synthesizer (Berkeley Nucleonics) and is then amplified 35 dB using a high power amplifier from Mini-Circuits (ZVE-3W-183+). For our tabletop experiments we put the vapor cell inside a nickel-iron ferromagnetic alloy (mu-metal) shield, which has a very high permeability and attenuates direct current (DC) or low-frequency magnetic fields. The shield is cylindrically shaped, with an internal solenoid along its longitudinal axis and cosine coils in the transverse directions. This allows for the independent application of magnetic fields in the $\hat{x}$, $\hat{y}$, or $\hat{z}$ directions. The ability to apply magnetic fields in all spatial direction becomes especially important in Chapter 6 where we build a Dead-zone free gradiometer based on the sideband generation

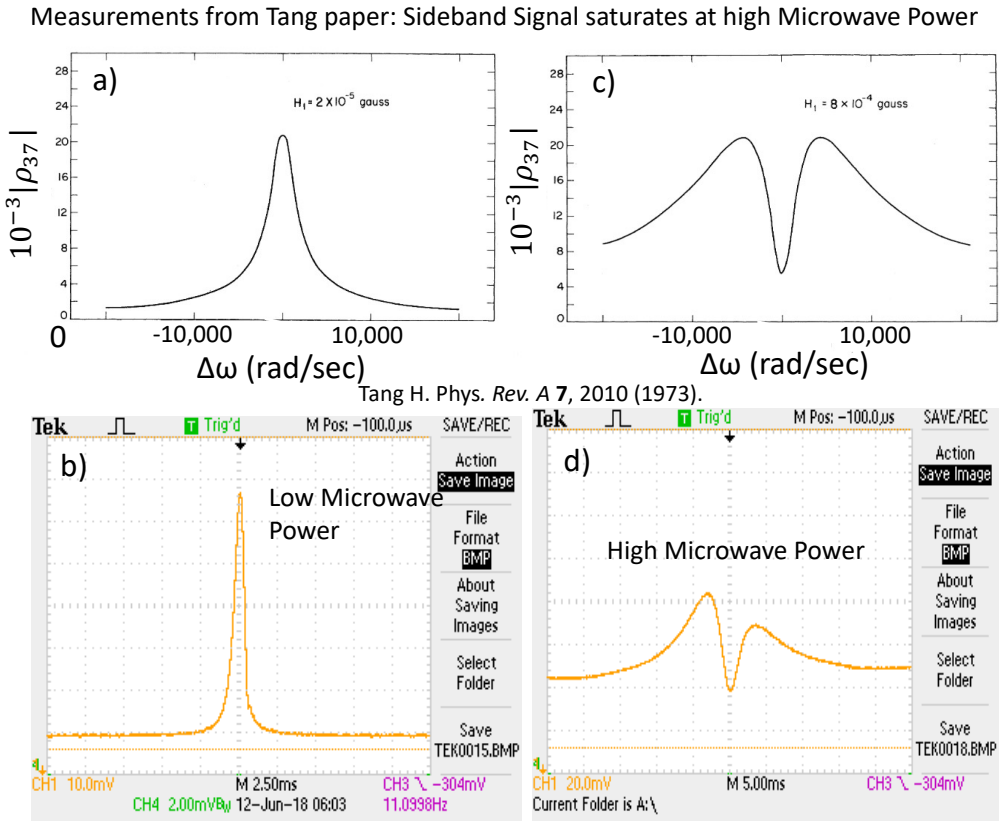

Figure 3.3: A comparison of steady-state sideband signals generated in the lab or Henry Tang in 1973 and signal generated in our lab. (a) Sideband signal generated by Tang (1973) for low microwave power. (b) Signal generated in our laboratory for low microwave power. (c) Sideband signal generated by Tang (1973) for high microwave power (notice saturation of resonance). (d) Sideband signal in our lab for high microwave power (saturation also present)

concept. The shield has two end-caps, and one of them is left off so that microwave radiation can enter the shield. We situate the microwave horn 6 inches away from the vapor cell on the side of the shield without the end cap. Although shielding is not strictly necessary for the sideband generation process, as we show in the resulting gradiometer in Chapter 5, we used shielding in the initial tabletop experiments so we could understand the signals without the added complication of background fields. After passing through the vapor cell, the probe exits the shield and passes through polarizer which we use to isolate the signal photons from the background photons. Since the sideband signal is orthogonally polarized to the probe beam (Section 3.7),

the polarizer works as a polarization selector, allowing the sideband signal to pass and extinguishing the residual probe signal. A high extinction-ratio polarizing beam splitter (PBS) is used as the polarizer in this case. After passing through the polarizer, the light is incident on a silicon switchable gain photodetector (PD), and then the signals are sent by BNC cable to an oscilloscope for analysis.

The first experiment that we completed was to look for evidence of sideband generation and compare to the experiments of Henry Tang in 1973. In Figure 3.3, we show signals from both our experimental setup and from the original setup from Tang (1973) for steady state pump and probe (meaning the experiment is not pulsed i.e the AOM is continuously on). The experiments are not entirely comparable as Tang (1973) used a lamp instead of a laser, among other differences. However, the behavior of the sideband signal should be similar. For these measurements, the probe power was set to 5 μW, and the pump was attenuated to 7 μW using a neutral density filter. For steady-state experiments the pump cannot be too strong or it will destroy the microwave induced coherence, thus the pump and probe have about the same optical power. The pump was tuned to the $|F = 1\rangle$ manifold, hyperfine pumping the atoms to the $|F = 2\rangle$ manifold. For these initial measurements, we set the magnetic field inside the shield to be zero so that we only see a single sideband peak (no splitting due to the Zeeman effect). In Fig. 3.3(a) a we show a sideband signal from Tang (1973) for low microwave power. They measure microwave power in units of magnetic field (Gauss) because the ground state hyperfine transitions are a magnetic dipole transitions. The x-axis is a frequency sweep of the microwave field across the resonance. In Fig. 3.3(b) a sideband signal from our experimental setup is shown as we sweep across the microwave resonance. We know that we are detecting a sideband signal because the probe is rejected by the PBS. For low microwave power we can see that the features in Fig. 3.3(a and b) look similar. In Fig 3.3(c) they increase the microwave power, and the sideband signal begins to saturate. This is due to the fact that the microwave Rabi frequency is much greater than the decoherence rate so more population is transferred to the $|F = 1\rangle$ manifold and less population

is in a coherent superposition of the two states. Fig. 3.3(d) shows our experiment for high microwave power and indeed the signal saturates just as it did in the Tang (1973) experiment. The asymmetry in the signals shown in Fig. 3.3(b and d) is due to a nonlinearity in the microwave fields generated from the microwave synthesizer at fast sweep speeds, with a slower sweep resulting in more symmetric signals.

Sideband generation is dependent on several parameters such as the degree of spin polarization, buffer gas pressure (Section 3.11]), probe detuning from resonance (Section 4.9), and rubidium density (vapor cell temperature). For this experiment the temperature of the vapor cell is adjusted to obtain a rubidium optical depth ~ 1. In experiments at OD > 1, the probe must be detuned from the $|1\rangle \rightarrow |5p^2P_{3/2}\rangle$ or $|2\rangle \rightarrow |5p^2P_{3/2}\rangle$ transitions to maximize sideband generation. At high optical depth, if the probe is not detuned from the resonance, the sideband signal is strongly absorbed along with the probe so not much light passes through the vapor cell. The physical positioning of the microwave horn was tuned to produce the strongest amplitude sideband for the particular microwave transition we were probing. Also, the microwave field reflected off of the walls of the mu-metal shield complicating the polarization of the microwave field, further necessitating the need to optimize the position of the antenna. Under optimal conditions, we found the sideband amplitude to be roughly equal to the probe amplitude after the beam exits the vapor cell.

3.2 Microwave transitions

Nine possible microwave transitions for the ground state of ^{87}Rb are shown in Fig. 3.4. However, the transitions shown in purple and orange are degenerate so there are actually only seven transitions. We label the transitions starting from the $|F = 1\rangle$ manifold and then the Δm_F transition to the $|F = 2\rangle$ manifold as shown in Fig. 3.4. These transitions are important for both sideband generation and MODR signals and this labeling will come up several times over the course of this thesis.

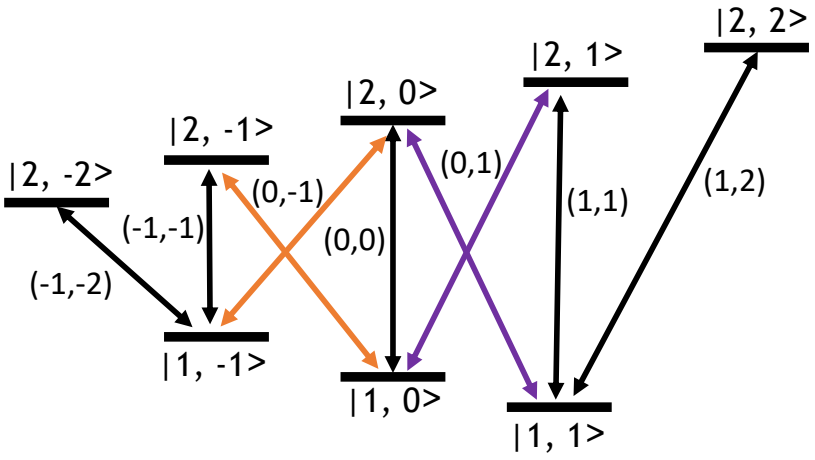

Figure 3.4: The microwave transitions allowable for the hyperfine ground state of ^{87}Rb. The orange and purple transitions are degenerate so there are only seven total transitions for low b-field.

3.3 MODR Magnetometry

In Section 2.12, we define the MODR signal and describe how it is produced. The MODR signal can also be used as a magnetometer to measure the magnetic field that the atoms are subjected to, allowing us to quickly calibrate the magnetic field. When a weak magnetic field (B_z) is applied, setting the quantization axis of the atoms, the Zeeman effect splits the single MODR signal into seven individual signals as shown in Fig. 3.5 due to the seven possible microwave transitions shown in Fig. 3.4. The distance between MODR peaks is dependent on the magnitude of the applied static magnetic field and is given by the Larmor precession frequency

$$\omega_L = \frac{\mu_B B_z}{2\hbar}. \tag{3.1}$$

For ^{87}Rb the Larmor precession frequency is $\sim 2\pi * 7$ Hz/nT. Fig. 3.5(a) shows the MODR signals after sweeping the microwave frequency across the ground state hyperfine resonances. The zero frequency is defined as the frequency of the (0, 0) "clock" transition which is ~6.834610 GHz, and is only shifted by the applied magnetic field to second-order (Güdde et al., 1993). For this case, the pumping field is turned

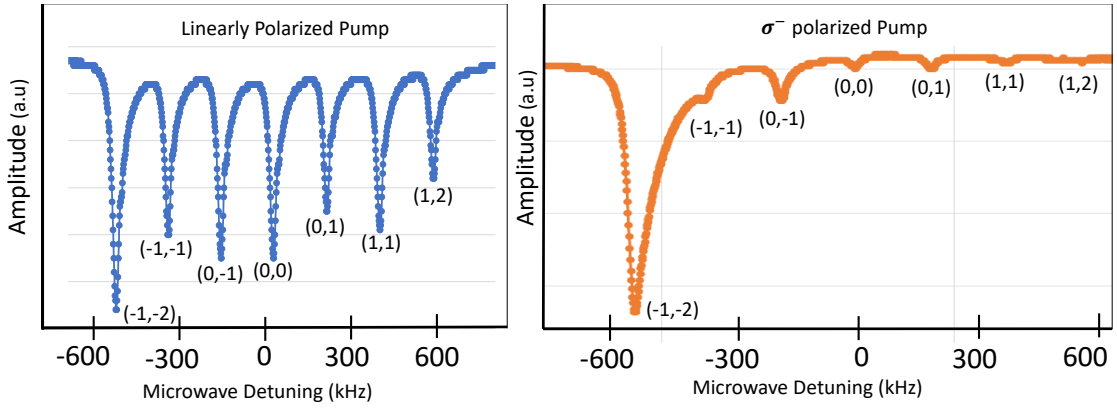

Figure 3.5: (a) Steady-state MODR signals after sweeping the frequency of the microwave field around the zero frequency, which is defined as the middle 0-0 transition ($\sim$ 6.834 GHz). The probe frequency is tuned to the $|F = 1\rangle$ transition and the pump field is turned off. A small magnetic field is applied along the direction of the pump beam splitting the MODR signal into seven due to the Zeeman splitting. (b) A σ^- polarized pump laser is tuned to the $|F = 2\rangle$ state and the atomic population is driven to the end-state of the hyperfine manifold.

off and the linearly polarized probe does the optical pumping, leaving the atomic population relatively evenly distributed between the sublevels. However, there is some asymmetry in the signal towards the (-1, -2) transition due to the probe which may not have been perfectly linearly polarized. The MODR signal is asymmetric due to the speed at which we perform the microwave sweep. Slowing down the sweep eliminates the asymmetry. In Fig. 3.5(b) we turn on a σ^- polarized pump beam tuned to the $|F = 2\rangle$ transition and the population is shifted to the end-state of the hyperfine manifold. This causes the (-1, -2) end-state transition absorption signal to be much stronger than the other transitions due to the much larger percentage of atoms which have been pumped into that state. By measuring the relative amplitudes of the MODR dips, we can observe the quality of the optical pumping, allowing us to tune the QWP on the pump to increase the pumping efficiency.

3.4 Pulsed Operation

Now that we have evidence of sideband generation in our setup and a method to calibrate the magnetic field, we run the experiment in pulsed mode. Pulsed mode is where the pump field is turned on for an amount of time ($\sim$ 1ms) and is then turned off after the atoms are sufficiently pumped. To turn the pump field off during the probing phase we use an AOM as an optical switch. We align the AOM such that approximately 90% of the light is diffracted into the first-order mode. The AOM is driven with an 80 MHz frequency signal. One of the main benefits of running the experiment in pulsed mode is that the pump field can be much stronger because the pump light is turned off when the sideband signal is produced, which means the pump power does not destroy the coherent superposition created by the microwave field. For the pulsed experiment, the microwave field is applied after the pump turns off putting the atoms in a coherent superposition of the two hyperfine ground states, and we turn off the microwave field after a $\pi/2$ pulse has been applied. The sideband signal is maximized immediately after the $\pi/2$ pulse and then decays at the time constant T_2. The AOM driver and pump are triggered by the same function generator, ensuring the fields are pulsed at the correct intervals. Fig. 3.6(a) shows experimental data of the sideband signal generated from the pulsed experiment. The sideband signal is maximized immediately after the $\pi/2$ pulse is applied and then begins to decay. The probe beam does not need to be pulsed since it is weak enough ($\sim 10\mu$W) to not destroy the microwave induced coherence. In Section 3.10 we do test the sideband signal strengths for the case when the probe field is also pulsed.

3.5 T_2 Decay

In Section 2.13 we talk about how the T_2 time is related to the decoherence in an ensemble of atoms. In order to generate sidebands, a coherent superposition of hyperfine ground states is established. We can measure the T_2 time by measuring the

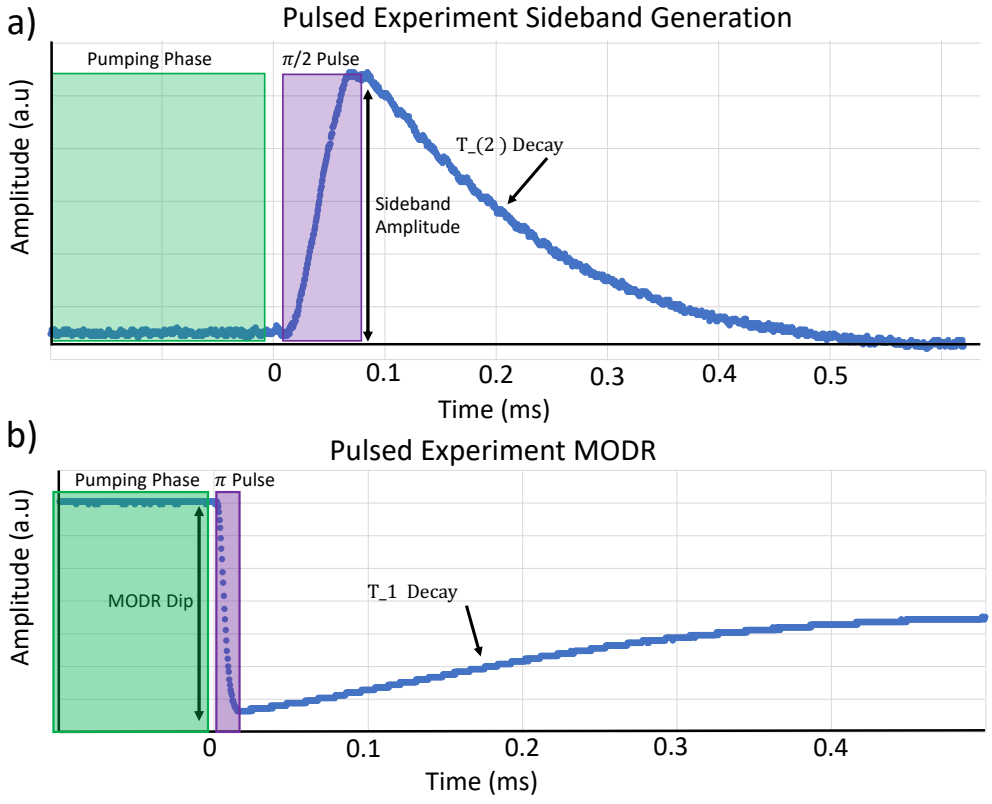

Figure 3.6: (a) Sideband signal for the pulsed experiment. After the pumping phase a $\pi/2$ pulse is applied putting the atoms in a coherent superposition and generating sidebands. The sideband signal then begins an exponential decay at time T_2 from its maximum amplitude. (b) MODR signal for the same experimental configuration. The decay of the MODR signal tells us the T_1 time

decay time of the sideband signal itself, since it directly depends on the strength of the atomic coherence. In order to extract the fit parameters of the signal shown in Fig. 3.6(a) the sideband signal is fit to the decaying exponential

$$Fit(x) = Ae^{-x/T_2} + B \tag{3.2}$$

where A, B, and T_2 are fitting parameters.

3.6 T_1 Decay

As shown in Section 2.13 the T_1 decay is the time it takes for the populations to relax to their original state. One way to measure this is by looking at the pulsed MODR signal and recording how fast it decays. To switch from the MODR signal to the sideband signal we rotate the HWP before the polarizer (shown in Fig. 3.2) by 45^o, which extinguishes the sideband and lets the polarization corresponding to the MODR signal pass. As mentioned in Chapter 2 Section 2.12 an imbalance in population is required for the MODR signal to occur, so the amplitude of the MODR signal should be a direct relation to the T_1 time. Also, notice in Fig. 3.6(b) how the MODR signal does not decay back to its original amplitude, which makes sense because the atomic population is relaxing after being pumped. We can fit the decaying MODR signal to the exponential decay function

$$Fit(x) = Ae^{x/T_1} + B \tag{3.3}$$

and then solve for T_1

3.7 Sideband Selection Rules

The basic selection rules for atomic systems is described in Section 2.4 in Chapter 2. We extend those ideas here to include the selection rules relevant for the generation of sideband signals. When the atoms are pumped to the end-state the relevant ground state sublevels are $|F = 1, m_F = 1\rangle$ and $|F = 2, m_F = 2\rangle$. One can think of the sideband generation process as stimulated Raman transitions (Bateman et al., 2010) (Λ) between ground and excited states, with each Λ system having an incident photon and a stimulated photon. For the experimental configuration of a linearly polarized probe which has its propagation direction orthogonal to the magnetic field, σ^+, σ^-, and π transitions can occur. Fig. 3.7 shows a possible Λ configuration for the negative frequency sideband, with the other two shown in the inset. The

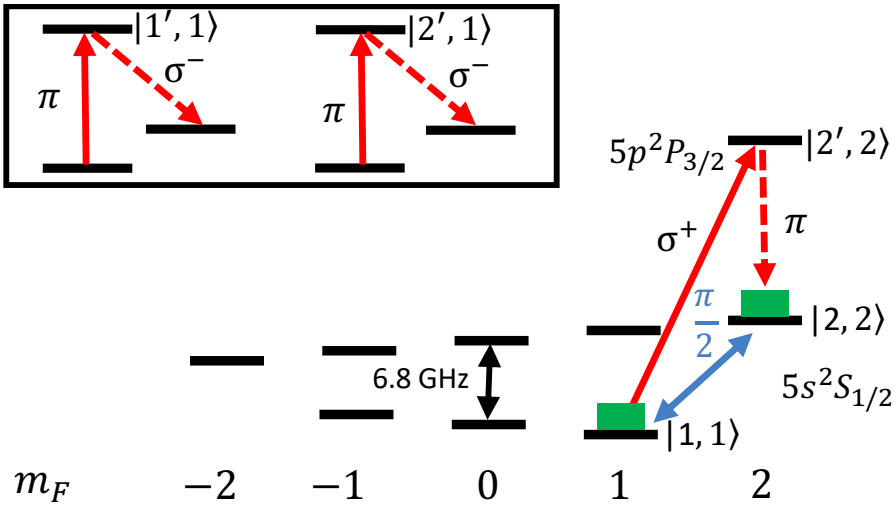

Figure 3.7: Ground state manifold of ^{87}Rb with transitions to an allowable excited state level. An example of a Λ system needed for sideband generation is shown. Also shown in the inset are the other possible transitions when the probe is detuned to the $|F = 1\rangle$ manifold.

probe makes the transitions $|1,1\rangle \xrightarrow{\sigma^+} |2',2\rangle \xrightarrow{\pi} |2,2\rangle$, $|1,1\rangle \xrightarrow{\pi} |2',1\rangle \xrightarrow{\sigma^-} |2,2\rangle$, and $|1,1\rangle \xrightarrow{\pi} |1',1\rangle \xrightarrow{\sigma^-} |2,2\rangle$ where the prime indicates the excited state. For a 1st-order effect, a probe photon (σ polarization) is scattered into the first-order sideband (π polarization), which is orthogonal to the probe polarization. This orthogonality is essential to the operation of the gradiometer described in Chapter 5 due to the fact that the sidebands can be effectively separated from the probe and measured on a photodiode.

3.8 Sideband vs. MODR

We observed an interesting effect which provides strong evidence that we are measuring sideband signals and not spurious signals. To do this, we greatly extend the length of the microwave pulse and look at the Rabi oscillations between the hyperfine ground states. We do this for both the sideband signal and the MODR signal, and we switch between the two experiments by rotating the HWP before the polarization selector to

pass through the particular polarization we want to measure. As shown in Fig. 3.8 the sideband signal oscillates at twice the frequency of the MODR signal. This can be explained by looking at a visual representation of the effect on the Bloch sphere. In Fig. 3.8(a), for no microwave field frequency detuning, the Rabi vector sits on the equatorial plane with the Bloch vector oscillating between the $|1,1\rangle$ and $|2,2\rangle$ states. When the Bloch vector is at the equator of the Bloch sphere, a coherent superposition between the $|1,1\rangle$ and $|2,2\rangle$ states is produced, allowing for the generation of strong sideband signals. As the Rabi vector continues its rotation the sideband signal decays. Thus, the sideband signal will be strongest at two positions over its full rotation on the Bloch sphere because it passes through the equator twice. However, the MODR signal does not behave in the same way and it oscillates at the same frequency that the Bloch vector does. Now, if we detune the microwave frequency by 3 kHz then the sideband signal starts to behave differently. On the Bloch sphere we can think of this as the torque vector tilting up such that it is no longer on the equatorial plane. Now the Bloch vector no longer rotates with symmetry across the equatorial plane, as it spends more "time" in the $|2,2\rangle$ state vs. the $|1,1\rangle$ state. Thus, the sideband signal looks distorted because the maximum amplitude of the sideband occurs at asymmetrical positions. Finally, if we detune the microwaves by a larger amount, say 14 kHz, then the sideband signal oscillates at the same frequency of the MODR signal. In this case the torque vector is tilted far enough off the equatorial plane such that the Bloch vector never reaches the equatorial plane as it rotates (or just reaches it). In this case the maximum sideband amplitude is generated only one time during the Bloch vector's precession. This is a clear illustration of the sideband generation process and a clear indication that coherence is indeed needed to produce sidebands. Also of note, both the sideband and MODR oscillation frequencies increase as the microwave field is detuned from resonance, which is given by the effective Rabi frequency equation, $\Omega_{tot} = \sqrt{\Omega_R^2 + \Delta^2}$ [1], where Ω_R is the Rabi frequency and Δ is the detuning.

[1] http://info.phys.unm.edu/~ideutsch/Classes/Phys566F21/index.html

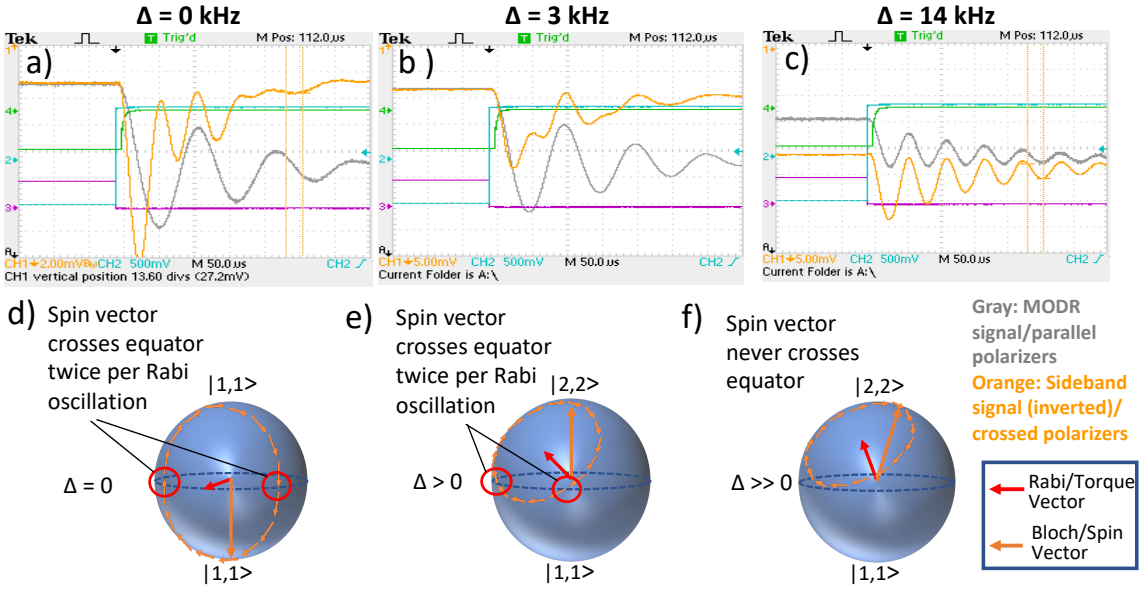

Figure 3.8: This plot provides further evidence of sideband generation. (a) The sideband signal (Orange) and the MODR signal (Grey) are shown on the same plot on an oscilloscope for $\Delta = 0$. The sideband signal oscillates at twice the frequency of the MODR signals in this case. (b) When the microwave field is detuned by 3 kHz the sideband signal oscillates asymmetrically. (c) For larger detunings, 14 kHz, the sideband and MODR signal oscillate at the same frequency. (d-f) Bloch sphere explanation for the MODR and sideband signals.

3.9 Microwave Power Calibration

One way to calibrate the power of the microwave field is by measuring the Rabi frequency of the atoms. When the power of the microwave field is increased the Rabi oscillation frequency also increases and the relationship is linear. The equation for Rabi frequency is given by

$$\Omega_R = \frac{\mu_B g_F B_H}{2\hbar} \tag{3.4}$$

where g_F is the hyperfine Lande g-factor which is ~ 2 for ^{87}Rb, μ_B is the familiar Bohr magneton, and B_H is the microwave magnetic field. Fig. 3.9(a) shows the calibration for Rabi frequency with respect to the microwave magnetic field. In Fig. 3.9(b) we show the magnetic field calibration with respect to the microwave power in dBm. For high power, the microwave amplifier begins to saturate. This gives us an

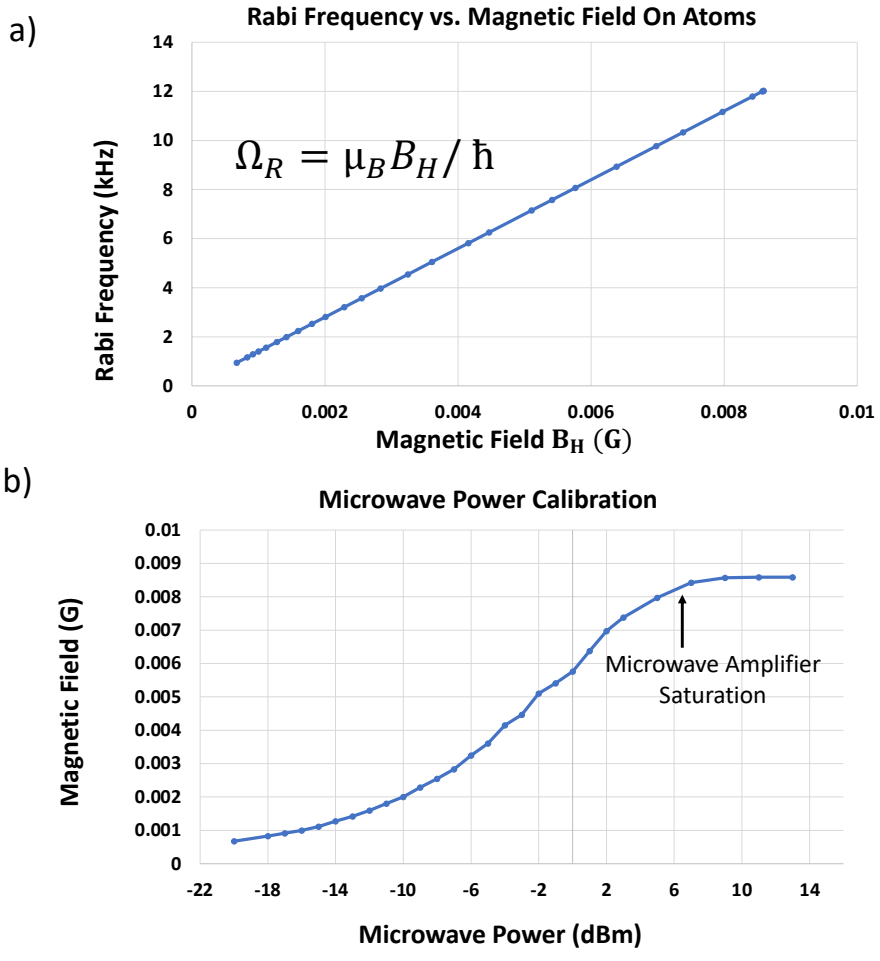

Figure 3.9: (a) Rabi frequency to microwave magnetic field calibration. (b) Magnetic field to microwave power in (dBm) calibration.

effective calibration for the microwave field so we know how much power the atoms see for each dBm setting on the microwave synthesizer.

3.10 Sideband Generation at Zero-Intensity

We measured sideband generation for the case when the optical probe field is pulsed to see if the probe power has a large effect on the T_2 decay time. For these measurements, the probe power was 12 μW. Fig. 3.10 provides a visual description of the zero-intensity probe experiment. This experiment starts off the same as Fig. 3.6 with a

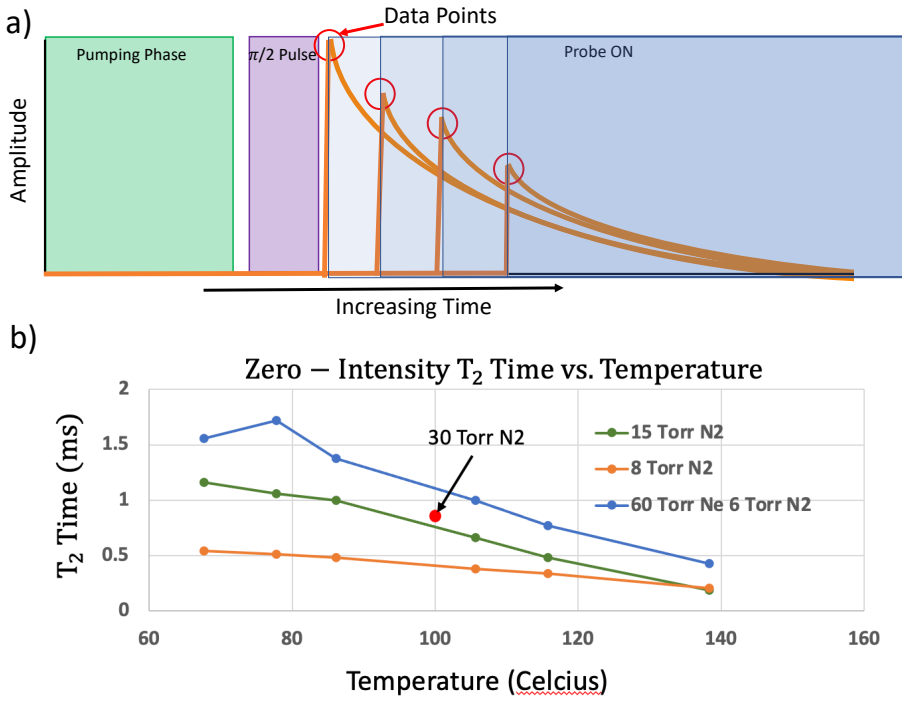

Figure 3.10: A conceptual diagram showing how the zero-intensity sideband is measured. After the Pump pulse and microwave pulse the probe pulse is applied at several different times. The red circles show the data points recorded for the Zero-intensity sideband amplitude as the probe delay time is increased. The progressively darker blue squares show the position of the probe pulse at the positions of the recorded data points.(b) Zero-intensity T_2 decay times for several different buffer gas pressures with respect to Number Density.

pulsed probe and a microwave $\pi/2$ pulse. The pulsed probe is implemented using a function generator to set an adjustable delay time for the probe power so we can make measurements of the sideband amplitude over the entire T_2 decay. For example, in Fig. 3.10 the red circles show the data points recorded for the zero-intensity sideband amplitude as the probe delay time is increased. The progressively darker blue squares show the position of the probe pulse as the data points are measured over the length of the decaying signal. Then, data is recorded and fit to Eqn. 3.2 to extract the T_2 time for the zero-intensity probe beam. In Fig. 3.10(b) we show a plot of the T_2 times for the zero-intensity sideband.

3.11 Buffer Gas Experiments

The sideband generation signal amplitude and T_2 time can be affected by the buffer gas present in the atomic vapor cell. For the next few sections of this chapter, we place vapor cells with varying amount of buffer gas in the experiment to test the effect they have on the sideband signal. We use N_2 buffer gas for most of the measurements, however one cell did have some helium. Buffer gas can be used to to minimize depolarization from cell wall collisions and to limit radiation trapping (Rosenberry et al., 2007), which reduces the optical pumping efficiency (HAPPER, 1972). However, if the buffer gas pressure is too high, pressure broadening (Oreto et al., 2004) of the $5^2P_{3/2}$ excited state causes off-resonant excitation to ground states which increase the absorption of the sideband signal, reducing its conversion efficiency.

3.12 Calculating Number Density

For the buffer gas experiments, we plot the sideband amplitudes with respect to cell temperature. As the temperature increases, the density of alkali atoms increases in the vapor cell. In order to estimate the number density of the atomic ensemble for for a broad range of temperatures we use a couple of methods. First, the number density can be estimated by first calculating the vapor pressure and then converting that to number density. The vapor pressure equation for the liquid phase of rubidium is given by Steck (2003)

$$\log_{10} P_V = 15.88253 - \frac{4529.635}{T} + .00058663\ T - 2.99138\ \log_{10} T \tag{3.5}$$

where P_V is the vapor pressure in Torr and T is the temperature in K. Now, to convert this to number density, we use the ideal gas law given by

$$\frac{N}{V} = \frac{P_V}{k_B T} \tag{3.6}$$

where N/V is the number density and k_B is the Boltzman constant. However, this method is not infallible because it requires a measurement of the temperature of

the vapor cell, which may be inaccurate. We measure the vapor cell temperature by taping (We use Kapton tape for its resistance to high temperature) a thermocouple, Type E since they are less magnetic, near or on the outside of the vapor cell wall. The placement of the thermocouple can have a large impact on the temperature measurement due to inhomogeneities in temperature on the cell wall. For example, locations next to the twisted pair heater will be hotter than locations in the middle of the vapor cell. Another way to measure density is by measuring the absorption of light as it passes through the vapor cell, since the amount of absorption is related to the density of atoms. This can be clearly seen in Section 2.6 on Beers law where the light intensity depends on the density of the atoms. First, we sweep the optical frequency across the hyperfine resonances. Only the $|F = 1\rangle$ and $|F = 2\rangle$ transitions are visible because of broadening effects, in particular the addition of buffer gas, which renders the other excited state transitions unresolved. Then, we record the spectral profile and fit it to the Eqn. 2.7 (see Section 2.6). However, at high optical depth the equation has two substantially intertwined parameters, the density and the linewidth, so we will cannot just do a fit and extract the density. In order to measure the linewidth, we lower the temperature so that the OD is $\ll 1$. When the OD is low the linewidth doesn't change much with density (due to the functional form of the lorentzian lineshape) so the linewidth can be extracted. Then, for large OD, the estimated linewidth from the previous calculation can be inputed and the density can be extracted. More information about the broadening mechanisms are shown in Section 2.7. Now that we have the linewidth, the number density can be backed out from the fit equation

$$\text{Fit(x)}= (A + Bv + Cv^2)e^{(\frac{5}{8}N_1 L\ \sigma_1(v-v_0))}e^{(\frac{3}{8}N_2 L\ \sigma_2(v-v_0))} \tag{3.7}$$

where $\sigma_{1,2}(v - v_0) = \pi r_e c f \xi(v)_{1,2}$ is the absorption cross section for either the $F = 1$ or $F = 2$ ground state, and L is the length of the vapor cell. In the fit equation, the $F = 2$ transition is multiplied by $\frac{5}{8}$ because there are five sublevels in the manifold and the $F = 1$ transition is multiplied by $\frac{3}{8}$ because there are 3 sublevels in this

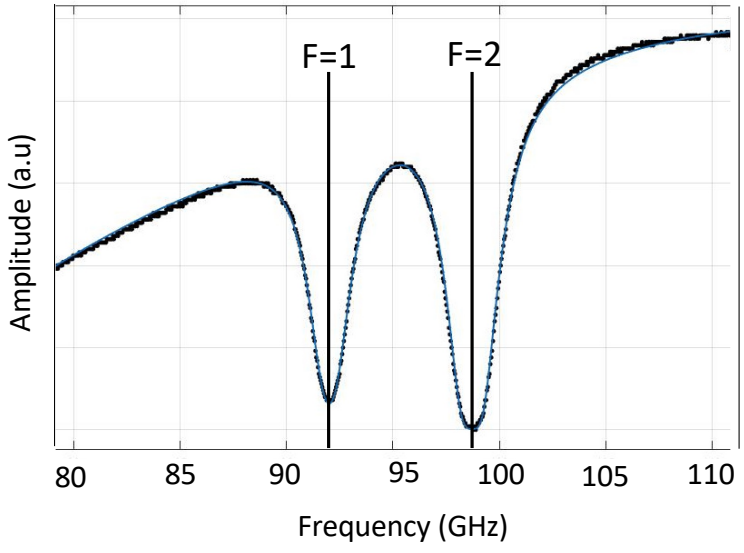

Figure 3.11: An example of an absorption dip on the D_2 line in ^{87}Rb with the $|F = 1\rangle$ and $F = 2\rangle$ resonances clearly visible. The excited state hyperfine levels are not resolved due to the addition of buffer gas which broadens the line.

manifold. Also, the fit equation is multiplied by a polynomial equation in order to compensate for the effects due to the laser. As we increase the amplitude of the current to the laser diode, the power changes along with the frequency in a mostly linear fashion. Another way to do this is to remove the vapor cell and measure the amplitude of the laser as the current is swept. Then each point in the absorption curve could be divided by the resulting line.

3.13 Conversion Efficiency: Two Definitions

In the first experiment we define a conversion efficiency for the sideband generation process and measure it for multiple buffer gas types and pressures. The vapor cells we use are 60 Torr Ne, 6 Torr N_2, 30 Torr N_2, 15 Torr N_2, 8 Torr N_2, and also a parrafin coated cell. However the parrafin coating begins to melt at temperatures of 80^oC so we could not increase the number density in that cell to the optimal amount

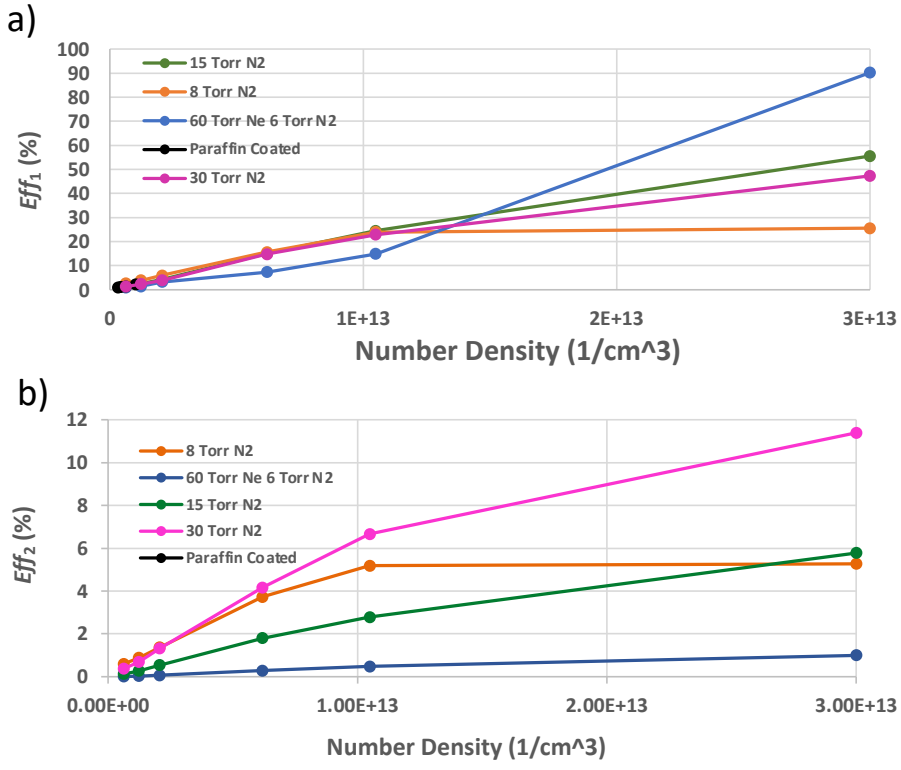

Figure 3.12: (a) The conversion efficiency of the sideband vs. number density. (a) Conversion efficiency for the first definition given in equation 3.8. (b) Conversion efficiency for the second definition given by equation 3.9.

for sideband generation. The amplitude of the sideband needs to be defined with respect to a reference so that we can know how efficient our sideband conversion is. We use two different definitions for conversion efficiency. The first definition compares the sideband amplitude to the amplitude of the MODR signal and is given by

$$Eff_1 = \frac{S_A}{M_A} \tag{3.8}$$

where S_A is the sideband amplitude and M_A is the MODR amplitude. This comparison gives us an idea of how much light is being scattered into the sideband mode compared to the amount of light that is absorbed in the MODR resonance. The second definition determines the percentage of the incoming probe power that is converted to sideband power and is given by

$$Eff_2 = \frac{S_A}{I_P} \tag{3.9}$$

where I_P is the input power of the probe. Fig. 3.12 shows the sideband conversion efficiencies for the previously described buffer gas pressures for both definitions of conversion efficiency.

3.14 Figure of Merit

Since we eventually use the sideband generation process to build a novel atomic gradiometer, we develop a Figure of Merit (FOM) to determine which sideband parameters are most important for the operation of the device. For a Poisson distribution the noise in the signal is proportional to the square root of the amplitude. Using this analogy we write the FOM as

$$FOM = \frac{\sqrt{S_A(\mu W)}}{\eta_L(\frac{1}{s})} \tag{3.10}$$

where S_A is the signal amplitude given in μW and η_L is the transverse decoherence linewidth given by $\frac{1}{\pi T_2}$. It is also useful to look at the FOM at zero-intensity probe and when the probe is always on. Fig. 3.13 shows a plot of the FOM for both the CW probe case (a) and the zero-intensity probe case (b). Although small, the FOM is better for the zero-intensity case which shows us that the probe does have a negative effect on the sideband signal decoherence. From the data in Fig. 3.13 it is clear that the 30 Torr buffer gas cell outperformed the others, with the 8 Torr and 15 Torr cells also performing well. The FOM experiments informed our selection of buffer gas for the gradiometer described in Chapter 5 of this thesis, where we use the 30 Torr buffer gas pressure cell and the 15 Torr buffer gas pressure cell.

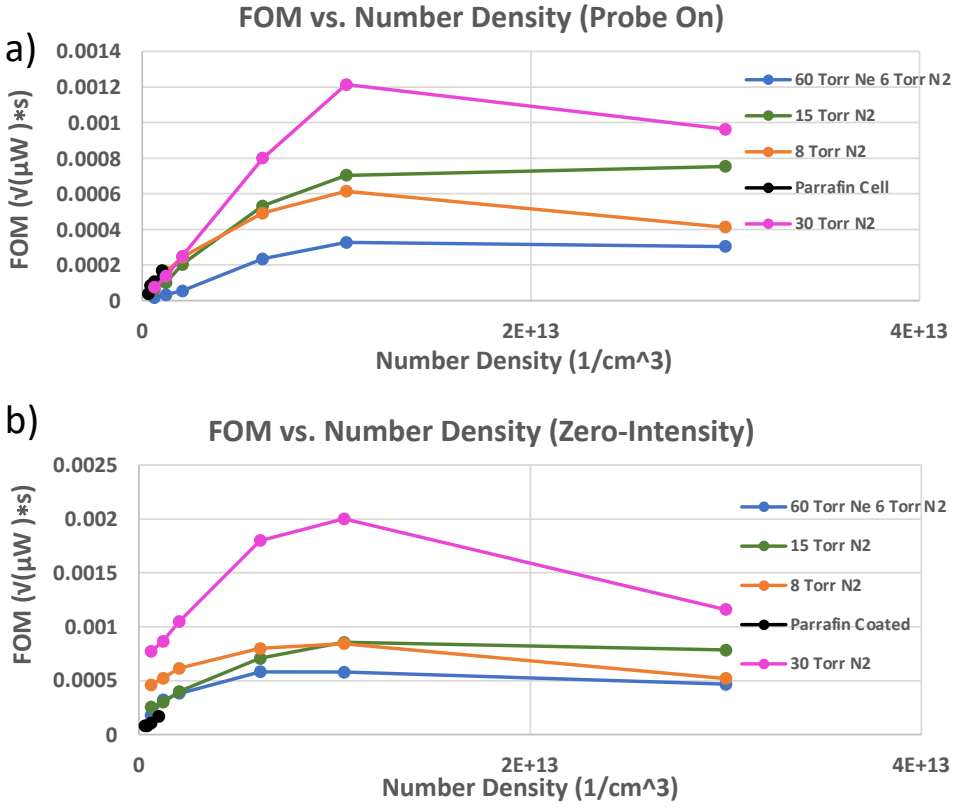

Figure 3.13: FOM for multiple buffer gas pressures is shown for different number densities of the rubidium vapor. (a) FOM for the case of a CW probe beam (b) FOM for the case of a zero intensity probe beam. In this case, the probe is pulsed and amplitudes are measured immediately after the probe is turned on.

Chapter 4

Derivation of Sideband Propagation: Numerical Model

In this chapter we describe the propagation of a classical electromagnetic field through a warm atomic vapor. We then build a numerical model and solve the propagation equation for relevant experimental parameters, accurately modeling the sideband process described in Chapter 3. We then show plots of first and second-order sideband amplitudes with respect to propagation distance through the vapor cell. We end the chapter by performing an experiment where we measure the amplitude of the sideband and probe light as they pass through the vapor cell as a function of probe detuning and fit the experimental data to the numerical model, which shows excellent agreement.

4.1 Maxwell's Equations

The sideband generation process is explained qualitatively in Chapter 3. To recap, if a coherence is established between two hyperfine ground state transitions, and the incoming optical field is sufficiently close to a ground state resonance, sidebands are produced as the field propagates through the medium. The sideband generation

process is similar to an electro-optic modulator, where a crystal is modulated at a frequency and produces sidebands at the modulation frequency (or some multiple of the modulation frequency for higher-order sidebands) away from the probe frequency. In our case, a microwave field is used to establish a coherence between two hyperfine ground states, and the generated sidebands are offset from the incoming beam by the frequency of the hyperfine ground state splitting. In this chapter, we describe a numerical model that was developed to better understand the sideband generation process and to accompany our experimental progress. The derivation of the propagation equation has been adapted from an unpublished note from Jau and the book "Optically Pumped Atoms" (Happer et al., 2010).

We start with Maxwell's macroscopic equations in MKS units:

$$\nabla \cdot \mathbf{D_e} = \rho, \tag{4.1}$$

$$\nabla \cdot \mathbf{B} = 0, \tag{4.2}$$

$$\nabla \times \mathbf{E} = -\frac{\partial \mathbf{B}}{\partial t}, \tag{4.3}$$

and

$$\nabla \times \mathbf{H} = \frac{\partial \mathbf{D_e}}{\partial t} + \mathbf{J}. \tag{4.4}$$

The electric displacement field, $\mathbf{D_e}$, can be written as

$$\mathbf{D_e}(\mathbf{r}, t) = \epsilon_0 \mathbf{E}(\mathbf{r}, t) + \mathbf{P}(\mathbf{r}, t) \tag{4.5}$$

where $\mathbf{E}(\mathbf{r}, t)$ is the electric field and $\mathbf{P}(\mathbf{r}, t)$ is the polarization density, ϵ_0 is the vacuum permittivity, $\mathbf{B}$ is the magnetic flux density, and $\mathbf{H}$ is the magnetic field strength.

Using Maxwell's equations, we derive an equation that describes the propagation of low-intensity light through a thermal atomic medium. We assume no spatial charge

$\rho = 0$, current source $\mathbf{J} = 0$, and no magnetic susceptibility such that $\mathbf{B} \approx \mu_0 \mathbf{H}$, where μ_0 is magnetic permeability in a vacuum.

By taking the curl of both sides of Eqn. 4.3 we rewrite it as

$$\nabla \times (\nabla \times \mathbf{E}) = -(\nabla \times \frac{\partial \mathbf{B}}{\partial t}). \tag{4.6}$$

Using the vector triple product identity:

$$a \times (b \times c) = (a \cdot c)b - (a \cdot b)c, \tag{4.7}$$

we can write the left hand side of Eqn. 4.5 as $\nabla \times (\nabla \times \mathbf{E}) = \nabla(\nabla \cdot \mathbf{E}) - \nabla^2 \mathbf{E}$, where ∇^2 is a vector Laplace operator.

For a one-dimensional plane wave traveling in the ζ direction, the first term $(\nabla \cdot \mathbf{E})$ vanishes since $\rho = 0$ and the second term $(\nabla^2 \mathbf{E})$ becomes $\frac{\partial^2 \mathbf{E}}{\partial \zeta^2}$. The right hand side of Eqn. 4.6 after substituting Equation 4 can be written as

$$-(\nabla \times \frac{\partial \mathbf{B}}{\partial t}) = -\mu_0 \frac{\partial (\nabla \times \mathbf{H})}{\partial t} = -\mu_0 \frac{\partial}{\partial t} \frac{\partial \mathbf{D_e}}{\partial t}. \tag{4.8}$$

Bringing both sides of Eqn. 4.6 together, we write

$$\frac{\partial^2 \mathbf{E}}{\partial \zeta^2} = \mu_0 \frac{\partial^2 \mathbf{D_e}}{\partial t^2}. \tag{4.9}$$

For the case of atoms in a vapor cell, $\mathbf{P}(\mathbf{r}, t)$ can be written as a density of electric dipoles:

$$\mathbf{P}(\mathbf{r}, t) = N \left\langle \mathbf{D}(\mathbf{r}, t) \right\rangle, \tag{4.10}$$

where N is the number density of the atoms and $\langle \mathbf{D}(\mathbf{r}, t) \rangle$ is the average electric dipole moment of the atoms. By substituting Eqn. 4.10 in Eqn. 4.5, we can rewrite $\mathbf{D_e}$ as

$$\mathbf{D_e}(\mathbf{r}, t) = \epsilon_0 \mathbf{E}(\mathbf{r}, t) + N \left\langle \mathbf{D}(\mathbf{r}, t) \right\rangle. \tag{4.11}$$

Substituting Eqn. 4.11 in Eqn. 4.9, we arrive at

$$\frac{\partial^2 \mathbf{E}(\mathbf{r}, \mathbf{t})}{\partial \zeta^2} = \mu_0 \epsilon_0 \frac{\partial^2 \mathbf{E}(\mathbf{r}, \mathbf{t})}{\partial t^2} + \mu_0 \frac{\partial^2 \mathbf{N} \left\langle \mathbf{D}(\mathbf{r}, \mathbf{t}) \right\rangle}{\partial t^2}. \tag{4.12}$$

We can think of this as Maxwell's wave equation, which describes the propagation of $\mathbf{E}(\mathbf{r}, \mathbf{t})$ through an atomic medium of number density N.

4.2 Time-independent Evolution of the Electric Field

We are interested in static propagation of the electric field, since light travels through the length of our medium much faster than the transverse decoherence time, T_2. In other words, as the light propagates, the atoms do not have time to decay substantially before the light exits the cell. For this model, we are interested in the maximum achievable sideband amplitude immediately after the length of the vapor cell and when the atoms are in their prepared state and the coherence is maximized. Afterwards, the atomic coherence will begin to relax and the sideband amplitude will decrease, and we can fit the sideband signal to an exponential decay.

Taking this into account, we employ the method of the Fourier transform to write the fields in terms of frequency. It can be used to describe any function as a sum of its constituting frequency components. For both $\mathbf{E}(\mathbf{r},t)$ and $\langle\mathbf{D}(\mathbf{r},t)\rangle$, we write their Fourier transforms as

$$\mathbf{E}(t,\mathbf{r}) = \int \tilde{\mathbf{E}}(\omega,\mathbf{r})e^{-i\omega t}d\omega \tag{4.13}$$

and

$$\langle\mathbf{D}(\mathbf{r},t)\rangle = \int \left\langle\tilde{\mathbf{D}}(\omega,\mathbf{r})\right\rangle e^{-i\omega t}d\omega, \tag{4.14}$$

where $\tilde{\mathbf{E}}(\omega,\mathbf{r})$ and $\left\langle\tilde{\mathbf{D}}(\omega,\mathbf{r})\right\rangle$ represent frequency components of $\mathbf{E}(\mathbf{r},t)$ and $\langle\mathbf{D}(\mathbf{r},t)\rangle$, correspondingly, and ω represents the frequency space.

In order to eliminate the time dependence, we need to remove the phase term ($e^{-i\omega t}$). First, we take a second derivative with respect to time of Eqns. 4.13 and 4.14. They become

$$\frac{\partial^2\langle\mathbf{D}(t,\mathbf{r})\rangle}{\partial t^2} = -\omega^2\int\left\langle\tilde{\mathbf{D}}(\omega,\mathbf{r})\right\rangle e^{-i\omega t}d\omega \tag{4.15}$$

and

$$\frac{\partial^2 \mathbf{E}(t,\mathbf{r})}{\partial t^2} = -\omega^2 \int \tilde{\mathbf{E}}(\omega,\mathbf{r}) e^{-i\omega t} d\omega. \tag{4.16}$$

Using the Fourier transform, we can rewrite the left hand side of Eqn. 4.12 as a function of frequency as

$$\frac{\partial^2 \mathbf{E}(t,\mathbf{r})}{\partial \zeta^2} = \int \frac{\partial^2 \tilde{\mathbf{E}}(\omega,\mathbf{r})}{\partial \zeta^2} e^{-i\omega t} d\omega. \tag{4.17}$$

We then substitute Eqns. 4.15, 4.16 and 4.17 into Eqn. 4.12 and obtain

$$\int \frac{\partial^2 \tilde{\mathbf{E}}(\omega,\mathbf{r})}{\partial \zeta^2} e^{-i\omega t} d\omega = -\omega^2 \int (\mu_0 \epsilon_0 \frac{\partial^2 \tilde{\mathbf{E}}(\omega,\mathbf{r})}{\partial t^2} + \mu_0 \frac{\partial^2 \mathbf{N} \left\langle \tilde{\mathbf{D}}(\omega,\mathbf{r}) \right\rangle}{\partial t^2}) e^{-i\omega t} d\omega \tag{4.18}$$

We then eliminate the integrals and the time-dependent phase term (e^{-iwt}) on both sides and rewrite the time-independent electric field propagation equation as:

$$\frac{\partial^2 \tilde{\mathbf{E}}(\omega,\mathbf{r})}{\partial \zeta^2} = -\omega^2 \mu_0 (\epsilon_0 \tilde{\mathbf{E}}(\omega,\mathbf{r}) + N \left\langle \tilde{\mathbf{D}}(\omega,\mathbf{r}) \right\rangle). \tag{4.19}$$

4.3 Atomic Coherence and Polarizability

In order to evaluate the propagation for an atomic ensemble, we need to include the effects of atomic coherence and polarizability on the incoming probe light. To do this, we introduce the density matrix, defined in Section 2.14, which allows us to describe the state of the atomic ensemble, as well as the coherent interactions between them.

The average electric dipole moment can be further expanded as

$$\left\langle \tilde{\mathbf{D}}(\omega,\mathbf{r}) \right\rangle = \left\langle \boldsymbol{\alpha}(t,\omega) \right\rangle_\rho \tilde{\mathbf{E}}(w,\mathbf{r}) \tag{4.20}$$

where $\left\langle \boldsymbol{\alpha}(t,\omega) \right\rangle_\rho$ is the average value of the frequency dependent polarizability tensor.

In order to solve for the expectation value of the observable $\boldsymbol{\alpha}(t,\omega)$, we use density matrix formalism and write

$$\left\langle \boldsymbol{\alpha}(t,\omega) \right\rangle_\rho = Tr(\boldsymbol{\rho}(t,\mathbf{r}) \boldsymbol{\alpha}(\omega)) \tag{4.21}$$

where $Tr[.]$ is a trace operator, which when applied to a matrix is the sum of the diagonal elements, $\boldsymbol{\rho}(t, \mathbf{r})$ is the time and space dependent density matrix and $\boldsymbol{\alpha}(\omega)$ is the frequency dependent polarizability.

We can further modify the time-independent propagation equation (Eqn. 4.19) by incorporating Eqn. 4.20 as

$$\frac{\partial^2 \tilde{\mathbf{E}}}{\partial \zeta^2} = -\omega^2 \mu_0 (\epsilon_0 \tilde{\mathbf{E}}(\omega, \mathbf{r}) + N \left\langle \boldsymbol{\alpha}(t, \omega) \right\rangle_\rho \tilde{\mathbf{E}}(w, \mathbf{r})). \tag{4.22}$$

This can be further simplified as:

$$\frac{\partial^2 \tilde{\mathbf{E}}}{\partial \zeta^2} = -\mu_0 \epsilon_0 \omega^2 (1 + \boldsymbol{\chi}) \tilde{\mathbf{E}}(\omega, \mathbf{r}), \tag{4.23}$$

where $\boldsymbol{\chi}$ is the electric susceptibility given by $\frac{N\langle \boldsymbol{\alpha}(t,\omega)\rangle}{\epsilon_0}$ and $\mu_0 \epsilon_0 = \frac{1}{c^2}$.

In order to simplify Eqn. 4.23 we can write it in the form $(\frac{\partial^2}{\partial \zeta^2} - (\frac{i\omega}{c})^2 (1+\boldsymbol{\chi}))\tilde{\mathbf{E}} = 0$. Using the following mathematical relation as an analogy, $(x^2 + y^2) = (x - iy)(x + iy)$, the equation can be further approximated to

$$(\frac{\partial}{\partial \zeta} \pm i \frac{\omega}{c} \sqrt{(1 + \boldsymbol{\chi})}) \tilde{\mathbf{E}}_\pm = 0. \tag{4.24}$$

Here $\pm$ represents the electric fields of forward and backward propagations. In most cases $|\boldsymbol{\chi}| \ll 1$ so $\sqrt{1 + \boldsymbol{\chi}} \approx 1 + \frac{\boldsymbol{\chi}}{2}$ and we can simplify this equation further and obtain

$$\left(\frac{\partial}{\partial \zeta} \pm i \frac{\omega}{c} (1 + \frac{\boldsymbol{\chi}}{2}) \right) \tilde{\mathbf{E}}_\pm = 0 \tag{4.25}$$

4.4 Vector representation of electric field

The sidebands are generated at a frequency offset from the incoming probe beam in the atomic medium. In order to model the propagation of light for multiple optical frequencies, such as the probe, first-order sidebands, and even higher-order sidebands, we solve Eqn. 4.25, and we expand the electric field as a vector. For an incoming

beam (probe) at a specific frequency (D_2 Line) we want to be able to calculate the amplitude of light that is scattered into other frequency modes. The light scattering process populates the sideband modes with electric field amplitude that is scattered from the probe beam. To do this we write the optical carrier (probe laser beam) and sidebands as a frequency-quantized complex electric field

$$\mathbf{E}(\zeta) = \sum_{\omega} \widetilde{\mathbf{E}}_{\omega}(\zeta)|\omega\rangle e^{-i\omega t} \tag{4.26}$$

and

$$\widetilde{\mathbf{E}}(\zeta) = \sum_{\omega} \widetilde{\mathbf{E}}_{\omega}(\zeta)|\omega\rangle \tag{4.27}$$

where $\widetilde{\mathbf{E}}_{\omega}(\zeta)$ is the position-dependent complex amplitude, ζ is the propagation distance, and $|\omega\rangle$ is a discrete electric field basis labelled with optical frequency ω. It is sufficient, due to symmetry, to only include the positive frequency components of the electric field. To do this we define

$$\widetilde{\mathbf{E}}_{\omega}(\zeta)|_{\omega<0} = 0 \tag{4.28}$$

Also, $|\omega\rangle$ is an orthogonal basis such that $\langle\omega^{'}|\omega\rangle = \delta_{\omega',\omega}$ where ω is the frequency of the incoming light, or carrier beam, and ω' is the frequency that the light is scattered into, which we call as sidebands. Note that $\delta_{\omega'\omega}$ is a Kronecker delta, which is zero when $\omega' \neq \omega$.

By incorporating the vector electric field into Eqn. 4.25 we obtain

$$\left(\frac{\partial}{\partial\zeta} \pm i\frac{\mathbf{W}}{c}\cdot(\mathbf{1}+\frac{\boldsymbol{\chi}}{2})\right)\cdot\widetilde{\mathbf{E}}_{\pm}(\zeta) = 0, \tag{4.29}$$

where $\mathbf{W}$ and $\boldsymbol{\chi}$ are defined in Section 4.5. For forward propagation only, we can rewrite it as

$$\frac{\partial\widetilde{\mathbf{E}}(\zeta)}{\partial\zeta} = -i\mathbf{K}\cdot(\mathbf{1}+\frac{\boldsymbol{\chi}}{2})\cdot\widetilde{\mathbf{E}}(\zeta). \tag{4.30}$$

4.5 Susceptibility and Polarizability Tensor

In Eqn. 4.30, $\mathbf{K}$ and $\boldsymbol{\chi}$ are second-order tensors commonly known as dyadics and $\mathbf{1}$ is the unit dyadic operator. We can write the matrix elements of the dyadics $\mathbf{K}$ and $\boldsymbol{\chi}$ as

$$\mathbf{K}|\omega\rangle = \frac{\omega}{c}\mathbf{1}|\omega\rangle, \tag{4.31}$$

and

$$\langle\omega'|\boldsymbol{\chi}|\omega\rangle = \frac{N}{\epsilon_0}\sum_{\mu\nu}\boldsymbol{\alpha}_{\mu\nu}(\omega)\tilde{\rho}_{\mu\nu}(\zeta)\delta_{(\omega'-\omega),\Omega_{\mu\nu}}e^{i\frac{(\omega'-\omega)}{c}\zeta}. \tag{4.32}$$

where the Kronecker delta and the phase term are added to the definition of χ due to the expansion in the frequency basis. Here, c is the speed of light in vacuum, ω and ω' denote the initial and final frequency states of the optical electric field, N is the alkali-metal atom number density, $\boldsymbol{\alpha}_{\mu\nu}$ (described below) is the polarizability dyadic associated with two ground-state sublevels labeled by μ and ν, $\tilde{\rho}_{\mu\nu}(\zeta)$ is a distance-dependent matrix element in multi-rotating frames of an atomic density-matrix ρ in which $\rho_{\mu\nu} = \tilde{\rho}_{\mu\nu}e^{-i\Omega_{\mu\nu}t}$, $\delta_{(\omega'-\omega),\Omega_{\mu\nu}}$ is the Kronecker delta, and $\Omega_{\mu\nu}$ is the angular frequency of an atomic coherence between the two ground-state sublevels. Thus, for an initial probe frequency ω the sideband light would be scattered into ω', which is offset from ω by the splitting between the two ground states.

We find the polarizability operator to be described by

$$\boldsymbol{\alpha}_{\mu\nu}(\omega) = \frac{1}{\hbar}\sum_{\bar{\mu}}\frac{\mathbf{D}_{\mu\bar{\mu}}\mathbf{D}^{\dagger}_{\bar{\mu}\nu}}{(\omega_{\bar{\mu}\nu}-\omega)-i\gamma_{\mu\nu}}, \tag{4.33}$$

where $\mathbf{D}_{\mu\bar{\mu}}$ is the optical matrix element (Steck, 2003) for electric dipole operator $\mathbf{D}$ defined by ground-state sublevel μ and excited-state sublevel $\bar{\mu}$, $\gamma_{\mu v}$ is the linewidth for a particular transition, and $\hbar$ is the familiar reduced Plank's constant. We can then numerically solve Eqn. 4.30 for the propagation of the sidebands.

4.6 Numerical Model

Armed with the derivation of the propagation equation, we illustrate how we use Eqn. 4.30 to calculate the spatial evolution of the carrier and the optical sidebands as they propagate through the atomic medium. Assuming we have a weak carrier beam incident on a warm vapor cell filled with ^{87}Rb atoms, strong sidebands can be produced if the carrier (probe laser beam) is tuned to an appropriate detuning from the optical resonances. We include only up to the second-order sidebands in the model which means $\widetilde{\mathbf{E}}$ has five frequency components (the first and second order positive and negative sidebands and the carrier frequency). In this example, assuming the carrier light is z-polarized and moving along y, and the magnetic field is along z, we only need to consider the x and z vector components of the electric field since there is no component of the electric field in the direction of propagation. From Eqn. 4.30 we define $\zeta = y$, and write out the components of the dyadics as $\mathbf{K} = K_{xx}\mathbf{xx} + K_{zz}\mathbf{zz}$ and $\boldsymbol{\chi} = \chi_{xx}\mathbf{xx} + \chi_{zx}\mathbf{zx} + \chi_{xz}\mathbf{xz} + \chi_{zz}\mathbf{zz}$, where $\mathbf{xx}, \mathbf{zz}$ and subsequent labels are unit vectors. Using Eqn. 4.31, we write

$$K_{xx} = K_{zz} = \frac{1}{c}\begin{bmatrix} \omega_{-2} & 0 & 0 & 0 & 0 \\ 0 & \omega_{-1} & 0 & 0 & 0 \\ 0 & 0 & \omega_0 & 0 & 0 \\ 0 & 0 & 0 & \omega_1 & 0 \\ 0 & 0 & 0 & 0 & \omega_2 \end{bmatrix} \tag{4.34}$$

where $(\omega_{-2}, \omega_{-1}, \omega_0, \omega_1, \omega_2) = (\omega_0 - 2\Omega_{12}, \omega_0 - \Omega_{12}, \omega_0, \omega_0 + \Omega_{12}, \omega_0 + 2\Omega_{12})$ and we recall that $\Omega_{\mu\nu}$ is the angular frequency of the atomic coherence between two ground-state hyperfine sublevels. In the experiment, the atoms are optically pumped to the end state so we use the two ground-state hyperfine sublevels $|1\rangle = |F = 1, m_F = 1\rangle$ and $|2\rangle = |F = 2, m_F = 2\rangle$ in our model. For cases of imperfect optical pumping, or after population decay (T_1) has occured, including the other hyperfine ground states in the model would be essential to obtaining an accurate representation of the sideband generation process. Now, we use Eqn. 4.32 to write out the xx component

of the susceptibility tensor as

$$\chi_{xx} = \frac{N}{\epsilon_0}\begin{bmatrix} \alpha_{11}(\omega_{-2})\tilde{\rho}_{11} & 0 & 0 & 0 & 0 \\ +\alpha_{22}(\omega_{-2})\tilde{\rho}_{22} & & & & \\ 0 & \alpha_{11}(\omega_{-1})\tilde{\rho}_{11} & 0 & 0 & 0 \\ & +\alpha_{22}(\omega_{-1})\tilde{\rho}_{22} & & & \\ 0 & 0 & \alpha_{11}(\omega_0)\tilde{\rho}_{11} & 0 & 0 \\ & & +\alpha_{22}(\omega_0)\tilde{\rho}_{22} & & \\ 0 & 0 & 0 & \alpha_{11}(\omega_1)\tilde{\rho}_{11} & 0 \\ & & & +\alpha_{22}(\omega_1)\tilde{\rho}_{22} & \\ 0 & 0 & 0 & 0 & \alpha_{11}(\omega_2)\tilde{\rho}_{11} \\ & & & & +\alpha_{22}(\omega_2)\tilde{\rho}_{22} \end{bmatrix} \tag{4.35}$$

and we write out the zx component of the susceptibility tensor as.

$$\chi_{zx} = \frac{N}{\epsilon_0}\begin{bmatrix} 0 & \alpha_{21}(\omega_{-1})\tilde{\rho}_{21}e^{-i\Omega_{12}y} & 0 & 0 & 0 \\ \alpha_{12}(\omega_{-2})\tilde{\rho_{12}}e^{i\Omega_{12}y} & 0 & \alpha_{21}(\omega_0)\tilde{\rho}_{21}e^{-i\Omega_{12}y} & 0 & 0 \\ 0 & \alpha_{12}(\omega_{-1})\tilde{\rho}_{12}e^{i\Omega_{12}y} & 0 & \alpha_{21}(\omega_1)\tilde{\rho}_{21}e^{-i\Omega_{12}y} & 0 \\ 0 & 0 & \alpha_{12}(\omega_0)\tilde{\rho}_{12}e^{i\Omega_{12}y} & 0 & \alpha_{21}(\omega_2)\tilde{\rho}_{21}e^{-i\Omega_{12}y} \\ 0 & 0 & 0 & \alpha_{12}(\omega_1)\tilde{\rho}_{12}e^{i\Omega_{12}y} & 0 \end{bmatrix}. \tag{4.36}$$

In a similar fashion, χ_{xz} and χ_{zz} can be constructed. In order to simplify the notation we let $\alpha_{\mu\mu}(\omega) = \alpha_{xx\mu\mu}(\omega)$ and $\alpha_{\mu\nu}(\omega) = \alpha_{zx\mu\nu}(\omega), \mu \neq \nu$, which can be calculated using Eqn. 4.33. For SI-unit calculations one can use the dipole values and the Clebsch-Gordan Coefficients listed in Ref. Steck (2003) to construct $\mathbf{D}$ and calculate or use Eqn. (6-8) in Ref. Jau to calculate and then convert the unit from cm^3 to $\mathrm{C} \cdot \mathrm{m}^2 \cdot \mathrm{V}^{-1}$. If we remember Section 2.4, where we talk about selection rules in atomic systems. Here, $\alpha_{xx\mu\nu}(\omega)$ is the polarizability dyadic with optical

transitions σ_+ or σ_- only due to selection rules for x polarized light , and $\alpha_{zx\mu\nu}(\omega)$ is the case for a lambda system with π transitions to σ_+ and σ_- transitions. We can now expand the propagation equation (Eqn. 4.30) in matrix form. First we expand the dot product of the dyadics in the propagation equation as

$$\mathbf{K}\cdot(1+\frac{\boldsymbol{\chi}}{2}) = \begin{bmatrix} K_{xx} & 0 & 0 \\ 0 & 0 & 0 \\ 0 & 0 & K_{zz} \end{bmatrix} + \begin{bmatrix} K_{xx}\frac{\chi_{xx}}{2} & 0 & K_{xx}\frac{\chi_{xz}}{2} \\ 0 & 0 & 0 \\ K_{zz}\frac{\chi_{zx}}{2} & 0 & K_{zz}\frac{\chi_{zz}}{2} \end{bmatrix} = \begin{bmatrix} K_{xx}+K_{xx}\frac{\chi_{xx}}{2} & 0 & K_{xx}\frac{\chi_{xz}}{2} \\ 0 & 0 & 0 \\ K_{zz}\frac{\chi_{zx}}{2} & 0 & K_{zz}+K_{zz}\frac{\chi_{zz}}{2} \end{bmatrix}. \tag{4.37}$$

Finally, we can write the propagation equation in matrix form as

$$\begin{bmatrix} \frac{\partial\widetilde{E}_x}{\partial y} \\ \frac{\partial\widetilde{E}_y}{\partial y} \\ \frac{\partial\widetilde{E}_z}{\partial y} \end{bmatrix} = i \begin{bmatrix} K_{xx}+K_{xx}\frac{\chi_{xx}}{2} & 0 & K_{xx}\frac{\chi_{xz}}{2} \\ 0 & 0 & 0 \\ K_{zz}\frac{\chi_{zx}}{2} & 0 & K_{zz}+K_{zz}\frac{\chi_{zz}}{2} \end{bmatrix} \begin{bmatrix} \widetilde{E}_x \\ \widetilde{E}_y \\ \widetilde{E}_z \end{bmatrix}. \tag{4.38}$$

Now, we can solve the propagation equation for light entering the vapor cell (probe) for three spacial directions. Below, we describe how we solve the propagation equation using a numerical model in MATLAB.

4.7 Code Structure

In the following subsections we talk about the basic structure of the code that we developed to solve the propagation equation.

4.7.1 Define constants

First we define the constants such as the speed of light (c), the number density (N), the reduced Planks Constant ($\hbar$), and an estimate of the total linewidth (more in

Section 2.9), which can also be extracted from the fit of the experimental signals.

4.7.2 Transition Frequencies

We write the frequencies of the transitions between all of the levels probed in our experiments. For our model, we use the two hyperfine ground states $|F = 1, m_F = 1\rangle$ and $|F = 2, m_F = 2\rangle$ and the relevant excited state levels for those transitions. Only transitions from the two ground states which satisfy the selection rules $\Delta m_F = 0, \Delta m_F = +1,$ or $\Delta m_F = -1$ are are used in the model. If all of the ground states are included the the rest of the excited states would need to be included as well. We define the frequencies of the optical transitions with respect to the D_2 fine splitting of ^{87}Rb which is $\sim 2\pi(384.230484$ THz). For example, we write the frequency of the transition from $|F = 1, m_F = 1\rangle \rightarrow |F' = 1, m_F = 1\rangle$, where the prime indicates the excited state, as $2\pi(384.230484$ THz $+3.417$ GHz -229.854 MHz). To visualize the frequency splittings, one can refer to Section 2.2. Shifts due to the buffer gas and the Zeeman splitting were also added, but we found the effect on the sideband amplitudes to be negligeable since those shifts are small compared to the fine splitting for our experimental conditions.

4.7.3 Build Polarizabilities

The next step is to build the polarizability dyadic shown in Eqn. 4.33 for all of the transitions and for different polarizations of light. As an example, lets construct the polarizability for the case $\alpha_{\mu\mu} = \alpha_{11}$ and for the z-component so α_{zz11}. Probe light linearly polarized in the z-direction will drive π transitions ($\Delta m_F = 0$) between the ground states and exited states. This polarizability term leads to absorption, not sideband generation since there is not a Λ system. We have two possible transitions from $|F = 1, m_F = 1\rangle$ to the excited states for π transitions and they are $|F = 1, m_F = 1\rangle \rightarrow |F' = 1, m_F = 1\rangle$ and $|F = 1, m_F = 1\rangle \rightarrow |F' = 2, m_F = 1\rangle$. From Steck (2003) we can find the excited state dipole matrix elements for these

transitions and they are $-\sqrt{\frac{1}{8}}$ and $\sqrt{\frac{5}{24}}$. So the polarizability can be written as

$$\boldsymbol{\alpha}_{zz11}(\omega) = \frac{1}{\hbar}S^2\frac{\sqrt{\frac{5}{24}}\sqrt{\frac{5}{24}}}{(\omega_{\bar{\mu}\nu}-\omega)-i\gamma_{\mu\nu}} + \frac{1}{\hbar}S^2\frac{-\sqrt{\frac{1}{8}}\sqrt{-\frac{1}{8}}}{(\omega_{\bar{\mu}\nu}-\omega)-i\gamma_{\mu\nu}} \tag{4.39}$$

where the ω is the incoming laser frequency, S is the transition dipole matrix element used to construct $\mathbf{D}$ in Eqn. 4.33, and $\omega_{\bar{\mu}\nu}$ is the transition frequency described in Section 4.7.2.

Similarly, we can build the polarizability for the case of α_{xz12}. This term leads to sideband generation since it couples both the $|F=1, m_F=1\rangle$ and $|F=2, m_F=2\rangle$ states in a Λ configuration using a σ^+ transition and then a scattered π transition. We can write the polarizability as

$$\boldsymbol{\alpha}_{xz12}(\omega) = \frac{1}{\hbar}S^2\frac{\sqrt{\frac{1}{4}}\sqrt{\frac{1}{6}}}{(\omega_{\bar{\mu}\nu}-\omega)-i\gamma_{\mu\nu}}. \tag{4.40}$$

The rest of the polarizabilities (8 in total) can be calculated in the same manner.

4.7.4 Solve the Propagation Equation

Once the polarizabilities are calculated, we can build the $\boldsymbol{\chi}$ matrices and then solve the propagation equation (Eqn. 4.38) for the scenario that no significant sidebands are generated beyond second-order. With modern computing power, the frequency basis can be easily extended for much higher-order sidebands if needed. We use an 8th-order Runga-Kutta ODE solver (ode87 Integrator[1]) to solve the equation. We start out with an electric field amplitude array for the $\hat{x}$, $\hat{y}$, and $\hat{z}$ directions and for all of the frequency modes involved in the calculation (in our case five frequencies, since we have the first and second-order sidebands and the probe). For example, if the probe is linearly polarized in the $\hat{x}$ direction before entering the vapor cell, we set the amplitude of the probe to 1 for the $\hat{x}$ component of the field, and all of the other

[1]Vasiliy Govorukhin (2022). ode87 Integrator (https://www.mathworks.com/matlabcentral/fileexchange/3616-ode87-integrator)

array elements to zero. Then we evolve Eqn. 4.38 and calculate the the amplitudes of the electric fields after traveling through a vapor cell in the $\hat{y}$ direction. We record 200,000 data points over the length of the vapor cell. As the sidebands are generated, the array elements for the sidebands begins to populate. The optical sidebands are generated in intervals of Ω_{12} as long as the atomic coherence $\tilde{\rho}_{12}$ and its complex conjugate $\tilde{\rho}_{21}$ are nonzero. If the atomic coherence is zero, the probe undergoes standard resonant absorption when near the ground state resonances but no sideband generation occurs. In experimental atomic vapor cells, the atomic density matrix ρ is generally spatially dependent. However, if the optical pumping illumination is uniform across the vapor cell and the microwave radiation is perpendicular to the beam path, it is reasonable to assume ρ to be the same along the entire beam path. If the microwave field has a non-zero projection along the beam path, a spatially dependent phase has to be implemented into ρ. For perfect sideband generation $\tilde{\rho}_{11} = |\tilde{\rho}_{12}| = |\tilde{\rho}_{21}| = \tilde{\rho}_{22} = \frac{1}{2}$ since this means that half of the atomic population is in each ground state sublevel and the coherences are maximized. In general the off-diagonal elements of the density matrix are complex, however, we define the strength of the coherence with a real number.

4.8 Propagation Plots

Fig. 4.1 and Fig. 4.2 show probe (carrier) and sideband propagation through a vapor cell with a length of 0.8 cm. At $y = 0$, just as the light is entering the cell, the carrier beam has a total amplitude of 1. As the light propagates through the atoms, light is scattered into the first-order sideband modes. From the first-order modes the light can be further scattered into higher-order sidebands or back to the carrier. Fig. 4.1(a) shows the x-polarized light as it propagates through the medium. Notice that only the first-order sidebands are scattered into the x-direction since the incoming carrier light is z-polarized. The carrier light is frequency detuned midway between the $F = 1$ and $F = 2$ levels, with both sidebands approximately the same size. When the

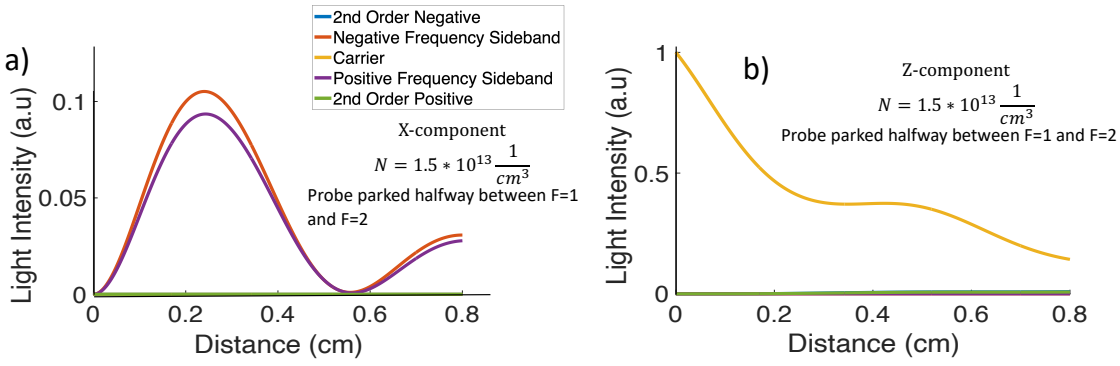

Figure 4.1: Numerical model for the sideband generation process as the light propagates through the atomic vapor cell. (a) We plot the $\hat{x}$-component of the electric field for an incoming probe polarized in the $\hat{z}$ direction. The optical sidebands are scattered into the $\hat{x}$-direction in this case because the first-order sidebands are orthogonally polarized to the incoming probe light. (b) The $\hat{z}$-component of the electric field showing the absorption of the probe light as it propagates. Also of note, second-order sideband light is also generated in the $\hat{z}$ direction (Green and Blue).

probe is frequency detuned towards one of the ground state resonances, the sideband amplitudes get progressively more asymmetric. Fig. 4.1(b) shows the light polarized in the z-direction, which is the carrier and second-order sidebands. This makes sense because the sideband generation process scatters the light into an orthogonal mode, and light scattered from the first-order sidebands will be scattered into a mode that is parallel to the incoming carrier polarization. Fig. 4.2(a) shows all of the sideband amplitude on the same plot. Fig. 4.2(b) is the same as Fig. 4.2(a) but with a higher atom number density. In this case the optical density is larger and the light is absorbed more quickly as it propagates. In this figure it is clear to see that sideband amplitudes do not continuously grow (if the density is high enough), but instead the amplitudes oscillate with propagation distance due to the light being continuously scattered between the frequency modes. In Fig. 4.2(c) the probe is shifted 1.3 GHz towards the $F = 1$ level. This probe detuning is interesting because by the time the light makes it through the cell (0.8 cm), most of the light is actually scattered into one of the second-order sidebands (green). Also notice how the green sideband does not decay over the length of the cell as quickly as the other sidebands due to the fact

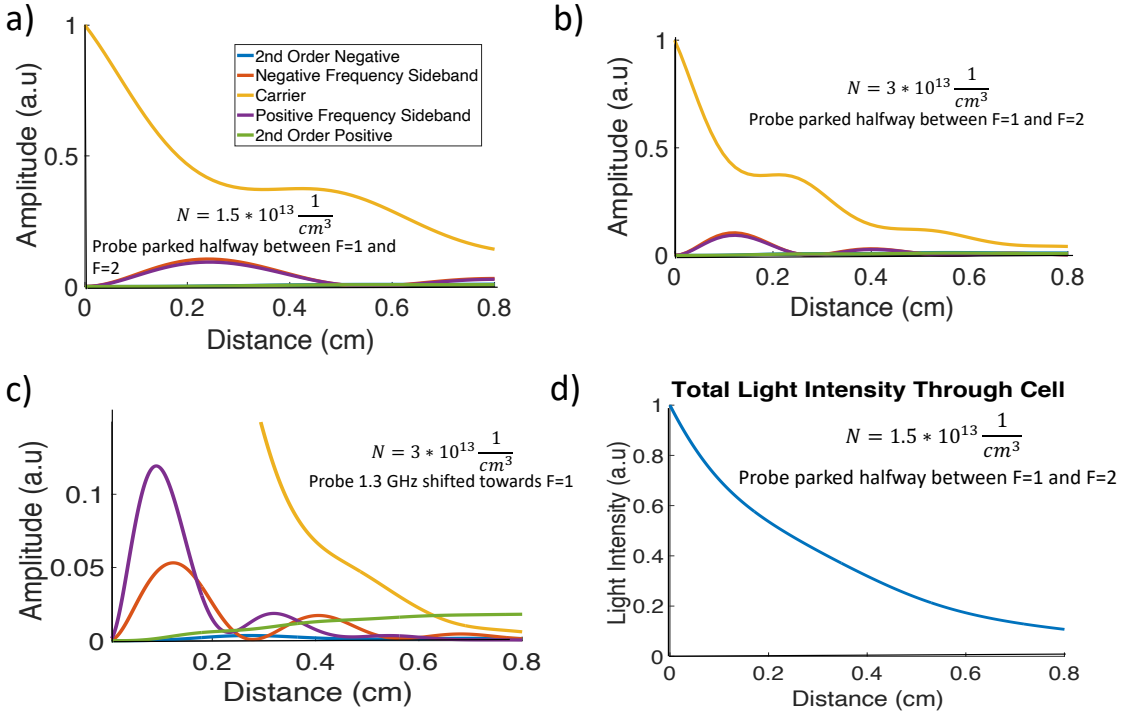

Figure 4.2: (a) Both components of the electric field from Fig. 4.1(a and b) are shown. (b) Similar conditions as the first plot but with a higher number density. One can see the oscillations of the sideband signal with propagation distance indicating back-and-forth scattering between the frequency modes. (c) Zoomed in plot of a particular instance where the second-order sideband is the strongest signal after the length of the vapor cell. (d) Total light intensity through the cell.

that it is farther away from the resonances, and it does not get absorbed as quickly as it propagates. Since much of the light is scattered into the second-order modes, a significant amount of light is likely scattered to even higher-order modes but our model is limited to second-order. Fig. 4.2(d) shows the total light intensity, all of the sidebands and probe light added up, as it passes through the cell. The changes in slope of the plot are due to the fact that scattered light is farther from resonance which alters the absorption of the light as it propagates.

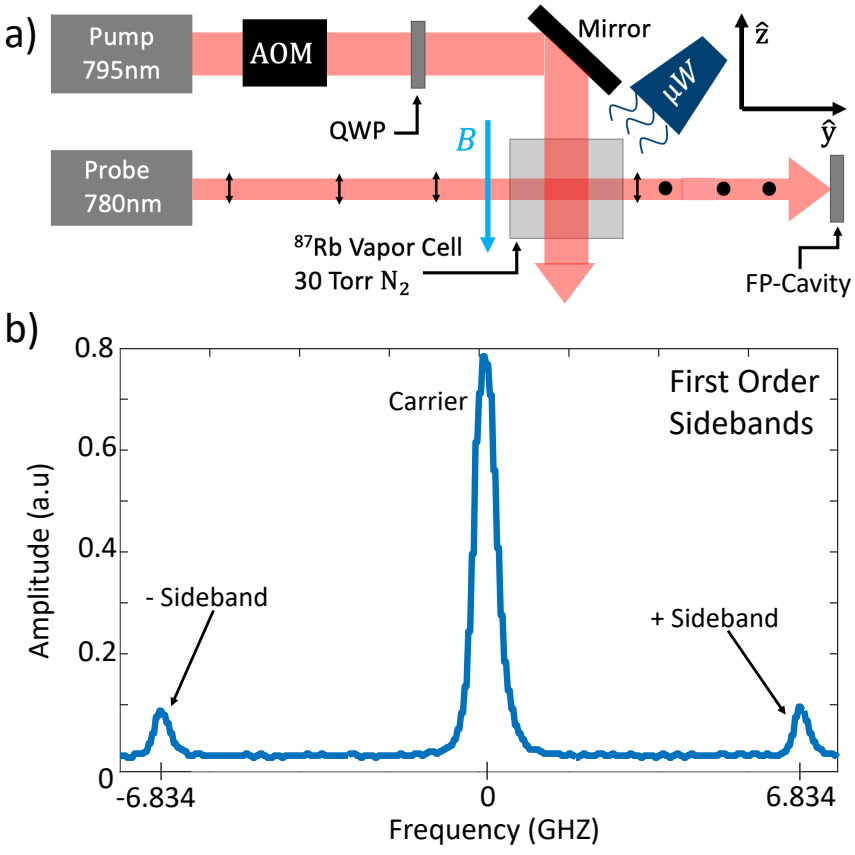

Figure 4.3: (a) Experimental setup we used to test the numerical model. We put a Fabry-Perot cavity after the vapor cell and remove the polarization selector allowing for the measurement of both the sideband and probe polarizations (b) Signal generated from the Fabry-Perot showing the positive and negative sidebands generated offset from the carrier by the hyperfine splitting.

4.9 Testing the model

Now that we have a working numerical model to calculate sideband propagation through an atomic medium, we test it using our tabletop sideband generation setup. Using the setup shown in Fig. 4.3(a), we send the generated sideband light to a scanning Fabry-Perot etalon. Also, the polarization analyzer is removed because we wanted to look at all light polarizations, otherwise either the sidebands or probe would be extinguished by the polarization selection. Aside from these changes, the experiments performed are very similar to the pulsed operation experiments described in Chapter 3. By sending current to a piezo, we scan across the frequency of the

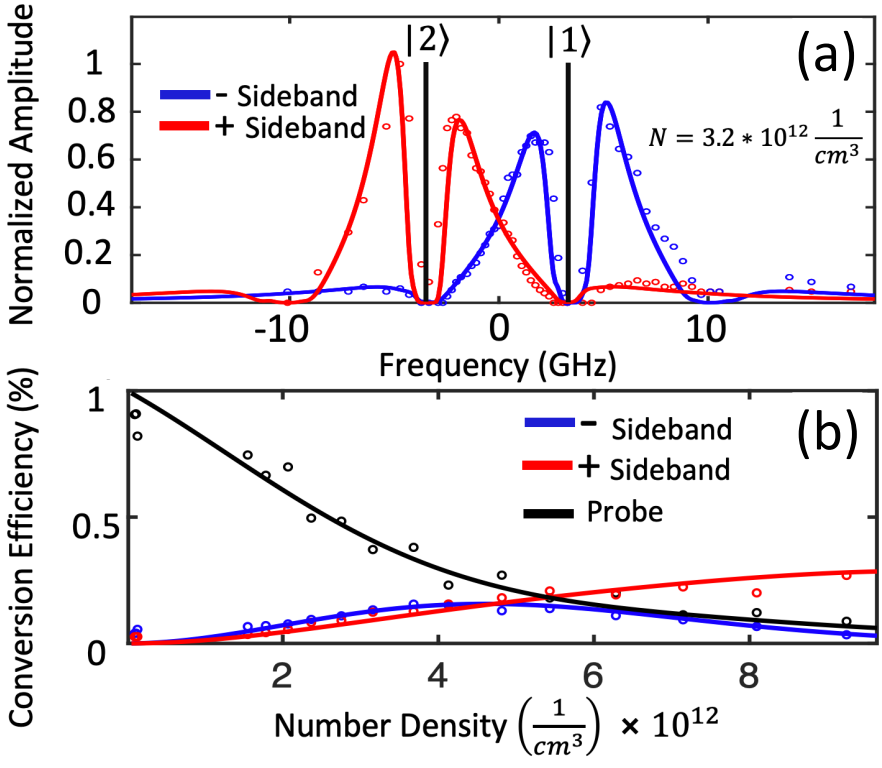

Figure 4.4: (a) Plot of the first-order sideband amplitudes as we scan across the ground state resonances. The zero frequency position is defined as the middle of the $|F = 1\rangle$ and $|F = 2\rangle$ manifolds. The open circles are experimental data, and the solid lines are from the numerical model, which is qualitatively fit to the experimental data from the Fabry-Perot etalon for 30 Torr of N_2 buffer gas. The data shows good agreement with the theoretical model. (b) The sidebands conversion efficiency with respect to number density.

Fabry-Perot cavity allowing us to see the sideband and carrier beams on the same scan. Fig. 4.3(b) shows data taken of the positive and negative frequency sidebands to either side of the incoming carrier light. To test the theoretical model, we record the sideband and carrier amplitudes after exciting the cell. We cannot measure the amplitude of the sideband halfway through the cell, but increasing the optical depth by raising the temperature produces approximately the same effect since the light travels through just as many atoms in the hot shorter cell as it does in the longer cell. In Fig. 4.4(a), we experimentally scan the frequency of the probe across the $|1\rangle$ and $|2\rangle$ resonances, measuring the amplitude of the sidebands, and results from our numerical model are plotted with the experimental data. In the model, we calculate

the propagation of the sideband through the medium at the number density $3.2 * 10^{12}$ cm^{-3} and determine the sideband amplitudes at the exit of the cell. The amplitude of the sideband and probe light is severely reduced on resonance due to absorption by the atoms. Also of note, if the probe frequency is set outside of either resonance by the hyperfine splitting, one of the sidebands is again absorbed. For example, when the probe is tuned to about -10.2 GHz (-6.8 GHz detuned from the $|2\rangle$ resonance), the positive frequency sideband (red) is absorbed because it is generated at the frequency of the resonance. The negative frequency sideband (blue) is not absorbed because its frequency is far from resonance. However, its amplitude is reduced because the polarizability is inversely proportional to the optical detuning, as shown in Eqn. 4.33. In Fig. 4.4(b) we measure the sideband conversion efficiency versus number density. Just as the sideband amplitudes oscillate with respect to distance in Fig. 4.2(b), the sideband amplitudes also oscillate with respect to an increase in number density. The conversion efficiency is equal to P_s/P_c, where P_c is the power of the probe before it enters the vapor cell, and P_s is the power of a particular sideband after leaving the cell. We set the probe frequency to be about halfway between the $|1\rangle$ and $|2\rangle$ resonances. The data and simulation of Fig. 3b indicate that the two sidebands should be the same amplitude for this probe detuning. However, the optical pumping was not 100% efficient in the experiment, and all the population was not initially in the $|2, 2\rangle$ state. We found that to model this situation we could simply implement an imperfect $\pi/2$ pulse, which means the atoms are not in an exactly equal superposition of the hyperfine ground states. This leaves more atomic population in one of the ground states after the microwave pulse than the other. Also, the model predicts the probe frequency was shifted 300 MHz towards $|1\rangle$ indicating we were not exactly between the two resonances. With about 60% of the atomic population remaining in the $|2, 2\rangle$ state after the microwave pulse, the model shows good agreement with the data. With an imbalance in population, one sideband is absorbed more quickly than the other as it propagates through the cell, and the model clearly predicts this behavior.

Chapter 5

Atomic Gradiometer Based on the Interference of Optical Sidebands

In Chapters 3 and 4 we describe the sideband generation process in detail. In this chapter, we describe how the interference of sidebands (beat-note) in two spatially separated vapor cells can be used to build a magnetic gradiometer with excellent sensitivity. First we describe the tabletop experimental setup we built, generate a beat-note signal, and then measure the noise floor in the laboratory setting at the Sandia National Laboratory.

Later, we also discuss a miniaturized "physics package" gradiometer which is used to record the noise floor. Some of the figures and passages in this chapter have been adapted from Campbell et al. (2022).

Then, with the help of collaborators, we build a miniaturized "physics package" gradiometer and record the noise floor of 25 fT/cm $\sqrt{Hz}$ in an unshielded room without magnetic shielding. Some of the figures and passages in this chapter have been adapted from Campbell et al. (2022).

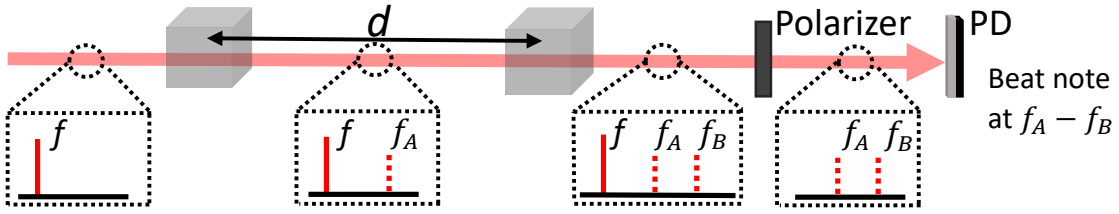

Figure 5.1: A conceptual overview of the gradiometer. Two alkali vapor cells are separated by a distance, d. A linear probe (carrier) beam with frequency, f, passes through the two vapor cells. The probe beam's interaction with the atoms in Cell A produces an orthogonally polarized optical sideband at magnetic-field-dependent frequency f_A. Similarly, interaction with Cell B produces a second optical sideband, at frequency f_B. The probe beam is removed using a polarizer, leaving behind only the two optical sidebands. The sidebands are captured by a photodetector where they interfere to produce a beat-note at frequency $f_A - f_B$ that is directly proportional to the magnetic gradient field between the two vapor cells.

5.1 Conceptual Idea

First, we provide a conceptual overview of the operation of the gradiometer and then dig into the details of its operation. As shown in Fig 5.1 a laser beam that we refer to as the "probe" is incident on two Alkali atomic vapor cells separated by a distance d. The atoms in Cell A are prepared in such a way that the probe beam's interaction with the atoms produces an orthogonally polarized optical sideband at magnetic-field-dependent frequency f_A. The sideband process is explained in more detail in Chapters 3 and 4. Similarly, interaction with Cell B produces a second (also orthogonally polarized to the probe) optical sideband, at frequency f_B. After traveling through both vapor cells the probe beam is incident to a polarizer. The polarizer effectively separates the sidebands from the probe due to their orthogonality. The sidebands form a beat-note at the frequency $f_A - f_B$ that is directly proportional to the magnetic field gradient between the two vapor cells. By measuring the frequency of the beat one can easily obtain the magnetic gradient field between the two vapor cells.

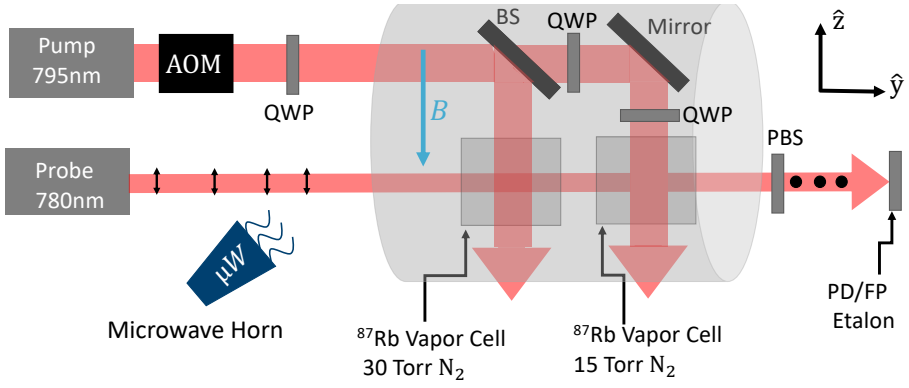

Figure 5.2: An experimental diagram of the tabletop experiment for the beat-note experiment. The setup is very similar to the setup described in Section 3.4 but with the addition of another vapor cell filled with 15 Torr of N_2 buffer gas and a 50-50 BS which sends half the pump light to the additional cell.

5.2 Tabletop Gradiometer

The experimental configuration is similar to the setup described in Section 3.4, except we include another vapor cell filled with 15 Torr of N_2 as shown in Fig. 5.2. The probe beam goes through both vapor cells before exiting the mu-metal shielding. Fig. 5.3 is a more detailed image of the experimental setup inside the shield. We 3D printed a housing for the two vapor cells to sit in. The 15 Torr cell was removed to show the housing that the cell sits in. The cells are angled by a few degrees with respect to the probe axis to suppress effects from reflections of the cell surface with the probe light (Pedrotti et al., 2017). The vapor cells are surrounded by insulation to retain heat and a twisted pair of phospher-bronze heater wire. Kapton tape is used to hold the wire and insulation in place, and then a 3D-printed lid (not shown) is screwed over top the two cells. All screws in the setup are plastic as metal could destroy the signal by introducing unwanted field gradients and thermal Johnson noise (Perepelitsa, 2006). A type E thermocouple is brought to each vapor cell and then taped (Kapton) to the top of the vapor cell some distance away from the heater wire. The pump beam enters the shield, as shown in Fig. 5.2 and the beam is incident on a $50-50$ non-polarizing BS, which causes half the light to go to the 30 Torr cell and half goes to the 15 Torr cell after reflecting off a mirror. The light that

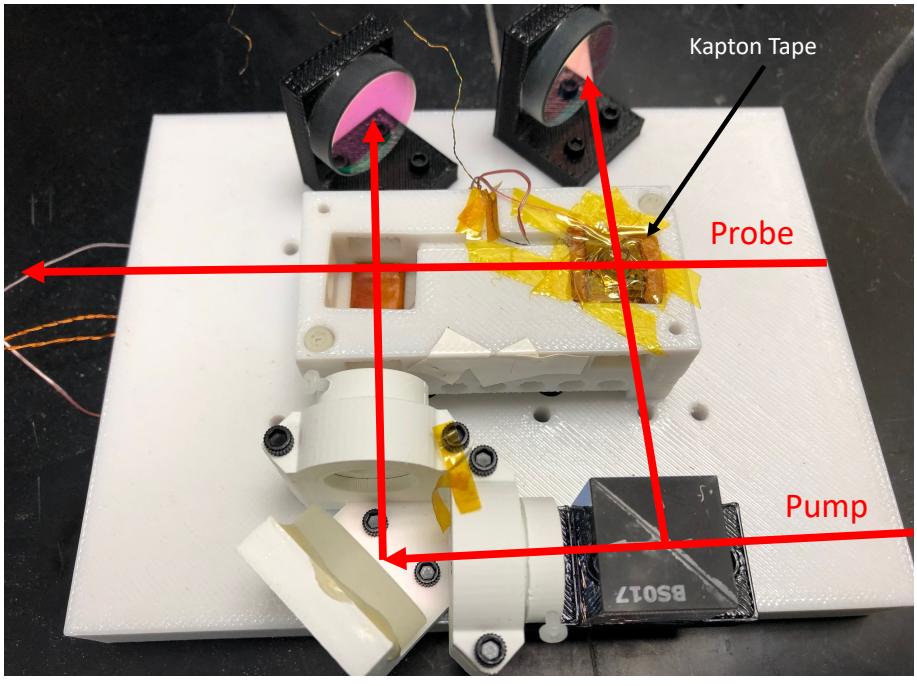

Figure 5.3: The experimental setup inside the shield. The 30 Torr vapor cell is shown inside the 3-D printed mount surrounded by insulation and wrapped with twisted pair heater wire. Kapton tape is used to hold the wire and insulation in place. The pump beam is split by a 50-50 BS such that half the light is directed to a 15 Torr vapor cell (not shown). Two QWPs are used to compensate for polarization distortion effects from the mirror and BS.

is transmitted through the BS passes through two QWPs which compensate for polarization distortion from the beam reflecting off the mirror and/or PBS. Once the pump beam goes through the cells, the light is usually ignored since we read our signals from the probe light. However, we put in two mirrors after the cells to reflect the pump light outside the shield in case we wanted to make a measurement of the pump light, such as when we perform beam alignment and/or make a measurement of the optical pumping.

We conduct the experiment in the same way as described before, by pulsing the pump and applying a $\pi/2$ pulse with a microwave horn to put the atoms in a coherent superposition of ground states. However, after the addition of the 15 Torr cell, interference between the sideband light from the two vapor cells generates a beat-note directly proportional (to first-order) to the gradient field between the two cells. Even

in the absence of a significant gradient field, a beat-note is still observed due to the nominal 15 Torr differential in nitrogen buffer gas pressure between the two cells. This allows the gradiometer to be effectively operated in a zero-field environment because a beat-note is still produced even when there is no field. The nitrogen buffer gas induced pressure shift for the ground state hyperfine transitions, $\Delta\nu_{BG}$, is approximately 548 Hz/Torr Vanier et al. (1982a) which translates to an 8220 Hz shift for 15 Torr of buffer gas difference. However, experimentally we measured buffer gas shifts of $\sim 6-7$ kHz between the two vapor cells at zero-field. The discrepancy likely arises from an inaccurate understanding of the buffer gas pressures in each vapor cell. The company that filled the vapor cells likely did not achieve a pressure in the cells at exactly the specified pressure, which means the buffer gas differential may not be 15 Torr between the two cells. Also of note, it is possible that a field gradient can be applied which causes a beat-note of zero-frequency. If this problem arises in practical application, a small bias field can be applied to cause a beat-note, or the sensor could be simply be rotated 180 degrees.

In a magnetic field gradient applied along the pump direction (z-direction), the two vapor cells will experience a different magnetic magnetic field. The frequency difference between the sideband and the probe, Δv, in low magnetic field is given by,

$$\Delta\nu = \Delta\nu_{HFS} + \nu_{BG} + 3\gamma \mid \mathbf{B_z} \mid \tag{5.1}$$

where $\Delta\nu_{HFS}$ is the separation between the two hyperfine ground states $|F=1\rangle$ and $|F=2\rangle$, ν_{BG} is the buffer gas induced pressure shift between the ground states, γ is the gyromagnetic ratio ($2\pi \times 6.99\ \frac{\mathrm{Hz}}{\mathrm{nT}}$), and $\mid \mathbf{B_z} \mid$ is the absolute background magnetic field experienced by the vapor cell. The dependence of $\Delta\nu$, on the magnetic field is amplified by a factor of three by probing the $|F=1, m_F=1\rangle \leftrightarrow |F=2, m_F=2\rangle$ hyperfine ground states. Eqn. 5.1 is only true for low B-field because the splitting between the states becomes nonlinear for higher magnetic fields. This effect is explained in more detail in Section 2.3.

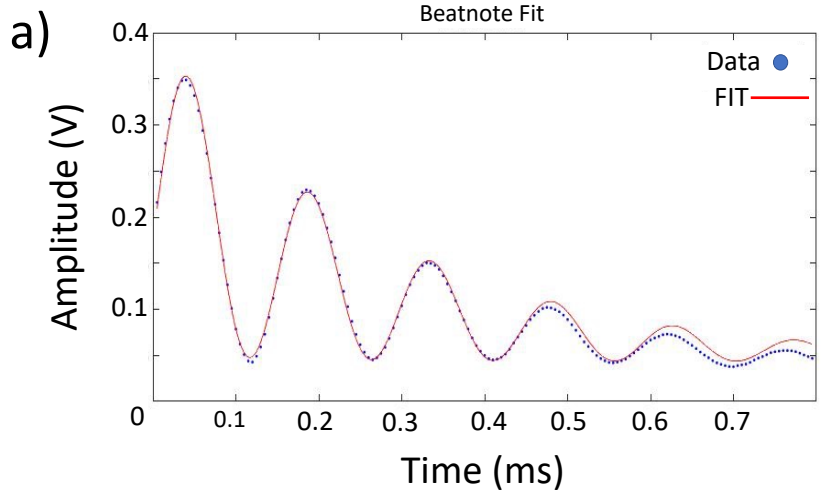

Figure 5.4: Beat-note generated from the interference of sidebands from the tabletop gradiometer experiment. The beat-note signal is fit to Eqn. 5.2 and the frequency of the beat is extracted in order to measure the magnetic gradient and also a noise floor.

5.3 Beat-note Signal

The beat-note is produced by an interference of the electric fields from two exponentially decaying coherent light sources (two sidebands). The functional form of the photodiode output after the $\pi/2$ pulse is given by

$$S(t) = E_A^2 e^{-\frac{2t}{T_A}} + E_B^2 e^{-\frac{2t}{T_B}} + 2E_A E_B e^{-t(\frac{1}{T_A}+\frac{1}{T_B})} \sin(2\pi f t + \phi) \quad (5.2)$$

where E_A and E_B are the electric fields produced by the sidebands from cells **A** and **B** respectively, T_A and T_B are the hyperfine ground state relaxation rates in the two cells, and $f = \Delta\nu_{BG} + 3\gamma|\Delta\mathbf{B}|$ is the relative frequency difference between the two sidebands (beat-note frequency). Considering $\Delta\nu_{BG}$ to be a constant offset, the magnitude of the magnetic field gradient between the two cells is obtained from a measurement of f.

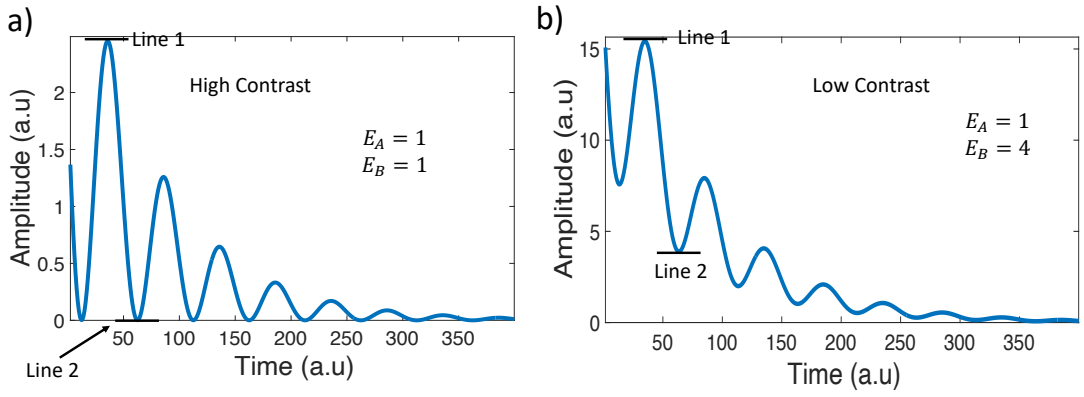

Figure 5.5: (a) Simulated beat-note signal based on Eqn. 5.2 with high contrast. $T_A = T_B$ and $E_A = E_B$. (b) Simulated beat-note signal with low contrast. $T_A = T_B$ and are the same and $E_A = 1, E_B = 4$

5.4 Signal Contrast

In Section 3.14 we talk about the important properties of sidebands, such as the signal amplitude and T_2 time, that we want to optimize for gradiometry experiments. We also introduce the FOM to quantify the importance of those two parameters. However, the beat-note signal has another quantity which we want to maximize, the signal contrast. The signal contrast is a measurement of how "well" the signals beat together. The more perfect the beating, the more information that can be extracted from the signal, and hence the better the sensitivity. We describe contrast more precisely in Fig. 5.5, where we show simulated beat-note signals based on Eqn. 5.2 for the case of a high contrast signal and a low contrast signal. The high amplitude portion of the beat-note signal is shown as line 1 and the low amplitude dip is shown as line 2. For perfect contrast, the dip should come back down to zero from the high point of line 1 indicating perfect interference. For the low contrast signal, line 2 does not come back to zero indicating that the interference between the sidebands was not perfect. For high contrast to occur the T_2 times and the amplitudes of the sidebands generated in both the 30 Torr and 15 Torr cell need to be similar. If they are not, the contrast suffers. In the low contrast signal in Fig. 5.5(b) the amplitude of E_b was four times the amplitude of E_a leading to the reduction in contrast. In our experimental

setup, if the sideband amplitudes between the vapor cells were very different we noticed a sharp reduction in the contrast of the resulting beat-note. This means that an optimization of the microwave horn positioning and cell temperature was needed to get the best signals. We found that heating the 30 Torr cell to 120^o C and the 15 Torr cell to 135^o C produced the best results because the 30 Torr cell generates larger amplitude sidebands than the 15 Torr cell, so the temperatures needed to be different to compensate.

5.5 $\pi/2$ Pulse in the Two Cells

As we discussed in the last section, it is important for the sidebands to be similar in amplitude in each cell in order to achieve good contrast. This means that when a microwave pulse is applied to the cells, it is essential that both cells see a $\pi/2$ pulse. Small changes in microwave polarization strongly effect the amplitude and contrast of the beat. Since the microwave field is coming from a single source (microwave horn), field parameters need to be found which produce the correct pulse in each vapor cell (or a compromise which fits both cells the best). We can approximate the best parameters by calculating the probability for the atoms to be in the excited state (in our case the $|F = 2, m_F = 2\rangle$ state) in a two level system. We can use the Rabi frequencies (described in Section 2.10) of the atoms and the microwave detuning to determine the best parameters for both of the vapor cells. The total Rabi frequency is given by

$$\begin{aligned} \Omega_{tot15} &= \sqrt{\Omega_{15}^2 + \Delta_{15}^2} \\ \Omega_{tot30} &= \sqrt{\Omega_{30}^2 + \Delta_{30}^2} \end{aligned} \tag{5.3}$$

where Ω_{15} is the Rabi frequency of the 15 Torr cell and Ω_{30} is the Rabi frequency of the 30 Torr cell. Now, in the equation below, we calculate the probability of being in

the $|F = 2, m_F = 2\rangle$ state for both cells.

$$P_{15} = (\frac{\Omega_{15}^2}{\Omega_{tot15}^2})\cos(\frac{\Omega_{tot15}t}{2})$$
$$P_{30} = (\frac{\Omega_{30}^2}{\Omega_{tot30}^2})\cos(\frac{\Omega_{tot30}t}{2}) \quad (5.4)$$

In Fig. 5.6 we show a simulation of Eqn. 5.4 as the microwave frequency is swept across the resonances of the two vapor cells. In the simulation, the microwave magnetic field strength is 2 milligauss for the 15 Torr cell and 4 milligauss for the 30 Torr cell, and the microwave resonance frequency for the 30 Torr cell is $2\pi * 6834697000$ Hz and $2\pi * 6834689000$ Hz for the 15 Torr cell. The microwave resonant frequency is different for each vapor cell because of the buffer gas induced hyperfine frequency shift. The goal is to find a position where the two cells are both in an equal superposition of the two ground state levels (i.e. the state vector on the equator of the Bloch sphere). In the "zoomed in" portion of Fig. 5.6 we show an example of a point where a $\pi/2$ pulse is applied to both cells. We know this because the probability of being in the $|F = 2, m_F = 2\rangle$ state is 1/2, which means the probability amplitude for being in the two states is equal. These simulations helped us in finding the appropriate microwave field amplitudes and frequencies to generated the desired pulse in each cell. However, once strong beat-note signals were generated, fine tuning of the parameters could be done by visually optimizing the signal.

5.6 Doublepass Configuration

In the doublepass configuration, the PD is removed and the beam is reflected off a mirror and sent back through the vapor cell as shown in Fig. 5.7. We were able to achieve better signal amplitudes in the doublepass configuration by increasing the path length through the vapor (it goes through it twice). It is also possible to double the amount of atoms in the vapor cell by increasing the temperature (number density) of the atoms; however, this negatively impacts the T_2 time which makes this method less attractive. The distances between the cells in the doublepass configuration and the

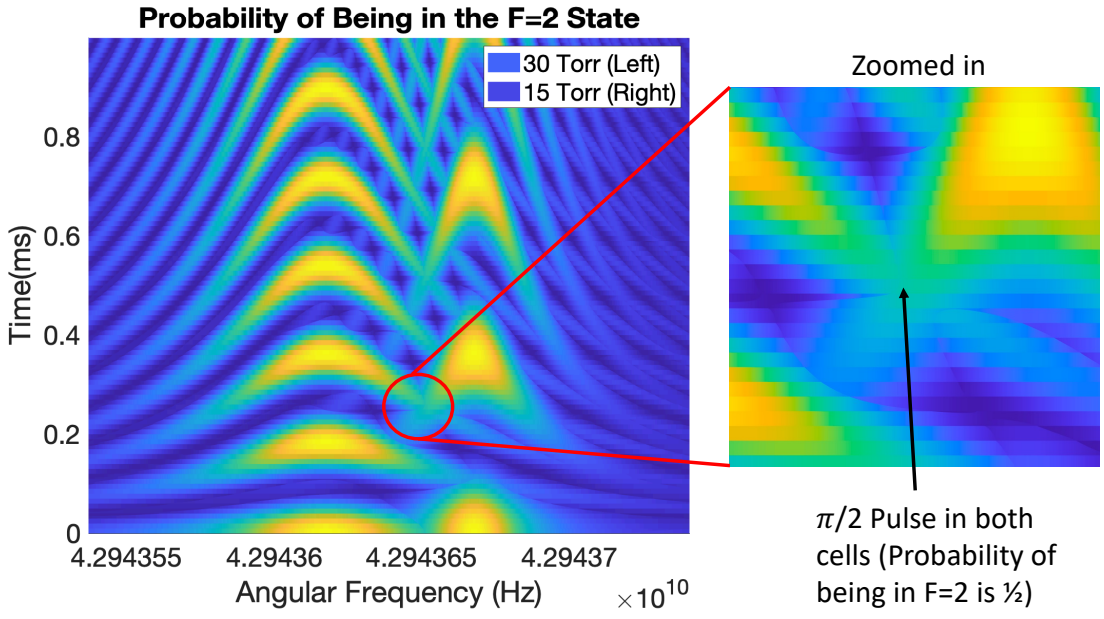

Figure 5.6: A simulated plot of the probability the atoms are in the $F = 2$ state with respect to microwave frequency. This is required to achieve a $\pi/2$ pulse for both the 15 Torr and 30 Torr vapor cells. A $\pi/2$ pulse is achieved when the probability fo being in the $F = 2$ state is 1/2. The microwave resonance frequency for the 30 Torr cell is $2\pi * 6834697000$ Hz and $2\pi * 6834689000$ Hz for the 15 Torr cell

back reflecting mirror were carefully chosen to ensure constructive interference of the relative phase between the probe and sidebands for forward and backward propagating probe light. Maximum sideband generation occurs at half-integer spacings of the wavelength of the microwave radiation. The hyperfine frequency of ^{87}Rb is 6.8 GHz which translates to a wavelength of 4.4 cm. This discrete spacing relative to the mirror gives a 2.2-cm spacing between the mirror and Cell **A** and 6.6-cm spacing for the mirror to Cell **B**, making the cell-to-cell separation (gradiometer baseline) 4.4 cm. After passing through the cells, the retroreflected light again passes through the **PBS** which directs the orthogonally polarized sideband light towards the **PD**.

Fig. 5.8 shows a comparison between the beat-note generated from the doublepass and singlepass experiments. The experimental parameters for each configuration were optimized to obtain the largest largest amplitude signals. In the doublepass configuration we increased the optical power of the probe from 12 μW in the singlepass

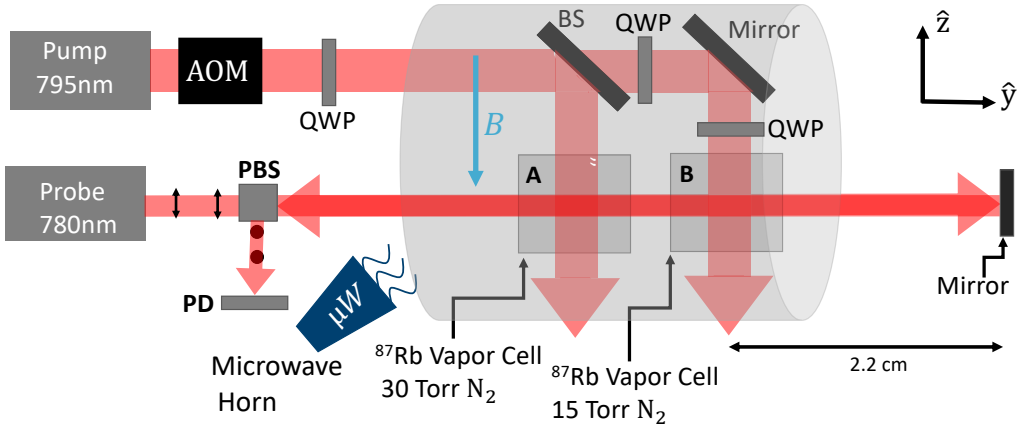

Figure 5.7: Experimental Setup for the doublepass configuration. The PD in Fig. 5.2 is replaced with a Mirror spaced 2.2 cm away from cell B. The light is reflected back through the cell and a PBS is used to direct the back-reflected light towards a PD

configuration to 20 μW. The probe light travels twice as far through the cell in the doublepass configuration so a larger initial probe power is advantageous because the light is interacting with a larger cross section of atoms. As shown in Fig. 5.8 the optimized amplitude of the beat-note generated from the doublepass setup is about 30% larger than the best signal obtained from singlepass measurements.

5.7 Sandia Noise Measurements

Using the tabletop setup described in Section 5.2 we took some preliminary noise measurements at Sandia to see if the sideband generation technique for gradiometry was worthy of further study. For each pulse cycle we extracted the frequency of the beat-note signal by fitting it to Eqn. 5.2. The frequency of the beat-note includes the bias frequency shift from the buffer gas difference in each cell. To obtain the absolute gradient, the sensor would need to be calibrated by measuring the buffer gas shift precisely. However we did not make this measurement. From the measurement of the beat-note frequency a time series of the gradient field was obtained. Fig. 5.9(a) shows the frequency time series data for 5 total seconds of data. Each data point is

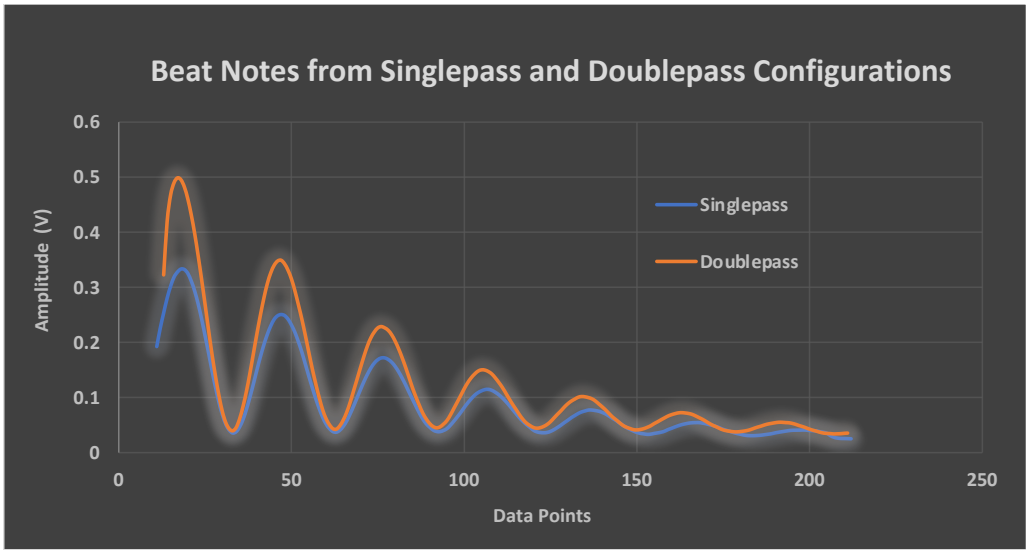

Figure 5.8: The best beat-note signals obtained from the singlepass experiment (blue) vs. the doublepass (orange) experiment. The beat-note amplitude was about 30% larger for doublepass.

a measurement of the frequency of the beat-note, which was ~ 6.8 kHz when these measurements were made. From the Fourier transform of the gradient field time series, the gradiometer noise floor was calculated in units of $\frac{pT}{\sqrt{Hz}\ cm}$ as shown in Fig. 5.9(b). Also included in this figure are estimations of noise levels from the probe laser (the pump is turned off during pulse) and electronic noise in the signal path, as well as a calculation of the photon shot noise.

The probe and electronic noise is calculated from the following equation:

$$\text{Sensitivity} = \frac{N_s}{\alpha\pi S\tau\gamma d\sqrt{T_d}}, \tag{5.5}$$

where N_s is noise with units of $\frac{V}{\sqrt{Hz}}$, α is a correction factor, S is the signal amplitude, τ is the measurement time, γ is the gyromagnetic ratio ($\frac{21Hz}{nT}$), d is the gradiometer baseline (4.4 cm), and T_d is the duty cycle (0.5). the photon shot noise is a Poisson process (Perepelitsa, 2006). We define the root mean square current fluctuations as

$$\text{PSN} = \sqrt{2Ie} \tag{5.6}$$

where I is the DC current (A), and e the charge of an electron in Coulombs (A $\times$ s). To find N_s from PSN we multiply by the gain of the PD which is in units of

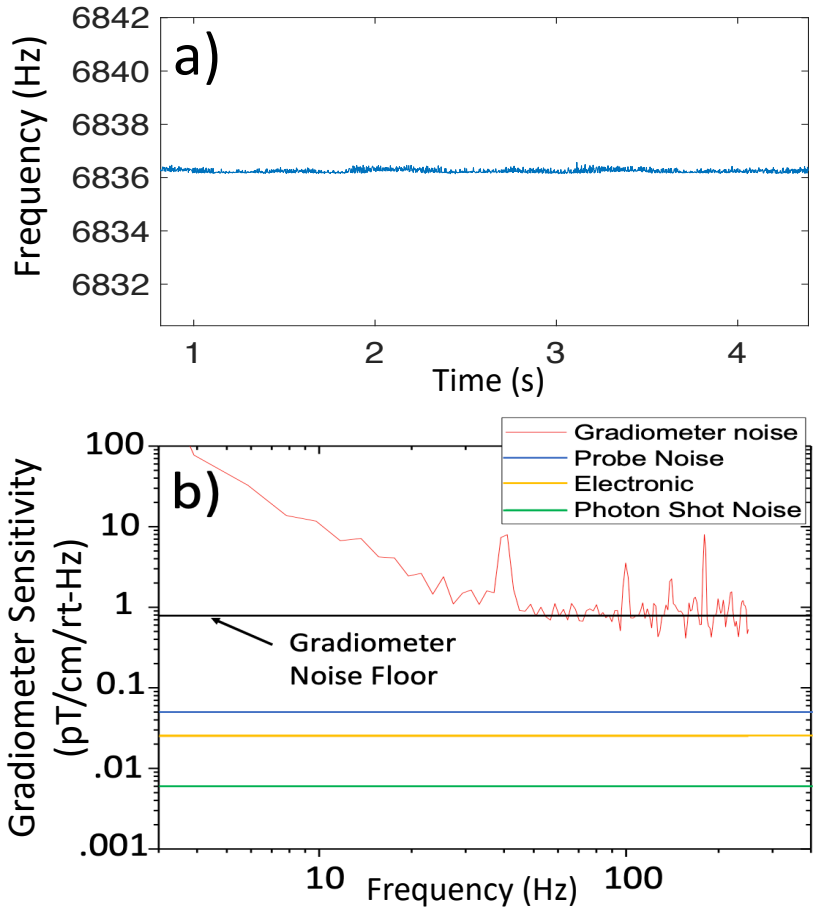

Figure 5.9: (a) Beat-note frequency vs. time. Each data point is a measurement of the frequency during during a probing cycle ($\sim$ 1 ms) (b) Noise floor measurements for the tabletop gradiometer. The noise floor is around 1 pT/cm/$\sqrt{Hz}$. Also included are measurements of the Probe noise, electronic noise, and an estimate of the photon shot noise.

V/A. As shown in Fig. 5.7(b) our noise floor is approximately $1\frac{pT}{\sqrt{Hz}\ cm}$ with a 4.4 cm baseline. While this is a good sensitivity for an atomic gradiometer, especially one based on a completely new concept such as this one, the goals of this project were much more ambitious. We hoped to achieve noise floor sensitivities near $1\frac{fT}{\sqrt{Hz}\ cm}$ which would be near state-of-the-art for these systems (Limes et al., 2020). However, the sensitivity we measured in the noisy laboratory environment with a tabletop setup were encouraging enough that we constructed a miniaturized version of the sensor which we call the "physics package."

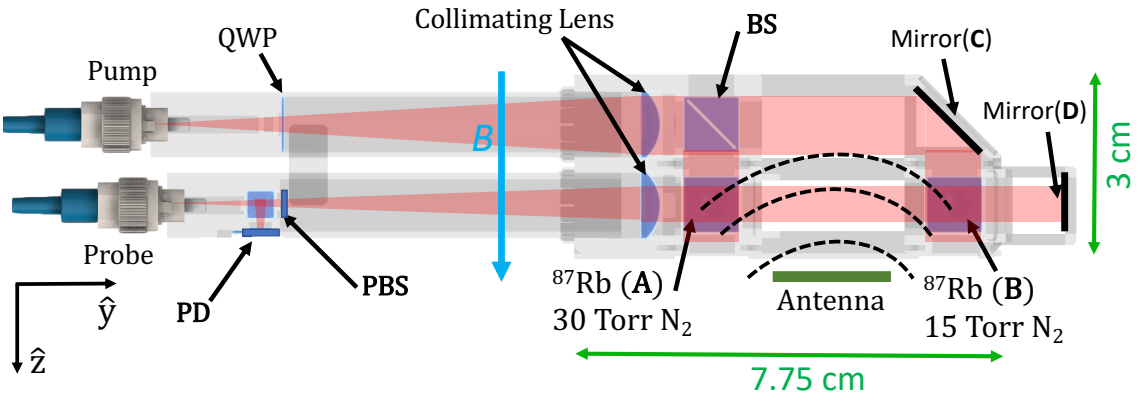

Figure 5.10: A schematic of the compact gradiometer sensor head. The probe makes two passes through vapor cells filled with ^{87} Rb vapor and nitrogen buffer gas. The sidebands are separated from the probe by the **PBS** and measured on a **PD**.

5.8 Physics Package Gradiometer

This miniaturized version of the sensor was developed by researchers at QuSpin (Vishal Shah and Ying-Ju Wang) in parallel to the tabletop experiments performed at Sandia labs. The physics package of the sensor is shown in Fig. 5.9. The sensor body of the physics package is made of 3D printed material and its dimensions are approximately 7.75 cm long, 3 cm wide, and 1.35 cm deep (without counting the beam expansion optics) with the distance between the two cells 4.4 cm (measured from the middle of each vapor cell). The sensor is run in pulsed mode with a 3 ms cycle time. During the first phase of the cycle (1.5 ms long) the pump light is switched-on to spin polarize the atoms in both vapor cells. The pump laser wavelength is modulated at 200 kHz to clear both the $5^2S_{1/2}|1\rangle$ and $|2\rangle$ ground state manifolds and transfer a majority of the atoms into the $|2,2\rangle$ dark state. Due to limitations in the available pump optical power in the experiment (4 mW at the entrance of the sensor head), we estimate that roughly 60% of the atoms were optically pumped into the $|2,2\rangle$ dark state in the two cells. After the optical pumping phase, the pump light is switched-off and a $\pi/2$ pulse is applied using custom microstrip patch antenna to generate sidebands. This sensor is based on the doublepass configuration so the light

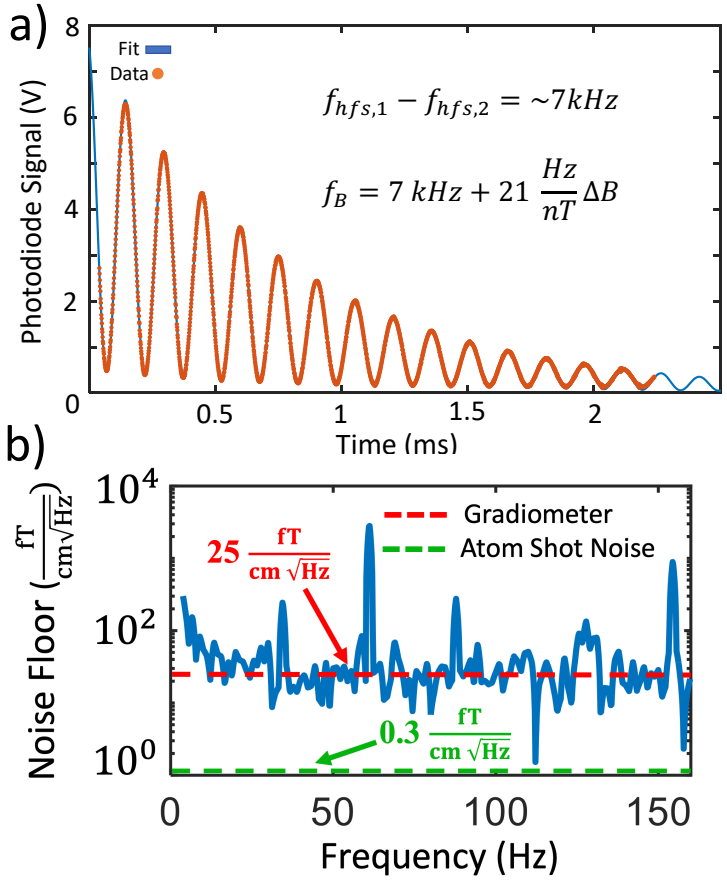

Figure 5.11: (a) The beat-note measured from the physics package gradiometer at QuSpin. The Signal is fit to Eqn. 5.2. (b) The Noise floor extracted from the beat-note shown in the first plot of this figure, as well as an estimate of the atom shot noise limit.

reflects off a mirror and is sent back through the cell. The sideband light is separated from the probe light by the PBS allowing sideband light to pass to the photodetector (PD) isolated from the probe.

For the noise measurements, the sensor was not enclosed in mu-metal shielding, meaning the atoms were exposed to any background field present in the laboratory, including the Earth's magnetic field ($\sim 50\ \mu T$). The raw photodiode output was digitized and recorded using a 16-bit, 2 MSPS analog-to-digital converter (ADC). In post processing, the beat-note obtained in each cycle was fitted to the functional form $S(t)$ shown in Eqn. 5.2 to extract the beat-note frequency. Fig. 5.10(a) shows

the beat-note signal obtained from the gradiometer physics package as well as a fit of the signal. The fitted function closely overlaps with the experimental data and the signal is relatively high contrast. After making a measurement of the beat-note frequency in each 3 ms cycle, a time series of the gradient field was obtained just as in Fig. 5.7(b). From the Fourier transform of the gradient field time series, the gradiometer noise floor in the ambient laboratory background environment, shown in Fig. 5.10(b), was measured to be 25 fT/cm/$\sqrt{Hz}$. An estimate of the atom shot noise (0.3 fT/cm/$\sqrt{Hz}$) from Eqn. 1, RefAllred et al. (2002) is also shown. We expect the sensitivity to approach the atom shot noise limit by increasing the pump power to obtain unity spin polarization, improving the optics, and mitigating the technical noise. The noise floor measured by the physics package is nearing the state of the art sensitivity (Limes et al., 2020) recorded in more conventional gradiometers .

Chapter 6

Towards a Dead-Zone-Free gradiometer

6.1 Introduction

OPM setups usually measure the magnitude of the magnetic field irrespective of the direction of the field. However, nearly all OPMs have "dead zones," which are orientations of the sensor with respect to the background field direction in which the sensor is inoperable. When atoms are optically pumped in our setup, the atomic spins are aligned with respect to an axis which is set by the direction of the pumping field or by the application of a magnetic field (we define the coordinate system based on this axis). Depending on the particular atomic state the atoms are in, selection rules only allow certain optical transitions to occur limiting the ability of the magnetometer or gradiometer to measure fields from arbitrary directions. Schemes have been invented to get around this problem (Wang et al., 2021), notably a rotation of the magnetometer itself, or a way to redistribute the atomic populations so that selection rules allow the optical transitions to occur along a measurement axis. The gradiometer shown in Figures 5.2 and 5.7 and in Campbell et al. (2022) uses an orthogonal pump/probe beam orientation and measures magnetic field gradients

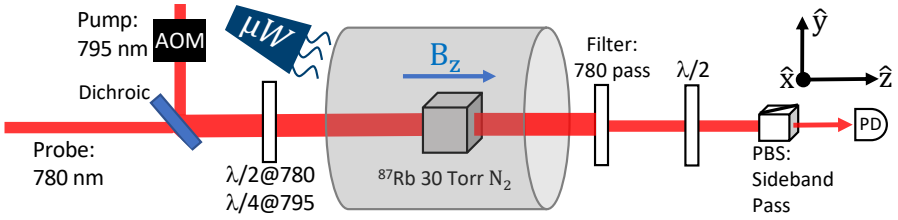

Figure 6.1: A schematic for the generation of sideband in the Colinear pump/probe configuration. Before entering the shield, the pump and probe beams are combined with a dichroic BS and pass through a dichroic waveplate which circularly polarizes the pump. The sidebands exit the shield and are measured on a photodiode with the background light extinguished by the PBS. A filter is added to reduce PD saturation during the pump phase.

along the probe axis when the background magnetic field is aligned with the pump optical axis. It cannot operate when the background magnetic field is perpendicular to the pump axis in the vapor cell, due to a degradation of optical pumping efficiency. This is also known as a planar dead zone. In this chapter, we describe a colinear pump/probe gradiometer based on microwave-optical sideband generation in a warm ensemble of ^{87}Rb atoms that is more compact than the orthogonal pump/probe sensor and is dead zone free. Compactness is especially useful for bio-magnetic applications (Jensen et al., 2016, 2018) such as magnetoencephalography (MEG) (Borna et al., 2020) since a small sensor footprint allows a greater number of sensors to be positioned around the skull.

6.2 Colinear Pump/Probe

We outline an experiment, similar to those described in Chapter 3, to demonstrate sideband generation in the colinear pump/probe orientation. This orientation is more compact than the orthogonal pump/probe orientation. As shown in Fig. 6.1, a vapor cell with the internal dimensions $8 \times 8 \times 8$ mm^3 is filled with warm^{87}Rb atoms and 30 Torr of N_2 buffer gas. A DFB laser at 780 nm (probe) is incident a Semrock dichroic beam splitter, angled at 45^o with respect to $\hat{z}$, with the beam passing directly through. A DFB laser at 795 nm (pump) is also incident the dichroic, but from an

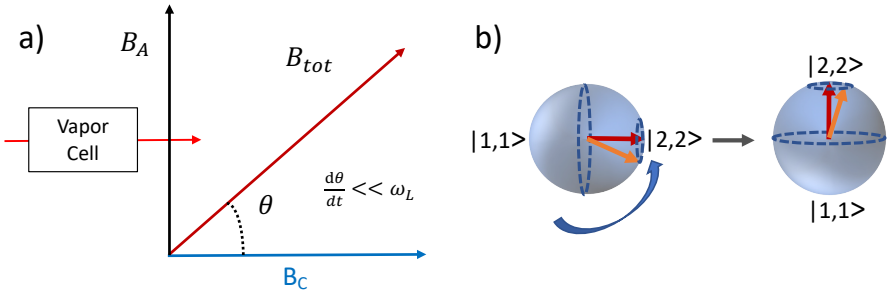

Figure 6.2: (a) A diagram showing the quantization axis rotation (QAR) method. A strong field B_c is applied along the laser axis and is then adiabatically ramped down such that the axis rotates towards the ambient field, B_A. (b) QAR can also be visualized as a rotation of the Bloch sphere by 90^o. The adiabatic rotation must be slow enough such that the Bloch (or spin) vector (orange) follows the torque vector (red) as the rotation occurs.

orthogonal angle to the probe. The dichroic reflects the pump light (like a mirror) towards the experiment, which combines the two beams into a single colinear beam. The beams then go through a Dichroic wave-plate with retardance $\lambda/2$ at 780 and $\lambda/4$ at 795, making the pump circularly polarized and the probe linearly polarized. A horn irradiates the vapor cell with microwave radiation tuned to the hyperfine splitting of the ^{87}Rb atoms plus the frequency shifts from the Zeeman effect and the buffer gas pressure. Then, the beams go through the vapor cell, generating sidebands. The sideband generation process is described in detail in Chapters 3 and 4. Upon exiting the cell the beams pass through a narrow band optical filter that allows 780 nm light to pass, extinguishing the 795 pump. We extinguish the pump to avoid photodiode saturation during the pumping cycle. The sidebands are orthogonally polarized with respect to the probe so a HWP and PBS are used to distinguish between the signal (sidebands) and background (probe) light on a photodiode (PD). In the next two sections we describe methods that can be used to measure magnetic fields both perpendicular to the laser axis, and along the laser axis, allowing for the operation of an atomic gradiometer at any angle with respect to the beam axis.

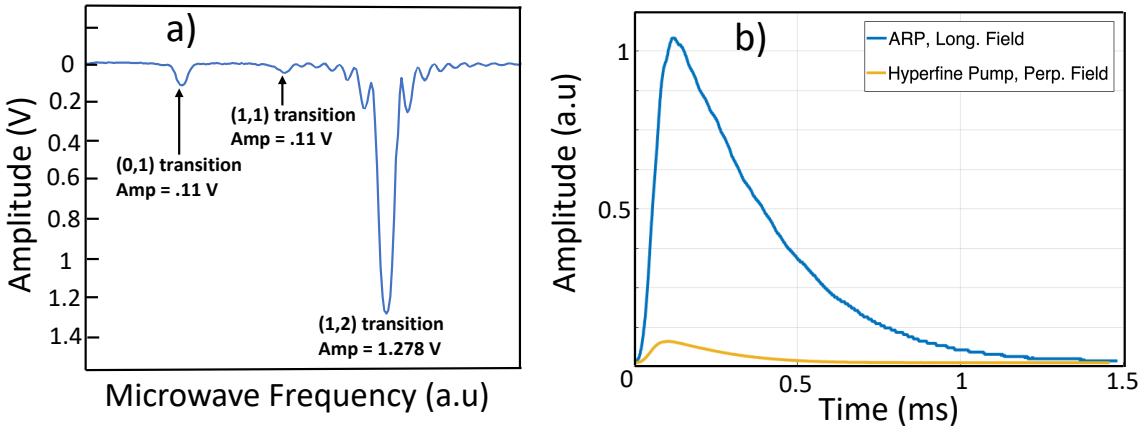

Figure 6.3: (a) We sweep across the MODR resonances after the QAR process is completed. It is estimated that $\sim 90\%$ of the atoms stay in the end-state after the completion of the rotation. (b) Sideband amplitude for the QAR method compared to hyperfine pumping. We see a $10\times$ increase inn signal amplitude with the QAR method.

6.3 Perpendicular B-field

If the background magnetic field is perpendicular to the direction of the laser propagation, the atoms are no longer pumped efficiently to the $|F = 2, m_F = 2\rangle$ end-state. Here, we provide an explanation for why this is the case. We define the quantization axis to be along the direction of the background magnetic field, which is perpendicular to the laser propagation direction. In this geometry, the background magnetic field splits the hyperfine ground states due to the Zeeman effect, allowing for a measurement of the field amplitude. However, with the quantization axis defined to be along the B-field, the atoms no longer "see" just σ^+ polarized light from the pump beam since it is spatially orthogonal to the B-field axis. In this case, the atoms see a combination of σ^+, σ^-, and π polarized light. This leads to a poor optical pumping efficiency and limits the effectiveness of the gradiometer. This problem is overcome by first applying a magnetic field, B_c, along the direction of the laser and then adiabatically rotating the magnetic field such that is points in the direction of the ambient field. In essence, we are rotating the magnetic field, and thereby the quantization axis, such that most of the atomic population is maintained in the $|F = 2, m_F = 2\rangle$ end-state

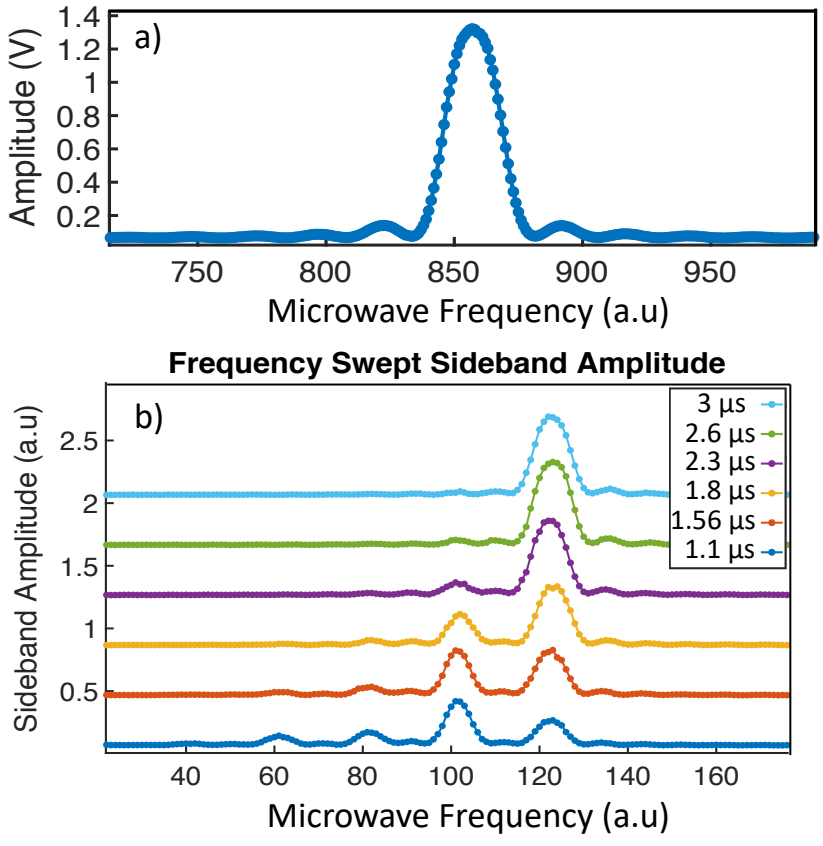

Figure 6.4: We sweep across the resonances and record the sideband signals (a) We sweep across the (2,1) transition after the QAR process. (b) We sweep across the resonances while the turnoff time of the QAR pulse is recorded. We achieve more population in the end-state for the quickest turnoff time.

while B_c is adiabatically ramped off. As shown in Fig. 6.2(a), we use a solenoid coil to apply a strong magnetic field ($\sim$ 100 μT) along the laser direction, setting the quantization axis parallel to the laser beam. Then, the atoms are optically pumped to the $|F = 2, m_F = 2\rangle$ state with pump light. We then adiabatically turn off the strong B-field until the quantization axis is rotated to be along the direction of the ambient field. We call this method the Quantization Axis Rotation (QAR) method. One can also think of this as a 90^o rotation of the Bloch sphere as shown in Fig. 6.2(b). In order for the rotation of the field to be adiabatic it must be sufficiently slower than the Larmor precession frequency, $\frac{d\theta}{dt} << \omega_L$, where θ is the angle of rotation of the quantization axis and ω_L is the Larmor precession frequency. Also, ω_L depends on

the strength of the applied B-field due to the Zeeman splitting, so the initial field must be strong enough to allow for a sufficiently fast rotation of the quantization axis. If the ambient field is weak, a bias magnetic field B_P is applied along the direction of the ambient field ensuring adiabatic rotation of the axis.

In order to determine how much population is left in the $|F = 2, m_F = 2\rangle$ state after the QAR method, we sweep across the microwave optical double resonance (MODR) signal, as shown in Fig. 6.3(a), and note the amplitude of the resonance dip for the desired transition. The MODR signal can be measured by rotating the HWP before the polarizer by 90°, which extinguishes the sidebands and passes the probe light. To measure the MODR amplitude, a LabVIEW program was developed which takes a single data point per probe cycle (2 ms period at 50% duty cycle) at the same point in time in each cycle, while the frequency of the microwave field is slowly swept ($\sim$ 10 seconds) across the hyperfine ground state manifold. By measuring the amplitude of the desired state with respect to the other transitions, we estimate that approximately 90% of the population is left in the $|F = 2, m_F = 2\rangle$ state after the axis rotation occurs. In Fig. 6.3(b) we show the sideband generated after the QAR experiment and compare the sideband amplitude to the amplitude of a sideband generated after hyperfine pumping (Section 6.5) only. With the QAR method, nearly all the population is shifted to the end state and thus there is more atomic population involved in the sideband generation process. We see approximately a ten times improvement in signal amplitude by using the QAR method versus the hyperfine pumping method.

One can also sweep the microwave frequency across the hyperfine ground state resonances and measure the amplitude of the sideband signal. Fig. 6.4(a) shows a frequency scan across the (2,1) transition after the QAR process is complete. Fig. 6.4(b) shows a sweep across the hyperfine resonances while the turnoff time of the QAR pulse is varied. By progressively slowing down the turnoff time we were able to maximize the atomic population found in the $|F = 2, m_F = 2\rangle$ state, thus increasing the sideband amplitude produced on the (2,1) transition. We were unable to turn

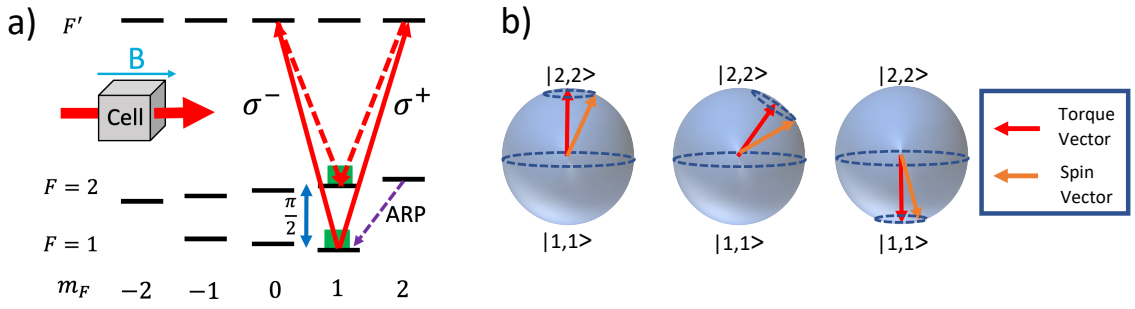

Figure 6.5: (a) Energy level diagram showing the Λ systems which produces sidebands for B-fields aong the axis of the laser. In this case, ARP is used to transfer population from $|F = 2, m_F = 2\rangle$ to $|F = 1, m_F = 1\rangle$. Then, a $\pi/2$ pulse is applied on the (1,1) transition. (b) A Bloch vector representation of Adiabatic Rapid Passage (ARP). The movement of the torque vector must be slow enough that the Bloch vectors continues to precess around the torque vector as it moves from $|F = 2, 2\rangle$ to $|F = 1, 1\rangle$.

off the field faster than ~ 1 μs because we were limited by the turnoff speed of the coils. We found that by increasing the magnitude of B_c, the pumping efficiency was increased for a turnoff of 1 μs. The lower limit to the turnoff time allowed us to perform the QAR process with a square wave turnoff, while still maintaining most most of the population in the $|F = 2, m_F = 2\rangle$ state.

6.4 B-field parallel to the laser axis

If the ambient field is along the probe laser propagation direction ($\hat{z}$-direction) sidebands are no longer generated when a $\pi/2$ pulse is applied between the $|F = 1, m_F = 1\rangle$ and $|F = 2, m_F = 2\rangle$ end-states due to selection rules. A description of the relevant selection rules is provided in Chapter 2. Linearly polarized light traveling along the direction of the ambient field is a superposition of σ^+ and σ^- light, which means the atoms can only drive transitions with those polarizations. For example, if the atoms are pumped to the $|F = 2, m_F = 2\rangle$ state and the probe is detuned to the $|F = 1, m_F = 1\rangle$ state, the probe would need to makes the transitions $|1, 1\rangle \xrightarrow{\sigma^+} |2', 2\rangle \xrightarrow{\pi} |2, 2\rangle$ in order for sideband generation to occur. However, since a

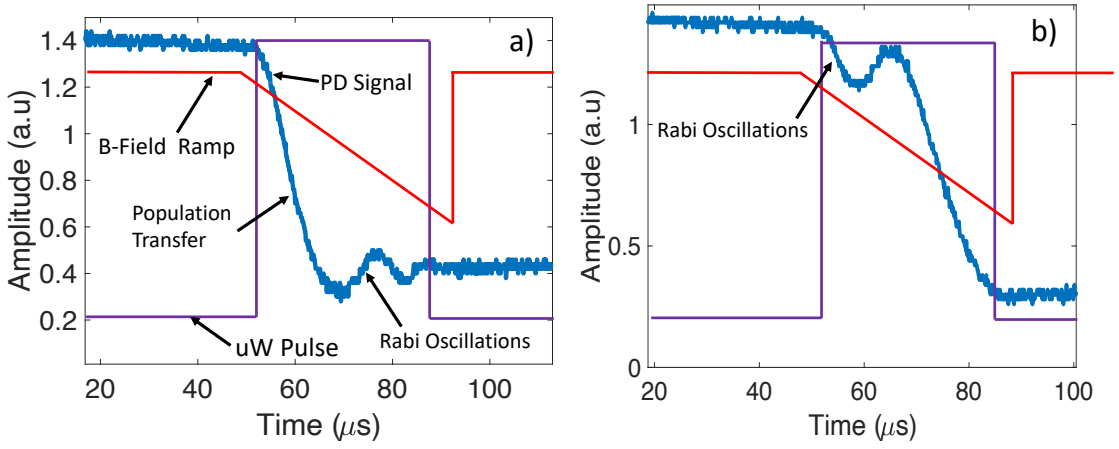

Figure 6.6: (a) Probe measurement of the adiabatic turnoff in the vapor cell. The microwave field induces Rabi oscillations after the state transfer. (b) The microwave field frequency is shifted to show Rabi oscillations before the state transfer is completed.

π photon is needed to complete the Λ system, this two-photon transition is not able to occur for this probe orientation. In order to overcome this difficulty, we build a Λ system with just σ^+ and σ^- transitions. Fig. 6.5(a) shows an energy level diagram of the Λ systems generated in this configuration. A $\pi/2$ pulse is applied to the $|F = 1, m_F = 1\rangle \leftrightarrow |F = 2, m_F = 1\rangle$ transition putting the atoms in a superposition of the two states. The probe is frequency detuned to the $|F = 1, m_F = 1\rangle$ state in this case and makes two-photon Λ transitions to the excited state and then back down to the $|F = 2, m_F = 1\rangle$ state completing the transition. The two generated sideband photons have σ^+ and σ^- polarization and combine to form a linearly polarized sideband signal which is still orthogonally polarized to the probe beam because of a 90^o phase shift as the atoms complete the two-photon transition.

To prepare the appropriate starting state, we need to transfer population from the $|F = 2, m_F = 2\rangle$ state to the $|F = 1, m_F = 1\rangle$ state. A common method to transfer population from one state to another in a two level system is using a π pulse. However, the π pulse method is not generally robust due to fluctuations in the pulse area and to inhomogeneities in the atoms. Also, in the gradiometer application described in Chapter 5, there are two vapor cells with different buffer gas pressures (15 and 30

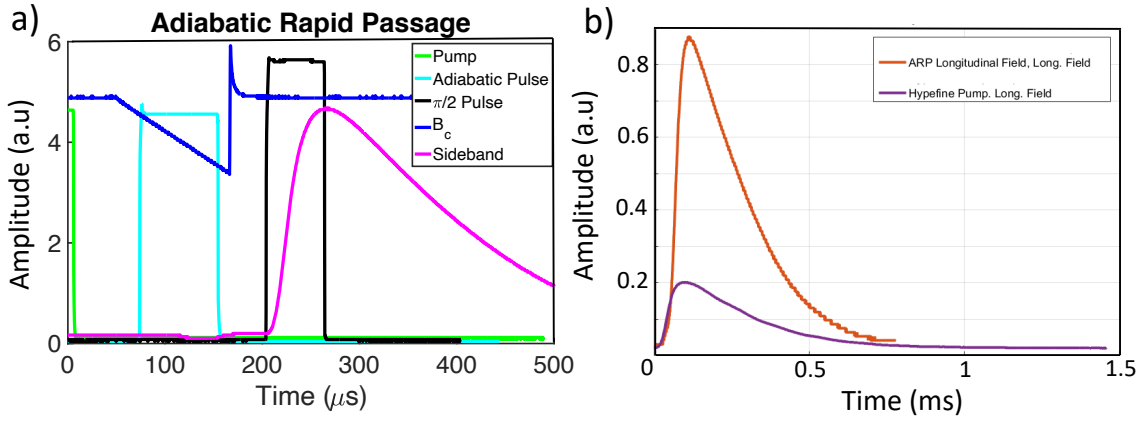

Figure 6.7: (a) Sideband signal generated from the ARP technique. All of the other applied fields are included in the oscilloscope trace. (b) Sideband amplitude after ARP vs. hyperfine pumping.

torr of N_2), resulting in a different hyperfine frequency in each vapor cell. A perfect π pulse in one cell may not be a perfect π pulse in the other. A more robust method to transfer population is Adiabatic Rapid Passage (ARP) (Simon, 2009). ARP occurs when the microwave frequency is tuned below or above the resonance and is then adiabatically swept across the resonance while simultaneously a microwave field is applied at the frequency of the resonance. Similarly, the resonance level itself can be swept by varying the amplitude of an externally applied magnetic field. By sweeping the level across the resonance in the ARP process, the two cells may have a different resonant hyperfine frequency, among other inhomogeneities, yet the population is still transferred efficiently between the states. The adiabatic condition is satisfied when (Malinovsky and Krause, 2001)

$$\sqrt{\Omega(t)_R^2 + \Delta\omega(t)^2} \gg |\frac{d}{dt}\theta(t)_T| \tag{6.1}$$

where $\Omega(t)_R$ is the Rabi frequency, $\Delta\omega(t) = \omega(t) - \omega_{12}(t)$ is the frequency detuning between the incoming radiation, $\omega(t)$, and the resonance $\omega_{12}(t)$, $\theta(t)_T$ is the phase angle of the torque vector on the block sphere. The torque vector must rotate slow enough on the block sphere from $|F = 2, m_F = 2\rangle \rightarrow |F = 1, m_F = 1\rangle$ such that the population is adiabatically transferred between levels. In this way, it is theoretically

possible for population to be coherently transferred between two states with 100% efficiency.

Fig. 6.6(a) shows a plot of the ARP state transfer process. The probe is detuned to the $|F = 1, m_F = 1\rangle$ state, and its amplitude is measured on a photodiode by rotating the HWP before the PBS such that the sideband signal is extinguished and the orthogonally polarized probe passes through the PBS. There is high transmission initially because most of the atoms have been optically pumped to the $|F = 2, m_F = 2\rangle$ state. Then, the amplitude of the B-field is swept through the resonance ($\sim 40\ \mu s$). While the B-field sweep is occurring, a microwave pulse at constant frequency is applied to the atoms at the frequency of the resonance, completing the ARP transfer. After the adiabatic transfer, the probe amplitude has been reduced dramatically due to atoms populating the previously empty sublevel. After the transfer, Rabi oscillations begin to occur due to the applied microwave field, as shown in Fig. 6.6(a). In Fig. 6.6(b), we shift the microwave frequency such that the Rabi oscillations occur before the atoms have been transferred. By tuning the microwave pulse frequency to be in-between these two cases, the most efficient transfer of atomic population can be achieved.

In Fig. 6.7(a) we show the signal traces for the pump (green), the adiabatic pulse (light blue), the $\pi/2$ pulse (black), B_c (dark blue), and the sideband signal (pink) produced during the ARP experiment. We separated the microwave pulses by about 80 μs in order to easily show the pulses for the diagram. First, the pump light (green) is applied and then turned off initiating T_1 relaxation between the states. Then the ARP process is applied as shown in Fig. 6.6. The slope of the sweep was tuned by monitoring the amplitude of the sideband on a PD and then maximizing it. We believe the spike on B_c after the magnetic field sweep is an inductive spike due to a quick change in amplitude of the field going through the coils. Soon after, a $\pi/2$ pulse is applied to the $|F = 1, m_F = 1\rangle \leftrightarrow |F = 2, m_F = 1\rangle$ transition putting the atoms in a coherent superposition of the two ground states which generates a sideband. We do not see the transfer in population from the ARP process like we

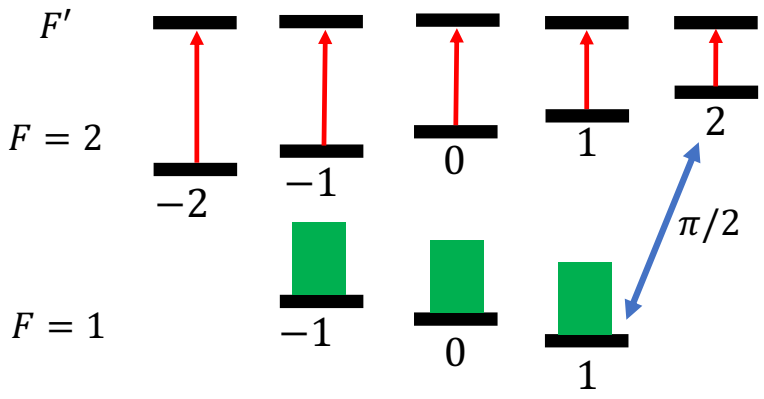

Figure 6.8: A schematic which shows the hyperfine pumping process for for a laser beam detuned to the $|F = 2\rangle$ hyperfine manifold. A net migration of atoms towards the $|F = 1\rangle$ occurs, creating a population imbalance between the manifolds.

did in Fig. 6.6 because the probe signal is orthogonally polarized with respect to the sideband and is extinguished by the PBS. Fig. 6.7(b) shows the sideband generated from the ARP process with a comparison to the sideband generated with hyperfine pumping (Section 6.6). The ARP sideband signal is about 4 times bigger than the signal generated with hyperfine pumping.

6.5 Hyperfine Pumping

We use hyperfine pumping signals as a reference for the signals generated in this chapter. Fig. 6.8 shows a schematic of the hyperfine pumping process. Hyperfine pumping is when a linearly polarized pump laser is frequency detuned to one of the ground state hyperfine manifolds; let's say $F = 2$. Much of the atomic population is shifted to the $F = 1$ manifold because the laser continuously clears the $F = 1$ manifold. This allows for the generation of sidebands on all the ground state transitions because all states in the manifold are populated with atoms. However, unlike circularly polarized optical pumping, all of the population is spread out between the ground state sublevels, and thus, the signals are smaller in amplitude. However, these signals are good reference for our other experiments so we can determine if our state transfer

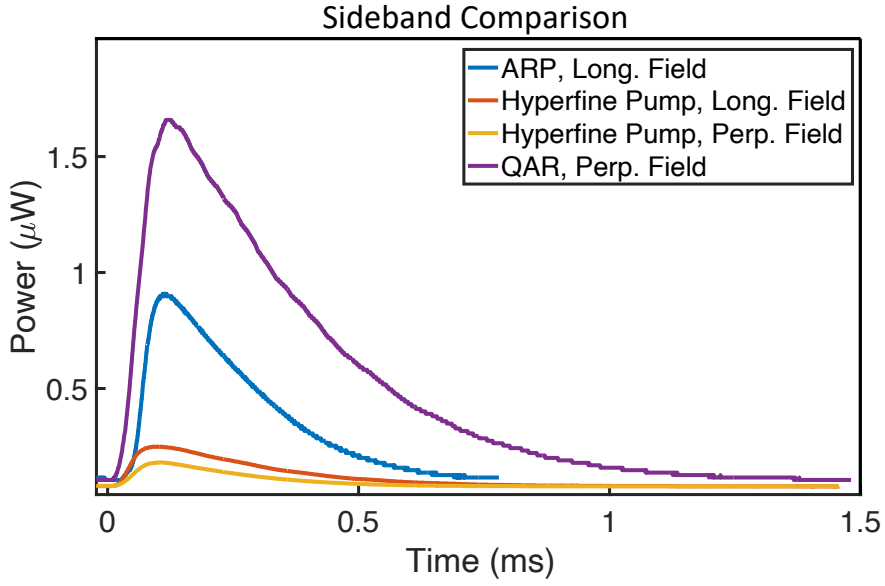

Figure 6.9: Comparison of the sideband signals for the QAR, ARP, and hyperfine pumping methods. The QAR signal is significantly stronger than the ARP signal, likely due to an inefficient state transfer process.

processes is enhancing the signal quality.

6.6 Sideband Comparison

In Fig. 6.9, we show a comparison of all four signals described in the previous section on the same plot. All four experiments were taken on the same day with the same experimental parameters, besides necessary changes to switch between experiments. The $\pi/2$ pulse was applied at the same time offset from the pump turnoff for each experiment, which gives a direct comparison of the sideband amplitudes for each method. The sideband signal amplitude is given in units of power by dividing the signal voltage by the responsivity (A/W) and gain of the PD (V/A) to calculate the approximate signal amplitude in Watts. Notice that the sideband amplitude of the QAR experiment is about a factor of two larger than the sideband signal generated in the ARP experiment. We are unsure why the ARP signal is smaller since the ARP process should be as, if not more, efficient than the QAR method. We performed

another experiment (not shown) where we used a π pulse instead of adiabatic passage to transfer the atomic population from $|F = 2, m_F = 2\rangle \rightarrow |F = 1, m_F = 1\rangle$ to understand why the sidebands produced in the ARP experiment are smaller than the ones produced in the QAR experiment. We found that in using a π pulse, sideband signals are produced with the same amplitude as the sidebands produced in the QAR experiment. This is evidence that the ARP process was inefficient in our experiment, and there is not an inherent sideband amplitude reduction by using this particular atomic transition.

6.7 Colinear Gradiometer Physics Package

Based on the colinear pump/probe orientation described in Fig. 6.1 a miniaturized physics package was developed by collaborators at QuSpin which is shown in Fig. 6.10. In order to reduce complexity and ensure beam overlap the 795 nm pump and 780 nm probe beams were combined into a single polarization maintaining fiber before entering the sensor package. To operate in pulsed mode, a high-speed optical switch (Boston Applied Technologies) was added to the pump optical fiber and a variable attenuator (Agiltron) was added to the probe optical fiber. Approximately $3 - 4$ mW of pump power and 1.5 mW of probe power was measured at the entrance of the sensor head. To ensure fiber coupling, the 795 nm and the 780 nm beams were orthogonally linearly polarized at the entrance of the sensor head. In order to prepare the correct optical polarization for the two beams, a custom dichroic waveplate **F** ($\lambda/2$ at 795 nm and λ at 780 nm) was used to rotate the polarization of the pump beam such that the two beams have the same polarization. Both beams then pass through a polarizing beam splitter (**PBS**) and subsequently through a dichroic waveplate **H** ($\lambda/4$ 795 nm, $\lambda/2$ 780 nm) which circularly polarizes the 795 nm pump light and leaves the 780 nm probe light linearly polarized Johnson et al. (2010). Next, the two beams were collimated with an 84 mm focal length optical lens. The two beams then pass through the two vapor cells and are retroreflected

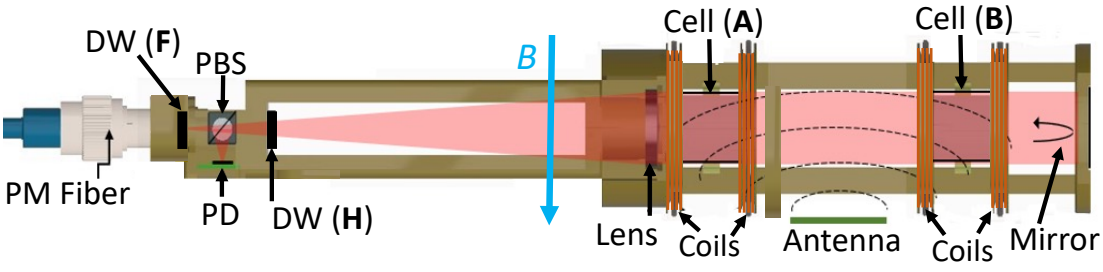

Figure 6.10: A schematic of the gradiometer sensor head in the collinear pump/probe configuration. The sensor is run in multipass mode so a mirror is used to reflect the light back through the cell where a PBS passes the sideband signal to a PD.

by a mirror placed 2.2 cm away from the second vapor cell and then retraced their original path. The optical sidebands which are orthogonally polarized with respect to the probe light was reflected by the polarizing beam splitter and directed onto a PD. Vapor cells **A** and **B** are each surrounded by a pair of Helmholtz coils which provide a 300 μT bias field ($5-10$ times Earth's field) during the optical pumping phase of the cycle. After pumping, the bias field is adiabatically switched-off to align the spins with the background field before applying the microwave $\pi/2$ pulse. No noticeable change in amplitude of the beat-note signal was observed in the colinear variant versus the miniaturized physics package developed in Section 5.8. In future experiments, we want to measure sideband signals for magnetic fields applied along the probe axis and record how the noise floor of the colinear gradiometer compares to the orthogonal orientation physics package developed in Section 5.8.

6.8 Beats Within a Single Cell

If one looks closely at Fig. 6.9, it can be seen that there are oscillations along the sideband profile. These oscillations are actually interference beats between sidebands generated within the same vapor cell but from other Λ transitions. This effect becomes apparent when the QAR process is not 100% efficient, and population leaks out into other sublevels. In Fig. 6.11 we show an experiment to verify our hypothesis that

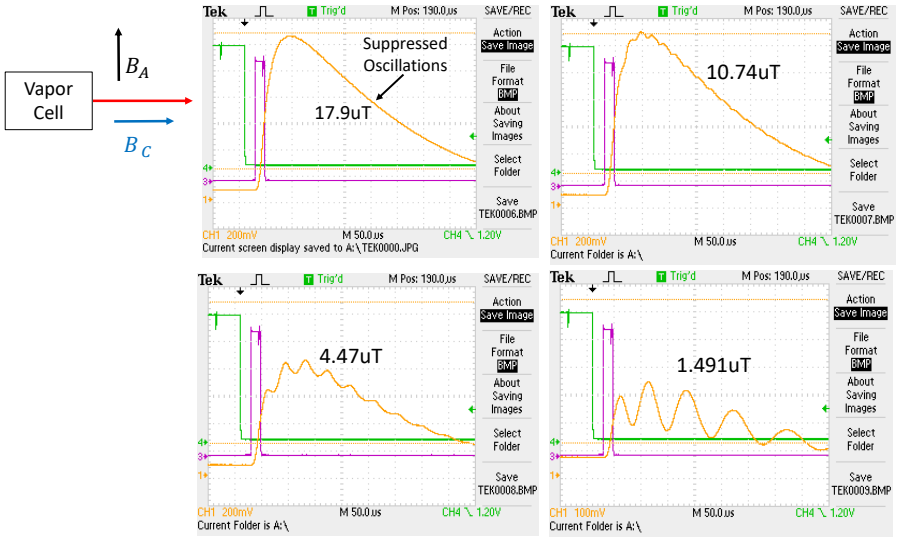

Figure 6.11: Sideband beat-notes generated from sideband interference in the same vapor cell. For strong B_A the beats are nearly invisible as most of the population stays in the end-state. As the amplitude of B_A decreases, the beats become progressively more apparent. This is because the rotation of the quantization axis is not efficient.

the oscillating signal along the sideband profile is quantum beats between disparate sublevels. Using the experimental setup shown in Fig. 6.1, we apply a relatively strong B-field along B_c ($\sim 100\ \mu$T, see Fig. 6.2). Then, we lower the field strength, B_A, until beats are produced. The quantization axis rotation method is not an efficient process for low B_A because the condition of adiabaticity is not maintained as the field becomes small during the B_c turn off. This causes population to leak into the other sublevels. For the lowest B_A field strengths the oscillation is more visible. Also, since the beat is being produced from close lying states separated by the Zeeman splitting, the oscillation frequency is the Larmor precession frequency between close lying energy levels.

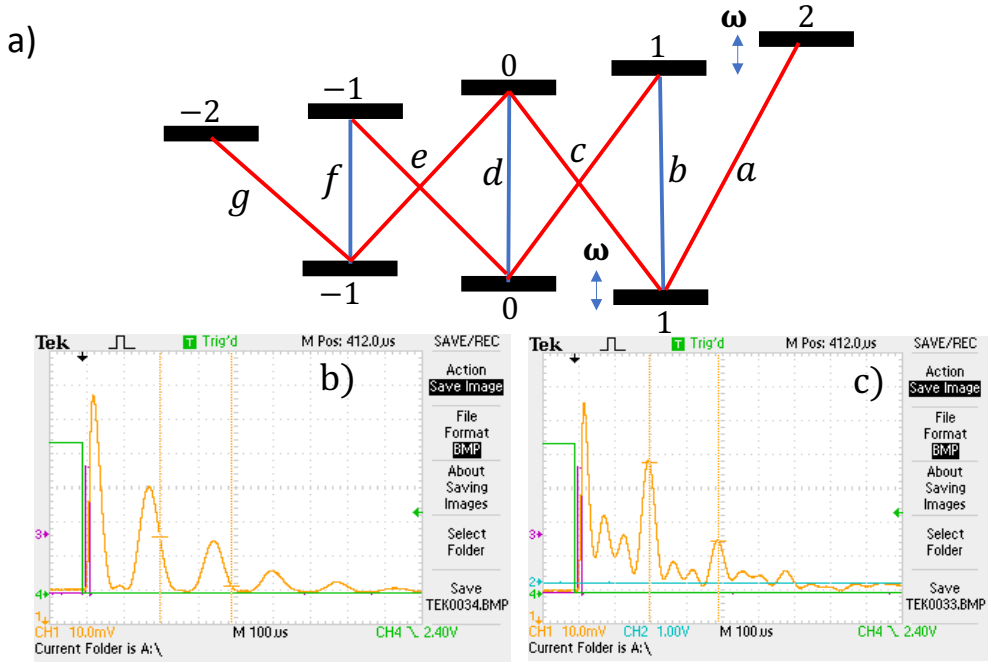

Figure 6.12: (a) Possible microwave transitions on the ground state manifold of ^{87}Rb. (b) Beat-note signal for the case of a low-amplitude field applied along the laser axis. There are three sideband signals beating together to form this beat-note. (c) Beat-note signal for a field applied in the perpendicular direction to the laser propagation. In this case there are four sideband signal which beat together.

6.9 Low-field Beats

Another experiment was performed where we measured the beats produced within the same vapor cell. The beat-note signal was measured at low magnetic field both along the direction of laser propagation and in the perpendicular direction. For these measurements, ARP and QAR methods were not used, just hyperfine pumping to shift population to one of the hyperfine ground state manifolds. For B-fields applied along the laser axis, only two-photon Λ transitions involving σ^+ and σ^- polarized light are possible due to optical selection rules (Chapter 2). In Fig. 6.12(a) we show the seven possible microwave transitions between the ground states (e and c involve two degenerate transitions). The blue colored transitions (f, d, and b) are the $\Delta m_F = 0$ microwave transitions which produce sidebands for this experimental configuration. Looking at Fig. 6.5(a) it can be seen that σ^+ and σ^- optical transitions are needed

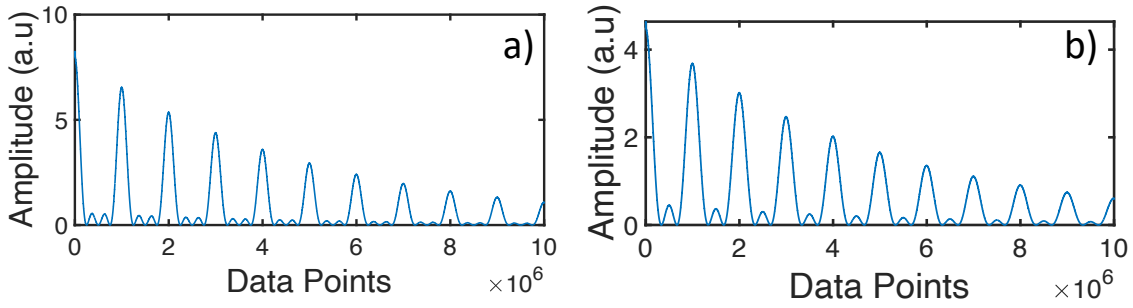

Figure 6.13: We numerically model the beat-note process. (a) Moving average of the data for the case of four optical fields beating together showing the simulated PD signal. (b) Moving average of the data for the case of 3 optical fields beating together.

to form the Λ transitions needed to generate sidebands for $\Delta m_F = 0$ microwave transitions. Fig. 6.12(b) shows an oscilloscope trace of the beat-note generated for this experiment, which involves the interference of three sideband signals.

For B-fields applied perpendicular to the direction of laser propagation, a coherent superposition of ground states generated on the red transitions in Fig. 6.12(a) will generate sidebands. For this experimental configuration, optical selection rules (Section 2.4) dictate that the beam is a combination of σ^+, σ^-, and π light. There are four transitions which are allowable for this orientation, and they are (a, c, e, and g). Fig. 6.12(c) shows a beat-note produced for this experimental configuration where four sideband signals are beating together.

In order to replicate the features shown in Fig. 6.12, we model the beat-note generated from the interference of four optical signals. For the case of three optical fields, we set the amplitude of one of the sidebands to zero. The power of the resulting beat between the four oscillating fields fields is proportional to the square of the electric field, so we write out the equation as

$$P_B = (E_1\cos(2\pi\omega_1 t + \phi_1) + E_2\cos(2\pi\omega_2 t + \phi_2) + E_3\cos(2\pi\omega_3 t + \phi_3) + E_4\cos(2\pi\omega_4 t + \phi_4))^2 e^{-t/T_2} \quad (6.2)$$

where E_1, E_2, E_3, and E_4 are the electric field amplitudes of the four oscillating fields, ω_1, ω_2, ω_3 and ω_4 are the frequencies of the four fields, ϕ_1, ϕ_2, ϕ_3, and ϕ_4

are the phases of the four fields, and T_2 is the decoherence time. As shown in Fig. 6.12(a), we let the frequency separation between the Zeeman transitions be given by ω. Thus, the frequency separation between sidebands generated on transition b and transition d is 2ω and between b and f is 4ω. Similarly, the frequency separation between transition a and c is 2ω, and between a and g is 6ω. We take this fact into account when defining the frequencies of each field. As shown in Fig. 6.13(a), we plot Eqn. 6.2 for 10 million data points with the waves oscillating at the frequency of 1 oscillation per 10 data points, and for the case of a perpendicular B-field. In the physical experiment, the waves are oscillating at the frequency of the incoming optical radiation. However, the actual oscillation frequency is not relevant for this particular experiment because the PD can not measure oscillation frequencies at the optical frequencies. In Fig. 6.13, we take a moving average of the nearest 100 data points to show what the signal looks like on the PD. The only oscillation frequency that is apparent on the plot is the Larmor precession frequency between the sublevels, or multiples of it. In Fig. 6.13(b) we perform a similar calculation but for the case of a longitudinal field. We set the amplitude of the fourth field to zero and plot the beat-note signal for the interference of three fields. Comparing the results of Fig. 6.12 and Fig. 6.13 it is clear that we are observing beat-notes between sidebands generated in the same vapor cell. This method is a useful tool to demonstrate quantum beating between the sublevels in the hyperfine ground state.

6.10 Single Laser Variant

In order to further simplify the experimental configuration and increase the compactness of the sensor, we show that it is feasible to use a single laser beam as both pump and probe. As shown in Fig. 6.14(a), a linearly polarized laser tuned to the D1 line (795 nm wavelength) of rubidium passes through a QWP, circularly polarizing the light. The light is then incident on a vapor cell filled with a warm ensemble of ^{87}Rb atoms (30 Torr buffer gas), which is recycled from previous experiments. We use an

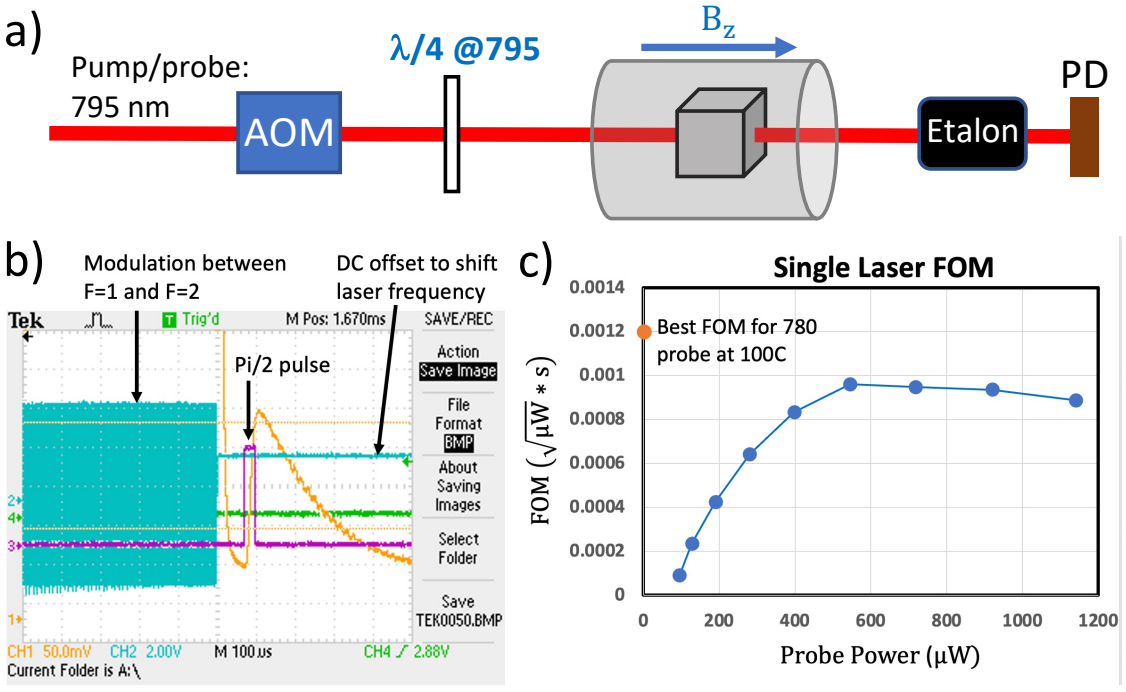

Figure 6.14: Experimental setup for the single laser variant, where the pump and probe beams are the same laser. The AOM is used to attenuate the beam during the probing phase and an etalon is used as a frequency discriminator to separate the sideband light from the background probe light (b) An oscilloscope trace showing sideband generation in the single laser variant. (c) A plot of the sideband FOM with the single laser setup (blue) for various probe powers. The best FOM for the 780 nm probe setup described in Chapter 3 (orange) is also shown for comparison.

AOM as an optical switch to create the "Pumping" and "Probing" phases for the experiment. The optical power is lowered during the probing phase by attenuating the amplitude of the 80 MHz RF field driving the AOM. A mechanical RF switch toggles between low optical power ($\sim 10\ \mu$W) and high optical power (~ 5 mW) when a voltage (5 V) is applied to the TTL port of the switch. During the probing phase, the frequency of the laser is detuned from the $F = 1$ or $F = 2$ atomic resonances by applying a DC offset to the laser controller. The detuning ensures the sideband light passes through the cell without getting quickly absorbed, which would severely limit the sensitivity of the resulting gradiometer. For this experimental configuration, both the pump and probe beams are σ^+ circularly polarized, since they are the same laser. When the applied B-field is in the direction of the laser, σ^+ light drives the atoms

to the excited state, with the scattered sideband light also σ^+ polarized. Thus, the sidebands and probe have the same polarization and cannot be separated using a PBS as a polarization selector. Another way to separate the sidebands from the probe is by using an etalon, or an optical cavity, that is temperature tuned to the mode of a first order sideband, suppressing the probe light. We use a fused silica etalon with a free spectral range of 21.6 GHz as a frequency discriminator. The outside diameter is wrapped with a twisted pair of Phospher Bronze heater wire connected to a power supply for temperature tuning. A 3D printed mount was designed for the etalon to sit in surrounded by a layer of insulation. The temperature of the cavity is slowly tuned until the sideband signal becomes apparent, and then is maintained at that temperature for several minutes tp suppress temperature inhomgenieties in the fused silica. Just as before, a PD is placed after the etalon to record the generated optical sideband. In Fig. 6.14(b) we show an oscilloscope trace of a sideband signal generated using the experimental setup described in Fig. 6.14(a). The green trace on Fig. 6.14(b) is a the voltage applied to the current driver of the laser. First, we modulate the laser current with a square wave at 200 kHz with the minima and maxima of the waveform corresponding to the frequencies of the $|F = 1\rangle$ and $|F = 2\rangle$ ground state manifolds. This helps clear population in states other than the intended dark state by switching the pumping field between the two ground state manifolds. Then, the amplitude of the beam is attenuated with the AOM and the probing phase beings. About $80\mu s$ after the pump turns off we apply a $\pi/2$ pulse generating the sideband signal which is measured from the temperature tuned etalon. In Fig. 6.14(c) we show a plot of the Figure of Merit (FOM) for the single laser variant with respect to probe power. We also compare the results of this experiment with the results from the best FOM measuremnt made in the orthogonal pump/probe experimental setup described in Chapter 3. We find that sideband properties in the single laser configuration are comparable to the sidebands generated in other experimental configurations of the gradiometer, indicating that this method could be used in a gradiometer physics package in the future.

Chapter 7

Conclusion and Outlook

We conclude this dissertation and present a summary of the results we achieved. In addition, we provide a brief description of experiments that we would like to run in the future to improve our experimental results.

7.1 Summary

In this thesis, we develop a novel atomic gradiometer based on the interference of stimulated optical sidebands. In Chapter 1 we introduce the reader to atomic magnetometers and gradiometers, and provide an explanation on the novelty of our work compared to the literature.

In Chapter 2, we lay down the conceptual framework needed to understand the experiments in this thesis. For example, we describe the level spitting of rubidium vapor, the optical pumping process, and the effect of buffer gas in the vapor cell.

In Chapter 3, we provide experimental evidence of sideband generation. We experimentally show sideband generation for the "steady-state" case, where the pump and microwave fields are always on, and for the case of a "pulsed experiment", where the pump and microwave fields are turned off when measurements are made. We

then conduct a study of vapor cells filled with various buffer gas pressures and define a parameter (FOM) to conclude that 15 Torr and 30 Torr buffer gas pressures work the best for our experiments.

In Chapter 4 we describe the theory of sideband generation process in detail. Starting with Maxwell's equations, we derive a propagation equation for the sidebands as they travel through a vapor cell. We then solve the propagation equation and develop a numerical model which predicts the behavior of the sidebands. We then perform an experiment which validates the accuracy of our theoretical model and numerical calculations.

In Chapter 5 we build an atomic gradiometer based on the interference of the sidebands described in earlier chapters. We then make some preliminary measurements of the noise floor ($\sim 1\frac{pT}{\sqrt{Hz}cm}$) using the tabletop experimental setup. This motivated our collaborators at QuSpin to build a 3D printed miniaturized version of the gradiometer. They measured a noise floor of 25 fT/cm $\sqrt{Hz}$ in a room without magnetic shielding, which is nearing state-of-the-art sensitivity.

In Chapter 6 we perform experiments to show the feasibility of operating the gradiometer in magnetic gradients from all spatial directions, making the gradiometer dead-zone-free. This is useful for applications since multiple components of the gradient field can be measured without physically rotating the apparatus.

7.2 Future Experiments

Measuring the beat-note frequency generated from the interference of microwave optical sidebands has proven to be an excellent method for measuring magnetic field gradients. In this section, we describe experiments that we would like to perform in order to improve the operation of the sensor.

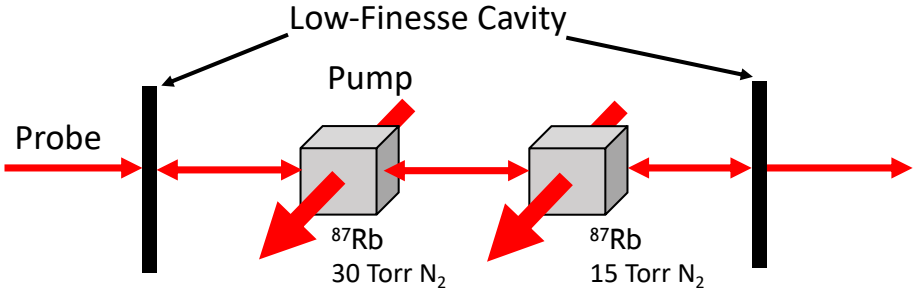

Figure 7.1: Simplified experimental diagram for the proposed experiment described in section [xx]. The two vapor cells in the atomic gradiometer are put inside a low-finesse cavity which should increase the sideband signal amplitude while maintaining the T_2 decoherence time.

7.2.1 Operational Dead-Zone-Free Gradiometer

In Chapter 6 we develop a blueprint to make a colinear pump/probe magnetic gradiometer for measuring fields from all directions with respect to the quantization axis. Collaborators at QuSpin also developed a miniaturized module based on the quantization axis rotation (QAR) method which showed sideband amplitudes equivalent to the orthogonal pump/probe configuration. However, a working dead-zone-free gradiometer which measures magnetic field gradients from all directions has not yet been demonstrated. Here we propose a way to operate such a gradiometer.

1. Determine the direction of the ambient magnetic field by zeroing the background field.
2. Select a scheme based on the ambient field direction.
3. Start the pulsed gradiometer operation by applying microwave a $\pi/2$ pulse etc.
4. During operation, monitor the signal size. If the signal amplitude drops below a predetermined threshold then switch schemes.
5. If the signal disappears, re-zero the field and restart the process from step 1.

7.2.2 Low-finesse Cavity

Two of the limiting factors for obtaining good sensitivity in our gradiometer setup are the decoherence time, T_2, and the signal amplitude. One way to increase signal amplitude is by heating the cell, which increases the number density. However, this leads to linewidth broadening which shortens the T_2 time. One way to circumvent this is to put the atomic vapor cells inside a low finesse (≈ 10 passes) optical cavity as shown in Fig. 7.1. The signal amplitude is increased due to the increased length of vapor cell the light passes through, but the T_2 should be comparable to the original gradiometer, which will lower the magnetic noise floor since the noise is $\propto \sqrt{S_A}$ where S_A is the signal amplitude.

References

S. Abend, M. Gersemann, C. Schubert, D. Schlippert, E. M. Rasel, M. Zimmermann, M. Efremov, A. Roura, F. Narducci, W. P. Schleich, et al. Atom interferometry and its applications. *Foundations of quantum theory*, 197:345, 2019. 1

J. Allred, R. Lyman, T. Kornack, and M. V. Romalis. High-sensitivity atomic magnetometer unaffected by spin-exchange relaxation. *Phys. Rev. Lett.*, 89(13): 130801, 2002. 3, 81

A. André, A. S. Sørensen, and M. D. Lukin. Stability of atomic clocks based on entangled atoms. *Phys. Rev. Lett.*, 92:230801, Jun 2004. doi: 10.1103/PhysRevLett.92.230801. URL https://link.aps.org/doi/10.1103/PhysRevLett.92.230801. 1

M. Arditi and T. R. Carver. Hyperfine relaxation of optically pumped rb^{87} atoms in buffer gases. *Phys. Rev.*, 136:A643–A649, Nov 1964. doi: 10.1103/PhysRev.136.A643. URL https://link.aps.org/doi/10.1103/PhysRev.136.A643. 5

M. Auzinsh, D. Budker, and S. Rochester. *Optically polarized atoms: understanding light-atom interactions*. Oxford University Press, 2010. 12

J. Bateman, A. Xuereb, and T. Freegarde. Stimulated raman transitions via multiple atomic levels. *Phys. Rev. A*, 81:043808, Apr 2010. doi: 10.1103/PhysRevA.81.043808. URL https://link.aps.org/doi/10.1103/PhysRevA.81.043808. 35

B. Bean and R. Lambert. Temperature dependence of hyperfine density shifts. iv. na

23, k 39, and rb 85 in he, ne, ar, and n 2 at low temperatures. *Physical Review A*, 13(1):492, 1976. 17

W. E. Bell and A. L. Bloom. Optical detection of magnetic resonance in alkali metal vapor. *Physical Review*, 107(6):1559, 1957. 2

S. Bize, P. Laurent, M. Abgrall, H. Marion, I. Maksimovic, L. Cacciapuoti, J. Grünert, C. Vian, F. P. dos Santos, P. Rosenbusch, P. Lemonde, G. Santarelli, P. Wolf, A. Clairon, A. Luiten, M. Tobar, and C. Salomon. Cold atom clocks and applications. *Journal of Physics B: Atomic, Molecular and Optical Physics*, 38(9):S449–S468, apr 2005. doi: 10.1088/0953-4075/38/9/002. URL https://doi.org/10.1088/0953-4075/38/9/002. 1

A. Borna, T. R. Carter, J. D. Goldberg, A. P. Colombo, Y.-Y. Jau, C. Berry, J. McKay, J. Stephen, M. Weisend, and P. D. Schwindt. A 20-channel magnetoencephalography system based on optically pumped magnetometers. *Physics in Medicine & Biology*, 62(23):8909, 2017.

A. Borna, T. R. Carter, A. P. Colombo, Y.-Y. Jau, J. McKay, M. Weisend, S. Taulu, J. M. Stephen, and P. D. Schwindt. Non-invasive functional-brain-imaging with an opm-based magnetoencephalography system. *Plos one*, 15(1):e0227684, 2020. 83

E. Boto, N. Holmes, J. Leggett, G. Roberts, V. Shah, S. S. Meyer, L. D. Muñoz, K. J. Mullinger, T. M. Tierney, S. Bestmann, et al. Moving magnetoencephalography towards real-world applications with a wearable system. *Nature*, 555(7698):657–661, 2018. 3

V. B. Braginsky, F. Y. Khalili, and K. S. Thorne. *Quantum Measurement*. Cambridge University Press, 1992. doi: 10.1017/CBO9780511622748. 4

D. Budker and M. Romalis. Optical magnetometry. *Nature physics*, 3(4):227–234, 2007. 2

J. C. Camparo. The rubidium atomic clock and basic research. Technical report, AEROSPACE CORP EL SEGUNDO CA PHYSICAL SCIENCES LABS, 2007. 5, 10

K. Campbell, Y.-J. Wang, I. Savukov, P. D. Schwindt, Y.-Y. Jau, and V. Shah. Gradient field detection using interference of stimulated microwave optical sidebands. *Physical Review Letters*, 128(16):163602, 2022. 10, 66, 82

D. Cohen. Magnetoencephalography: detection of the brain's electrical activity with a superconducting magnetometer. *Science*, 175(4022):664–666, 1972. 2, 4

C. Cohen-Tannoudji, B. Diu, and F. Laloe. Quantum mechanics, volume 1. *Quantum Mechanics*, 1:898, 1986. 11

A. Corney. Atomic and laser spectroscopy clarendon, 1977. 10

H. Dang, A. C. Maloof, and M. V. Romalis. Ultrahigh sensitivity magnetic field and magnetization measurements with an atomic magnetometer. *Applied Physics Letters*, 97(15):151110, 2010. 2

H. Dehmelt. Modulation of a light beam by precessing absorbing atoms. *Physical Review*, 105(6):1924, 1957. 2, 4

I. H. Deutsch and P. S. Jessen. Quantum-state control in optical lattices. *Phys. Rev. A*, 57:1972–1986, Mar 1998. doi: 10.1103/PhysRevA.57.1972. URL https://link.aps.org/doi/10.1103/PhysRevA.57.1972. 7

W. Fourcault, R. Romain, G. Le Gal, F. Bertrand, V. Josselin, M. Le Prado, E. Labyt, and A. Palacios-Laloy. Helium-4 magnetometers for room-temperature biomedical imaging: toward collective operation and photon-noise limited sensitivity. *Optics Express*, 29(10):14467–14475, 2021. 2

J. Güdde, A. Klinkmüller, P. West, and E. Matthias. Second-order magnetic contributions to the hyperfine splitting of the 5snd 1 d 2 states in sr 87. *Physical Review A*, 47(6):4725, 1993. 31

M. Hämäläinen, R. Hari, R. J. Ilmoniemi, J. Knuutila, and O. V. Lounasmaa. Magnetoencephalography—theory, instrumentation, and applications to noninvasive studies of the working human brain. *Reviews of modern Physics*, 65(2):413, 1993. 3, 4

W. Happer, Y.-Y. Jau, and T. Walker. *Optically Pumped Atoms*. Wiley-VCH, 2010. 48

W. HAPPER. Optical pumping. *Rev. Mod. Phys.*, 44:169–249, Apr 1972. doi: 10.1103/RevModPhys.44.169. URL https://link.aps.org/doi/10.1103/RevModPhys.44.169. 41

L. Henriet, L. Beguin, A. Signoles, T. Lahaye, A. Browaeys, G.-O. Reymond, and C. Jurczak. Quantum computing with neutral atoms. *Quantum*, 4:327, sep 2020. doi: 10.22331/q-2020-09-21-327. URL https://doi.org/10.223312Fq-2020-09-21-327. 1

A. Horsley and P. Treutlein. Frequency-tunable microwave field detection in an atomic vapor cell. *Applied Physics Letters*, 108(21):211102, 2016. 19

Y.-Y. Jau. Spatial evolution of the multi-coherent light in alkali-metal vapor. An unpublished note for a density-matrix theory and numerical model to describe multi-tone light propagation in an atomic ensemble with non-zero atomic coherences. Please find the originally compiled note (June, 2007) "MLP1.pdf" in the supplemental materials. 48, 56

K. Jensen, R. Budvytyte, R. A. Thomas, T. Wang, A. M. Fuchs, M. V. Balabas, G. Vasilakis, L. D. Mosgaard, H. C. Stærkind, J. H. Müller, et al. Non-invasive detection of animal nerve impulses with an atomic magnetometer operating near quantum limited sensitivity. *Scientific reports*, 6(1):1–7, 2016. 83

K. Jensen, M. A. Skarsfeldt, H. Stærkind, J. Arnbak, M. V. Balabas, S.-P. Olesen, B. H. Bentzen, and E. S. Polzik. Magnetocardiography on an isolated animal heart

with a room-temperature optically pumped magnetometer. *Scientific reports*, 8(1): 1–9, 2018. 83

C. Johnson, P. D. D. Schwindt, and M. Weisend. Magnetoencephalography with a two-color pump-probe, fiber-coupled atomic magnetometer. *Applied Physics Letters*, 97(24):243703, 2010. doi: 10.1063/1.3522648. URL https://doi.org/10.1063/1.3522648. 4, 94

K. Kamada, Y. Ito, S. Ichihara, N. Mizutani, and T. Kobayashi. Noise reduction and signal-to-noise ratio improvement of atomic magnetometers with optical gradiometer configurations. *Opt. Express*, 23(5):6976–6987, Mar 2015. doi: 10.1364/OE.23.006976. URL http://www.osapublishing.org/oe/abstract.cfm?URI=oe-23-5-6976. 3

D. F. J. Kimball, E. B. Alexandrov, and D. Budker. *General principles and characteristics of optical magnetometers*. Cambridge University Press, 2013. doi: 10.1017/CBO9780511846380.002. 5

S. Knappe, V. Gerginov, P. D. Schwindt, V. Shah, H. G. Robinson, L. Hollberg, and J. Kitching. Atomic vapor cells for chip-scale atomic clocks with improved long-term frequency stability. *Opt. Lett.*, 30(18):2351–2353, Sep 2005. doi: 10.1364/OL.30.002351. URL http://opg.optica.org/ol/abstract.cfm?URI=ol-30-18-2351. 10

S. Knappe, P. Schwindt, V. Gerginov, V. Shah, L. Liew, J. Moreland, H. Robinson, L. Hollberg, and J. Kitching. Microfabricated atomic clocks and magnetometers. *Journal of Optics A: Pure and Applied Optics*, 8(7):S318, 2006. 26

R. H. Koch, J. R. Rozen, J. Z. Sun, and W. J. Gallagher. Three squid gradiometer. *Applied Physics Letters*, 63(3):403–405, 1993. doi: 10.1063/1.110032. URL https://doi.org/10.1063/1.110032. 3

I. Kominis. Sub-shot-noise magnetometry with a correlated spin-relaxation dominated alkali-metal vapor. *Physical review letters*, 100(7):073002, 2008. 4

I. Kominis, T. Kornack, J. Allred, and M. V. Romalis. A subfemtotesla multichannel atomic magnetometer. *Nature*, 422(6932):596–599, 2003. 2, 3

P. Lambropoulos and D. Petrosyan. *Fundamentals of quantum optics and quantum information*, volume 23. Springer, 2007. 14

M. Limes, E. Foley, T. Kornack, S. Caliga, S. McBride, A. Braun, W. Lee, V. Lucivero, and M. Romalis. Portable magnetometry for detection of biomagnetism in ambient environments. *Physical Review Applied*, 14(1):011002, 2020. 3, 4, 78, 81

V. G. Lucivero, W. Lee, N. Dural, and M. V. Romalis. Femtotesla direct magnetic gradiometer using a single multipass cell. *Phys. Rev. Applied*, 15:014004, Jan 2021. doi: 10.1103/PhysRevApplied.15.014004. URL https://link.aps.org/doi/10.1103/PhysRevApplied.15.014004. 3

V. Malinovsky and J. Krause. General theory of population transfer by adiabatic rapid passage with intense, chirped laser pulses. *The European Physical Journal D-Atomic, Molecular, Optical and Plasma Physics*, 14(2):147–155, 2001. 90

P. J. Oreto, Y.-Y. Jau, A. B. Post, N. N. Kuzma, and W. Happer. Buffer-gas-induced shift and broadening of hyperfine resonances in alkali-metal vapors. *Phys. Rev. A*, 69:042716, Apr 2004. doi: 10.1103/PhysRevA.69.042716. URL https://link.aps.org/doi/10.1103/PhysRevA.69.042716. 15, 41

F. L. Pedrotti, L. M. Pedrotti, and L. S. Pedrotti. *Introduction to optics*. Cambridge University Press, 2017. 68

D. V. Perepelitsa. Johnson noise and shot noise. *Dept. of Physics, MIT*, 2006. 68, 77

A. Perry, M. Bulatowicz, M. Larsen, T. Walker, and R. Wyllie. All-optical intrinsic atomic gradiometer with sensitivity in a 22 μt earth-scale magnetic field. *Optics Express*, 28(24):36696–36705, 2020. 3

F. M. Pipkin. Atomic physics tests of the basic concepts in quantum mechanics**the preparation of this manuscript was supported in part by the department of energy

and the national science foundation. volume 14 of *Advances in Atomic and Molecular Physics*, pages 281–340. Academic Press, 1979. doi: https://doi.org/10.1016/S0065-2199(08)60130-X. URL https://www.sciencedirect.com/science/article/pii/S006521990860130X. 1

J. W. S. B. Rayleigh. *The theory of sound*, volume 2. Macmillan, 1896. 16

M. A. Rosenberry, J. Reyes, D. Tupa, and T. J. Gay. Radiation trapping in rubidium optical pumping at low buffer- gas pressures. *Physical Review A*, 75(2):023401, 2007. 41

M. Saffman. Quantum computing with atomic qubits and rydberg interactions: progress and challenges. *Journal of Physics B: Atomic, Molecular and Optical Physics*, 49(20):202001, oct 2016. doi: 10.1088/0953-4075/49/20/202001. URL https://doi.org/10.1088/0953-4075/49/20/202001. 1

M. Saffman, T. G. Walker, and K. Mølmer. Quantum information with rydberg atoms. *Rev. Mod. Phys.*, 82:2313–2363, Aug 2010. doi: 10.1103/RevModPhys.82.2313. URL https://link.aps.org/doi/10.1103/RevModPhys.82.2313. 1

S. J. Seltzer. *Developments in alkali-metal atomic magnetometry*. Princeton University, 2008. 2

V. K. Shah and R. T. Wakai. A compact, high performance atomic magnetometer for biomedical applications. *Physics in Medicine & Biology*, 58(22):8153, 2013. 4

D. Sheng, A. R. Perry, S. P. Krzyzewski, S. Geller, J. Kitching, and S. Knappe. A microfabricated optically-pumped magnetic gradiometer. *Applied physics letters*, 110(3):031106, 2017. 3

P. Sikivie. Axion dark matter detection using atomic transitions. *Physical Review Letters*, 113(20), nov 2014. doi: 10.1103/physrevlett.113.201301. URL https://doi.org/10.11032Fphysrevlett.113.201301. 1

B. Simon. *Properties of Adiabatic Rapid Passage Sequences*. Stony Brook University, 2009. 90

M. T. Simons, A. B. Artusio-Glimpse, A. K. Robinson, N. Prajapati, and C. L. Holloway. Rydberg atom-based sensors for radio-frequency electric field metrology, sensing, and communications. *Measurement: Sensors*, 18:100273, 2021. ISSN 2665-9174. doi: https://doi.org/10.1016/j.measen.2021.100273. URL https://www.sciencedirect.com/science/article/pii/S2665917421002361. 1

A. Smith, B. E. Anderson, S. Chaudhury, and P. S. Jessen. Three-axis measurement and cancellation of background magnetic fields to less than 50 μg in a cold atom experiment. *Journal of Physics B: Atomic, Molecular and Optical Physics*, 44(20): 205002, sep 2011. doi: 10.1088/0953-4075/44/20/205002. URL https://doi.org/10.1088/0953-4075/44/20/205002. 1

D. Steck. Rubidium 87 d line data. 2003. xiii, 9, 41, 54, 56, 58

I. Sulai, Z. DeLand, M. Bulatowicz, C. Wahl, R. Wakai, and T. Walker. Characterizing atomic magnetic gradiometers for fetal magnetocardiography. *Review of Scientific Instruments*, 90(8):085003, 2019. 3

H. Tang and W. Happer. Parametric frequency conversion of resonance radiation in optically pumped rubidium-87 vapor. *Physical Review Letters*, 24(11):551, 1970. 25

H. Tang. Parametric frequency conversion of resonance radiation in optically pumped rb 87 vapor. *Physical Review A*, 7(6):2010, 1973. xv, 24, 25, 28, 29, 30

T. M. Tierney, N. Holmes, S. Mellor, J. D. López, G. Roberts, R. M. Hill, E. Boto, J. Leggett, V. Shah, M. J. Brookes, R. Bowtell, and G. R. Barnes. Optically pumped magnetometers: From quantum origins to multi-channel magnetoencephalography. *NeuroImage*, 199:598–608, 2019. ISSN 1053-8119. doi: https://doi.org/10.1016/j.neuroimage.2019.05.063. URL https://www.sciencedirect.com/science/article/pii/S1053811919304550. 2, 4

J. Vanier, R. Kunski, N. Cyr, J. Savard, and M. Têtu. On hyperfine frequency shifts caused by buffer gases: Application to the optically pumped passive rubidium frequency standard. *Journal of Applied Physics*, 53(8):5387–5391, 1982a. 70

J. Vanier, R. Kunski, N. Cyr, J. Savard, and M. Têtu. On hyperfine frequency shifts caused by buffer gases: Application to the optically pumped passive rubidium frequency standard. *Journal of Applied Physics*, 53(8):5387–5391, 1982b. 17

J. Vrba, G. Anderson, K. Betts, M. Burbank, T. Cheung, and D. Cheyne. 151-channel whole-cortex meg system for seated or supine positions, recent advances in biomagnetism, 1999. 3

H. Wang, T. Wu, W. Xiao, H. Wang, X. Peng, and H. Guo. Dual-mode dead-zone-free double-resonance alignment-based magnetometer. *Phys. Rev. Applied*, 15:024033, Feb 2021. doi: 10.1103/PhysRevApplied.15.024033. URL https://link.aps.org/doi/10.1103/PhysRevApplied.15.024033. 82

L. Weller. *Absolute Absorption and Dispersion in a Thermal Rb Vapour at High Densities and High Magnetic Fields.* PhD thesis, Durham University, 2013. 16

R. Wynar, R. S. Freeland, D. J. Han, C. Ryu, and D. J. Heinzen. Molecules in a bose-einstein condensate. *Science*, 287(5455):1016–1019, 2000. doi: 10.1126/science.287.5455.1016. URL https://www.science.org/doi/abs/10.1126/science.287.5455.1016. 1

R. Zhang, R. Mhaskar, K. Smith, and M. Prouty. Portable intrinsic gradiometer for ultra-sensitive detection of magnetic gradient in unshielded environment. *Applied Physics Letters*, 116(14):143501, 2020. 3

J. E. Zimmerman and N. V. Frederick. Miniature ultrasensitive superconducting magnetic gradiometer and its use in cardiography and other applications. *Applied Physics Letters*, 19(1):16–19, 1971. doi: 10.1063/1.1653725. URL https://doi.org/10.1063/1.1653725. 3